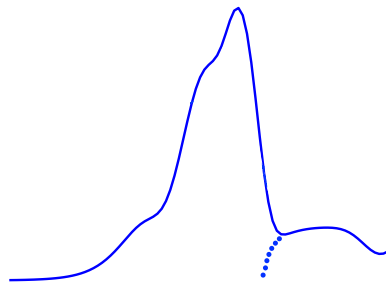


**High temperature
thermoluminescence peaks –
Influence on the albedo principle
for personal dosimetry and benefits
for the new TL-DOS neutron
dosemeter**



**Dissertation
zur Erlangung des akademischen Grades
Doktor der Naturwissenschaften**

vorgelegt von
Myriam Heiny
geboren in Lingen

Lehrstuhl für Experimentelle Physik IV
Fakultät Physik
Technische Universität Dortmund
2020

Der Fakultät für Physik der Technischen Universität Dortmund in Dortmund zur Erlangung des akademischen Grades eines Doktors der Naturwissenschaften vorgelegten Dissertation.

1. Gutachter: Prof. Dr. Kevin Kröninger
2. Gutachter: Prof. Dr. Carsten Westphal
Prüfungsvorsitz: Prof. Dr. Jan Kierfeld
Prüfungsbeisitz: Dr. Bärbel Siegmann

Datum des Einreichens der Dissertation: 15.05.2020
Datum der mündlichen Prüfung: 15.07.2020

Abstract

The individual monitoring service at the Materialprüfungsamt North Rhine-Westphalia and the TU Dortmund are developing the compact dosimeter system TL-DOS based on thin-layer thermoluminescence detectors as well as an associated glow curve analysis tool. Various dosimeters of the system measure different dose quantities and types of radiation.

This thesis focuses on the TL-DOS neutron dosimeter to measure the whole body dose. The system is optimized in terms of LiF:Mg,Ti detectors, an albedo badge, a readout device and the glow curve deconvolution. In order to gain more information about the irradiation scenario such as the particle type, the detectors are measured at 653 K to include the high temperature peaks. After a design specification was defined, the neutron dosimeter is characterized in different photon and neutron radiation fields as well as in workplace fields.

This thesis also presents an analysis that provides the individual induced signal of mixed field irradiations by analyzing the high temperature peaks of a glow curve. The signal induced by irradiation combinations like alpha+photon or neutron+photon fields is separated with only one detector. Finally, the current dealing with the significant energy dependence of neutron dosimeters is critically discussed and new approaches are presented.

Kurzfassung

Die Personendosismessstelle des Materialprüfungsamtes Nordrhein-Westfalen und die TU Dortmund entwickeln basierend auf Thermolumineszenzdetektoren das kompakte Dosimetersystem TL-DOS sowie ein dazugehöriges Glühkurvenanalysetool. Das System beinhaltet verschiedene Dosimetertypen, um unterschiedliche Dosisgrößen und Strahlungsarten zu messen.

In dieser Arbeit wird das TL-DOS Neutronendosimeter zur Messung der Ganzkörperpersonendosis betrachtet. Das Dosimetersystem wird bezüglich der LiF:Mg,Ti-Detektoren, einer Albedo-Sonde, einem Auslesegerät und der Glühkurvenanalyse optimiert. Die verwendeten Detektoren werden bei 653 K gemessen, sodass auch die Glühkurvensignale bei hohen Temperaturen (>573 K) ausgelesen werden. Dies eröffnet die Möglichkeit, Zusatzinformationen über die Bestrahlung wie z.B. den Teilchentyp zu erhalten. Nachdem eine Auswertevorschrift festgelegt worden ist, wird das Neutronendosimeter in verschiedenen Photonen- und Neutronenstrahlungsfeldern sowie Arbeitsplatzfeldern charakterisiert.

Des Weiteren wird eine Analyse vorgestellt, die das induzierte Signal nach einer Mischfeld-Bestrahlung wie z.B. Alpha+Photonen- oder Neutronen+Photonen-Feldern separiert. Durch das Auswerten der "high temperature peaks" wird die Trennung mittels eines Detektors möglich. Zum Schluss wird die aktuelle Vorgehensweise der starken Energieabhängigkeit von Neutronen Dosimetern diskutiert und neue Lösungsansätze werden vorgestellt.

Contents

1	Introduction	1
2	Basic principles of personal neutron dosimetry	3
2.1	The role of neutrons in radiation protection dosimetry	3
2.2	Neutron radiation and neutron fields	4
2.3	Personal dosimetry and dose quantities	8
2.4	Requirements for neutron dosimeter systems	12
2.5	Challenges in personal neutron dosimetry	14
2.6	The albedo method to measure $H_p(10)$	15
2.7	History of personal neutron dosimetry with TLDs	17
3	The TL-DOS neutron dosimeter system	23
3.1	Basics of thermoluminescence	23
3.2	TL-DOS neutron detectors	28
3.3	TL-DOS prototype readout device	33
3.4	TL-DOS albedo dosimeter badge	41
3.5	Detector and dosimeter calibration with Caesium-137	42
3.6	Analysis software	49
4	Characterization of the TL-DOS dosimeter in neutron fields	53
4.1	Neutron reference field facilities at the PTB	53
4.2	TL-DOS dosimeter calibration for neutrons	57
4.3	Comparison to commercial TL albedo neutron systems	65
4.4	Neutron field calibrations in workplace fields	71
5	Supplementary requirements for the new neutron dosimeter	87
5.1	The X-rays facility of the MPA NRW	87
5.2	Energy and angular photon response of the dosimeter	88
5.3	Beta criterion for photon dosimetry	92
5.4	Photon decision threshold and detection limit of the neutron dosimeter	93
5.5	High-LET peaks induced by a high photon dose	96
6	High-LET peaks and their prospects for additional irradiation information	99
6.1	The alpha irradiation setup and alpha induced glow curves	99
6.2	Energy dependence of individual glow peaks	106
6.3	Determination of type of irradiation	107
6.4	Separation of alpha and gamma induced signals after mixed irradiations	110
6.5	Separation of the neutron and the photon dose after mixed irradiations	117

7	Neutron energy dependence of the TL-DOS dosimeter	123
7.1	Energy dependence of the neutron correction factor k and the Z ratio . .	123
7.2	Possible alternative for the energy estimation	126
7.3	Intercomparison of different energy-estimation methods	131
8	Conclusion and Outlook	135
	Acronyms	137
	Bibliography	139

Chapter 1

Introduction

Natural radiation, such as cosmic radiation and radiation from naturally radioactive substances in air, water and soil, have always been present in the vicinity of humans. However, advances in technology, like nuclear power plants and use of X-ray equipment, lead to an increasing number of new sources of radiation.

Since the 1920s, awareness of the risks of radiation has been growing [1]. Legally, radiation protection in Germany is regulated by the "Strahlenschutzverordnung" (StrlSchV) [2]. It's intended purpose is the protection of people and the environment from the harmful effects of ionizing and non-ionizing radiation from natural and man-made sources of radiation. The primary goal is to keep exposure to radiation as low as reasonably possible for each individual person. According to this, critical values on the accumulated dose are set for people, who are occupationally exposed to radiation according to the Radiation Protection Act.

In Germany there are four individual monitoring services, which measure the dose of occupationally exposed persons using dosimeters officially approved. One of these is the Materialprüfungsamt North Rhine-Westphalia (MPA NRW).

The MPA NRW develops in cooperation with the TU Dortmund University a compact dosimeter system called TL-DOS. It is based on the phenomenon of thermoluminescence and will be applied for routine monitoring in the future. The system includes different dosimeter types for the measurement of various dose quantities and kinds of radiation. One advantage is that all dosimeters are read out with the same device.

The main goal of this thesis is the development of a TL-DOS neutron dosimeter, on the one hand to complete the TL-DOS system and on the other hand to take the increasing number of applications that produce neutrons into account.

In addition to the standard requirements of personal dosimetry, neutron dosimeters have to deal with two further facts. Neutron fields are usually mixed fields of neutrons and photons and they cover a very large energy range. These challenges have to be solved.

The neutron dosimeter system currently used in Germany was developed together with an evaluation method at the end of the 1970s. Since applications for neutron dosimetry increased at this time, a suitable neutron system was promptly needed. It serves the purpose of neutron dosimetry, but was not critically examined or revised. Besides, these methods are behind the times, as the technology and fields of application have changed. The TL-DOS system has the main advantage that the detectors are very heat-resistant and can therefore be evaluated and erased at high temperature. This offers the possibility to read out additional signal, that is generated by neutron irradiation. In turn this leads to new prospects for analyzing the measured signal to gain information about the irradiation scenario. With this optimized system and the benefit of additional signal, the challenges of neutron dosimetry and different influences on a neutron dosimeter system shall be better understood. Furthermore, any possible influences shall be eliminated with suitable analysis methods.

This thesis offers: The theoretical backgrounds of neutron workplace fields and personal neutron dosimetry are briefly introduced in Chapter 2. In Chapter 3 the phenomenon of thermoluminescence is explained and the TL-DOS system is optimized specifying the detector design, the readout procedure, an albedo neutron badge and a glow curve analysis tool. Chapter 4 presents different measurements of the designed TL-DOS neutron dosimeter to characterize the system and calibrate it for neutron irradiations. The results of photon irradiations are described in Chapter 5 introducing additional requirements for the dosimeter, followed by Chapter 6 investigating the additional signal and developing and verifying a new analysis. Last but not least, in Chapter 7 new alternatives are discussed and compared to exclude the strong energy dependence of neutron dosimeters. Finally, a conclusion and an outlook are given in Chapter 8.

During this thesis measurements, which are presented in Chapter 4, have been performed in cooperation with various institutes. The following institutes provided possibilities of data recording:

- ELBE Positron Source at Research Center Dresden / Rossendorf (Epos)
- The West German Proton Therapy Centre Essen (WPE)
- Fraunhofer Institut for Technological Trend Analysis INT
- "BGZ Gesellschaft für Zwischenlagerung mbH"
- Two Individual Monitoring Services in Germany (Munich, Dortmund)

Parts of this dissertation were already published or are in a review process in Refs. [3, 4] and some important results have been forwarded to the standard committee of the Deutsches Institut für Normung und Standards (DIN) for revision of the DIN-Norm 6802-4.

Since the TL-DOS neutron dosimeter was presented in the invited lectures of the LPS Summer School 2019 and the 70. Radiometrisches Seminar Theuern, some improvements are made.

Chapter 2

Basic principles of personal neutron dosimetry

In addition to the desired benefit effects of direct and indirect ionizing radiation, such as in cancer therapy, energy generation or material screening, radiation has dangerous effects on the human body. Therefore, it is important to keep this effect as small as possible by providing sufficient radiation protection.

2.1 The role of neutrons in radiation protection dosimetry

In Germany, four officially nominated individual monitoring services provide dose monitoring of occupationally exposed persons. Dosemeters are usually evaluated on a monthly base, with a few exemptions (like firemen) who are not exposed on a regular base and may extend the monitoring period to up to three months. Dosemeters for different types of radiation and the respective applications of ionizing radiation are available. For example in individual monitoring for photon radiation, the film dosimeter is currently used, which will soon be replaced by a thermoluminescence dosimeter system (TL-DOS system) in one of the monitoring services. Other monitoring services are using or planning to use an optically stimulated luminescence (OSL) dosimeter systems in the future. [5]

In mixed photon and neutron radiation fields special neutron dosimeters have to be worn because thermal neutrons are not detected by the film dosimeter. It is recommended to use them, when the neutron dose is more than 10% of the photon dose [6].

Neutron radiation belongs to the natural cosmic radiation and is particularly important at altitudes of the flight corridors of the Atlantic route. In addition, neutrons can be generated or released by fuel elements from nuclear power plants in technical applications, especially in nuclear reactors and nuclear fusion, at particle accelerators for medicine and research with increasing trend. The individual monitoring service in Dortmund (MPA NRW) issues a neutron dosimeter to about 1000 people every month.

2.2 Neutron radiation and neutron fields

The discovery of free neutrons was published by James Chadwick in 1932. Neutrons were produced after irradiating beryllium with alpha particles. This radiation is indirectly ionizing radiation and is not electrically charged. Furthermore, free neutrons are unstable and have a mean life time of (880 ± 1) s. [7]

Neutrons and positively charged protons form together an atomic nucleus and in combination with negatively charged electrons an atom. While the number of protons in an atom defines the element, the number of neutrons specifies the isotope.

2.2.1 Neutron sources and energy spectra of neutron fields at workplaces

Depending on their use, there are different mechanism to produce neutron radiation. The production of free neutrons occurs in most cases by different nuclear processes, in some cases by spontaneous fission. A nuclear process is the interaction of an atomic nucleus with a particle or an atomic nucleus. This reaction changes the state or composition of the atomic nucleus. The probability that such a certain process for an incident particle takes place with the scattering body is given as the cross section.

While released neutrons are often fast with kinetic energies of some hundred keV, slower neutrons with energies in the range of hundred μeV (called thermal neutrons) are usually obtained combing a neutron source with a moderator. The neutrons interact with the moderator and transfer a part of their energy to it.

There are basically four possibilities for formation of neutrons:

1. Neutron formation by radioactive decay: These neutron sources are further categorized into three types. a) A radioisotope that emits alpha particles is mixed with a low-atomic-weight isotope. A typically example for such a neutron sources is a $^{241}\text{AmBe}$ source. In this case an alpha particle from the decay of ^{241}Am hits beryllium, which absorbs the alpha particle. The result is a ^{13}C nucleus which decays into ^{12}C by emitting a neutron. b) For a gamma-beryllium neutron source a combination of a gamma emitter which decay with high-energy photons and a material that has a large cross section for the (γ, n) nuclear reaction is generally necessary. An example of such a source is usually a mixture of antimony (Sb) with beryllium (Be). c) There are also spontaneous fission neutron sources such as ^{252}Cf . A very heavy atomic nucleus with an excess of neutrons compared to the number of protons decays into two lighter nuclei and emits neutrons. [8]
2. At nuclear reactors, neutrons are released during induced nuclear fission. A heavy nucleus decays into medium-heavy, highly excited nuclei, releasing binding energy.

In addition to the fission fragments, 2–3 neutrons are usually released during this reaction. The energy spectrum of these neutrons usually has the form of a Maxwell distribution and can extend up to 15 MeV. [9]

3. It is possible that neutrons are produced at a particle accelerator, if sufficient energy is available during the nuclear reaction. If electron bremsstrahlung has an energy above the binding energy of neutrons in the target nucleus, fast neutrons are released via the nuclear photoelectric effect. This phenomenon can occur, for example, with accelerators that are used to treat cancer patients. [8]
4. Neutron generators are based on nuclear fusion reactors, where two lighter nuclei combine to a heavier nucleus. They produce neutrons with high energies. While, for example, neutrons produced by Deuterium-Tritium reactions (D-T) have an energy of 14 MeV, for neutrons produced by D-D-reaction the energy is 2.5 MeV. [8]

While some accelerators can be used to produce monoenergetic neutron beams, usual neutron fields are mainly scattered radiation fields and have a wide neutron energy spectrum caused by complex interactions of the neutrons with the surrounding matter (see Chapter 2.2.2).

Figure 2.1 shows a simulated spectrum with its typical energy ranges. Neutrons are usually classified by their energy. The spectrum of a neutron field consists of a thermal part (A), an intermediate part (B), a so-called fast energy part (C) and, sometimes a part at very high energies, which are differently pronounced in different fields.

In Figure 2.1 the parts are modeled according to Ref. [10]. The thermal peak is modeled using a Maxwell distribution and for the intermediate region a model of a straight line which went smoothly to zero at the end of this region is used. The fast-energy peak is modeled as a combination spectra of Maxwell, evaporation and fission peaks. The high-energy peak is only found for very high energies of particles served to produce neutrons, reached for example in proton therapy environments. At a proton therapy center the fast and high energy peaks originate from interactions of high-energy primary protons. For example fast neutrons are produced by nuclear processes like nuclear fission. This neutrons are moderated caused by room scattering resulting in a thermal neutron peak. At various places in the same room a strong spatial dependence can be observed for neutron energy spectra because the neutrons interact often with matter.

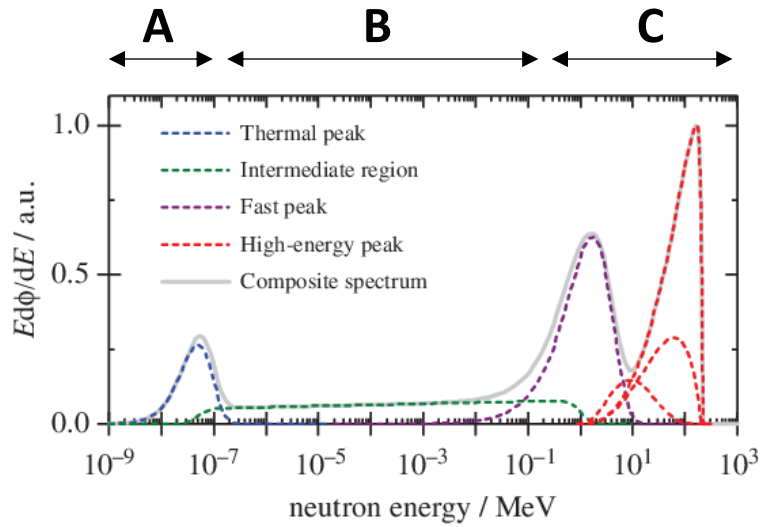


Figure 2.1: A neutron energy spectrum modeled for a neutron field occur in a proton therapy center [10]. The energy areas are modeled using different functions, and the neutrons are classified. A: Thermal neutrons B: Intermediate-energy neutrons C: Fast- and high-energy neutrons.

2.2.2 Radiation interactions with matter and tissue

When photon radiation, traverses matter, it can transfer its energy to matter by three different processes. These are the photoelectric effect, the compton effect and pair production, which dominate differently depending on material and energy. The intensity of a photon beam decreases exponentially. When enough energy is transferred, an atom can be ionized.

Charged particles such as protons suffer inelastic collisions with electrons in matter, which causes a transfer of energy so that atoms are ionized or excited. The energy loss dE of a charged particle is described by the Bethe-Bloch Formula. It depends on the charge and the kinetic energy of the particle, and therefore increases with the energy.

$$-\frac{dE}{dx} \tag{2.1}$$

For electrons the energy loss is slightly different and a special case. Since electrons are very light, the bremsstrahlung is an additional, important component for them. Accordingly, the Bethe-Bloch formula has to be modified for considerations of electrons.

While the effects described so far take place at the electron-level of an atom, neutral particles such as neutrons are scattered or absorbed at atomic nuclei. Typical processes

are elastic or inelastic scattering, neutron capture and fission of an atomic nucleus.

The process of elastic scattering describes the scattering of fast neutrons on light atomic nuclei, which causes them to decelerate until they will turn thermal. This is the most relevant effect in tissue. Fast neutrons scatter with protons of water molecules and kinetic energy is transferred to the protons. These so-called recoil protons move through the absorber and can perform direct ionization. Since protons are densely ionizing, they deposit their energy very close to their origin. This mainly contributes to the formation of a dose. Therefore, neutrons are very effective in radio-biology and play a crucial role in radiation protection.

During inelastic scattering, a neutron is briefly captured by nuclear force and transfers a part of its energy to the nucleus. Thus, the atomic nucleus remains in an excited state after scattering, usually returning to the ground state by emission of gamma radiation. This process can only take place at multi-nucleon nuclei, i.e. in the body it takes place at carbon (C), nitrogen (N) and oxygen (O) atoms.

A further important phenomenon is the neutron capture reaction. If a neutron moves past a nucleus, it can be captured by it. Since the probability for this process decreases with the neutron energy, neutron capture mainly occurs with thermal neutrons. The excess energy is typically released as a high-energy gamma quantum (exothermic reaction) and secondary particles are formed.

In the human body the probability that a neutron (n) is captured by an atom is highest for hydrogen atoms. During this process hydrogen turns into deuterium (d), also known as heavy hydrogen, and photons with an energy of 2.225 MeV are emitted:



p is the proton of a hydrogen atom. With higher neutron energy the relative importance of other reaction types increases. Furthermore, heavy nuclei can undergo fission after capturing a neutron. [7, 11]

2.2.3 Damage and cell death effects of radiation on humans

It is already known that material properties of metals and other materials are deteriorated by neutron irradiation. This limits the lifetime of components in e.g. nuclear reactors. The effect on living tissue is also harmful. It is based on fast neutrons mostly interacting with protons of water molecules. The resulting recoil protons correspond to a strongly

ionizing radiation. It results in biological and toxicological effect on people.

A distinction is made between two types of radiation damage: On the one hand, deterministic damages occur above a certain dose threshold. On the other hand, there are stochastic damages where the probability of this damage increases with increasing irradiation. [12]

Furthermore, different radiation types are variously harmful. As a measure for the effect of various radiation types the linear energy transfer (LET) is defined:

$$L_{\Delta} = \frac{dE_{\Delta}}{dx}. \quad (2.3)$$

It describes how much energy E on average is lost along a distance x by ionization processes. Only the energy transferred in the vicinity of the primary particle track is taken into account. Secondary electrons whose energy is larger than a certain value Δ are excluded because a larger energy implies a larger range. While for example electrons have a low LET, alpha particle and neutrons are high LET radiation, they deposited more energy at the same distance, see Bethe-Bloch formula (2.1).

2.3 Personal dosimetry and dose quantities

Energy is transferred to matter and tissue through the interaction processes described in Chapter 2.2 above. To quantify this effect, the physical basic dose quantity, the absorbed dose D , is used. It is a measure of how much energy per mass has been deposited in a medium. In medical applications the medium is often presumed to be water due to the high percentage of water in the human body.

$$D = \frac{dE}{dm} \quad [D] = \text{Gy} = \text{J/kg}. \quad (2.4)$$

To measure dose the quantity kerma ("kinetic energy released per unit mass") is defined as kinetic energy dE_{kin} deposited per mass:

$$K = \frac{dE_{\text{kin}}}{dm} \quad [K] = \text{Gy}. \quad (2.5)$$

Kerma is a calibration quantity that can be measured directly using an ionization chamber. If the dose is built up to match electronic equilibrium (regarded as secondary electron equilibrium), then the absorbed dose D is equal to the kerma K . [13]

However, both quantities do not take into account any radiation type- or biological radiation-effects. They are purely 'physics' quantities and do not provide any estimate

on the radiation induced risk. Therefore, additional radiation protection quantities are defined, the equivalent doses, which are more relevant for radiation protection. The radiation type is taken into account in dose calculation by multiplying a radiation-dependent weighting factor ω_R to the absorbed dose to obtain the so-called radiation equivalent dose:

$$H_T = \sum_R D_{T,R} \cdot \omega_R \quad [H_T] = \text{Sv}. \quad (2.6)$$

Weighting different radiation types is necessary because different radiations produce different amounts of biological damage, although the deposited energy may be the same. While photons have a factor of $\omega_R = 1$, neutrons, for example, have a ω_R -factor between 5–20 due to the effect of the LET described in Section 2.2.3). The factor depends on the neutron energy as shown in Figure 2.2. The weighting factor increases for higher energies until it reaches its maximum at approx. 1 MeV, which means that radiation with higher energy is more harmful to the tissue because more ionizations occur at the same distance. For even higher energies the value decreases. In this case the neutrons are fast so that the probability of neutron capture is reduced.

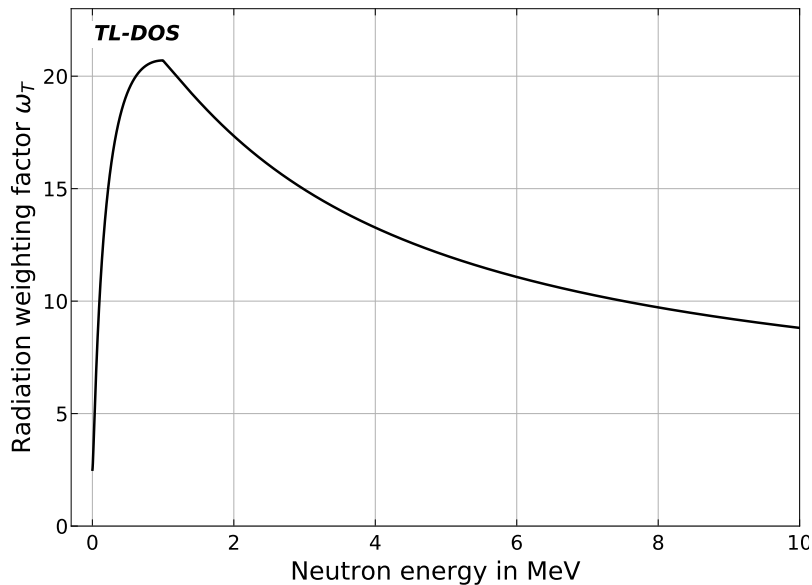


Figure 2.2: Function to specify the radiation weighting factor ω_R dependent on the neutron energy. Defined in [13].

To include also the radiation sensitivity of the individual organs, the dose equivalent is multiplied by the weighting factors of the respective organ first. In a second step all

organs are summed up so that the effective dose

$$E = \sum_T \omega_T \cdot H_T \quad [H_T] = \text{Sv} \quad (2.7)$$

results as weighted average. This quantity can be used to calculate the risk of radiation on tissue, so that limits that a person may not exceed in a month and a year are defined for this effective dose E . The consideration of the radiation type and the sensitivity of the tissue is shown as ① and ② in Figure 2.3. It results in radiation protection quantities, which are, however, not directly measurable.

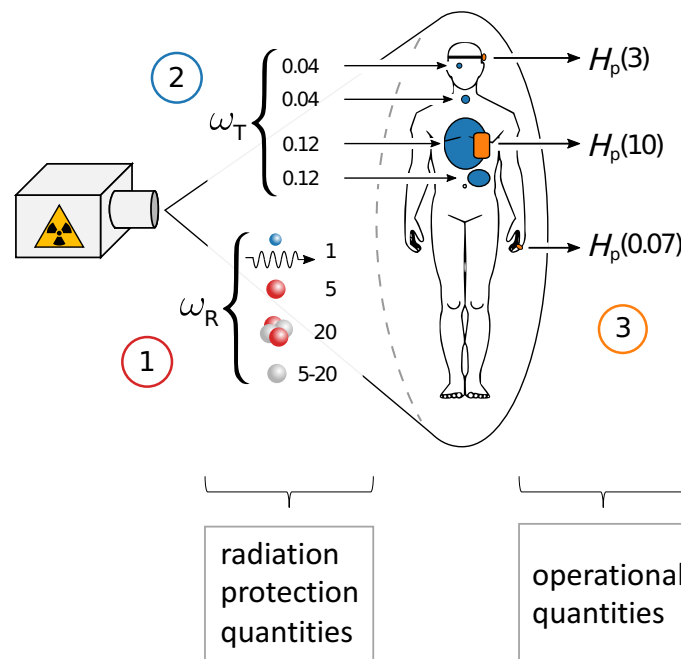


Figure 2.3: Radiation protection quantities are estimated through operational quantities. (modified from Ref. [14]) ①: Values of the radiation weighting factor ω_R for four types of radiation. ②: Weighting factors for different tissues in the human body. The values are defined in Ref. [13]. ③: Measurable operative quantities (defined in Ref. [13]).

Therefore, the operational quantities were introduced in the reports of the International Commission on Radiation Units and Measurements (ICRU) [13]. These quantities estimate the protection quantities and are measurable. The operational parameters include personal dose parameters (Figure 2.3, ③) and also ambient dose parameters. The personal dose equivalent $H_p(d)$ is defined in soft tissue at an appropriate depth, d , below a specified point on the human body [13]. For example, the whole body dose equivalent $H_p(10)$ in 10 mm tissue depth is used to estimate the effective dose, whereas $H_p(0.07)$

in 0.07 mm tissue depth is used as partial body dose to estimate the skin dose. The $H_p(10)$ dose is measured by a whole body dosimeter worn on the torso. It is worn in a position representative of the possible radiation exposure, usually on the chest, facing the radiation source.

The ambient dose equivalent $H^*(10)$ which is used for area dose monitoring is also defined in the ICRU report. It is designed to estimate $H_p(10)$ at a point which would be produced in a human if he would be standing in that exact place and is measured in a spherical ICRU phantom. [15, 16]

Dosimeters for the determination of equivalent doses are calibrated either via kerma combined with special factors or on associated phantoms.

An $H_p(10)$ dosimeter only provides a correct dose indication when a backscattering body to include also radiation backscattered at the body is present.

For experimental investigations and calibration purposes of a whole body dosimeter, the human body is replaced by a water slab phantom, which simulates the backscattering from the human body especially of the torso. It is a water-filled cuboid made of Polymethylmethacrylate (acrylic glass) (PMMA) with the dimensions 30 cm by 30 cm by 15 cm. The dosimeter detects the incident radiation as well as the radiation scattered back from the human body caused by a slab phantom in experimental set ups.

Figure 2.4 (left) shows the water phantom produced by PTW (Physikalisch-Technische Werkstatt Freiburg) and used in this thesis.

In Figure 2.4 (right) the principle of such a dosimeter phantom combination is shown. It is attached to a water phantom and measures not only the incident radiation but also the back-scattered components.

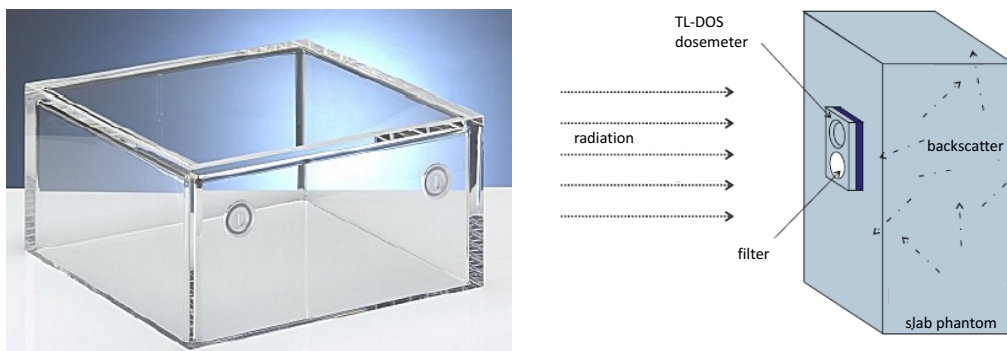


Figure 2.4: Left: Image of the water slab phantom [17]. Right: General principle of a dosimeter to determine a personal equivalent dose. Ref. [13] serves as input.

2.4 Requirements for neutron dosimeter systems

In general, for the development of a dosimeter system a lot of requirements have to be considered and fulfilled. For example, there are various requirements for the measurement technology including a readout device, for the physics of e.g. fulfilling a certain dose measuring range or for the evaluation software. All of these requirements are defined in Ref. [18]. Furthermore, a monitoring service prefers low cost and a high comfort for the users (wearing the dosimeter) as well as the employees who evaluate the system. Since a neutron dosimeter measured photon and neutron radiation, the requirements for both are considered separately.

Considering the measurement of the whole body dose equivalent for photons, an official design certification through passing the type test is necessary before using the system. Therefore, a neutron dosimeter has to fulfill the measuring range from 0.1 mSv to 2 Sv for photon energies from 20 keV to 7000 keV. All requirements are listed and specified in the PTB A's [18]. They include the dose quantity, the measuring range, the photon energy, beam angle of incidence, ambient temperature, relative humidity, mechanical shock, etc. Environmental influences under which it has to be ensure that there is no influence on the whole body dose equivalent. Some requirements of photon dosimetry are considered for the TL-DOS neutron dosimeter in Chapter 5.

Further requirements of the dosimeter concern the measurement of the neutron whole body dose, for which there is no official design certification necessary because the German 'Eichgesetz' [19] does not provide any regulations for the official verification of neutrons. In principle, however, a dosimeter should cover approximately the following range [6]:

- Neutron energies: 0.5 eV to 15 MeV,
- Measuring dose range for neutrons: 0.1 mSv to 1.0 Sv.

Nonetheless, instead of an official design certification, various comparison tests are taken to check these ranges and compare a system to others. In Germany the system is tested annually using reference irradiations performed by the Physikalisch-Technische Bundesanstalt (PTB). The PTB irradiates different scenarios and the monitoring service provides information about the dose allegedly present on the dosimeter. If the measured dose H_m is divided by the dose irradiated, the dosimeter response R is calculated:

$$R = \frac{H_m}{H_{\text{irrad}}}. \quad (2.8)$$

For an official neutron dosimeter the response is limited to values between the response values should be in order to be acceptable. For these test the limits [20] were set to:

$$0.5 \cdot \left(1 - \frac{2 \cdot 0.1}{0.1 + H_{\text{irrad}}} \right) \leq R \leq 2. \quad (2.9)$$

The limits are shown graphically in Figure 2.5.

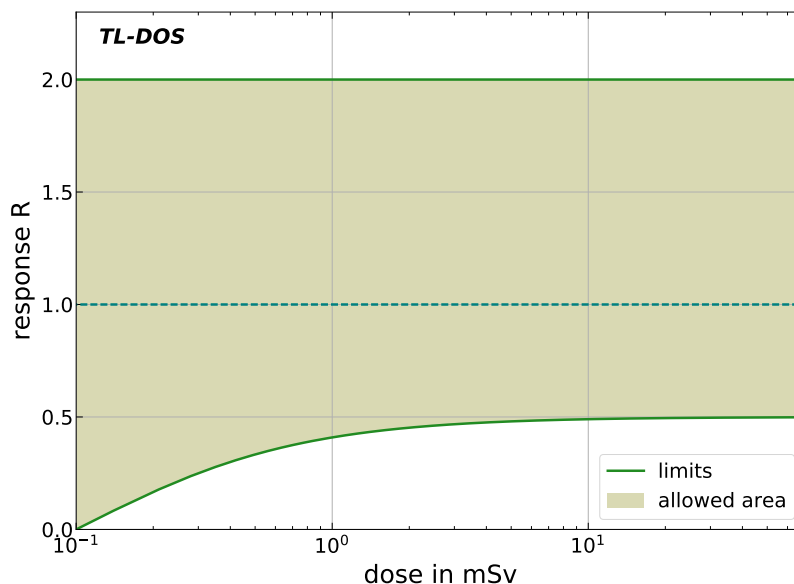


Figure 2.5: Interval of an acceptable response of a neutron dosimeter depending of the neutron dose. The allowed area is illustrated in light green and the limits are marked in dark green.

Additionally, regular intercomparisons are performed by The European Radiation Dosimetry Group (EURADOS). This organization has successfully executed the intercomparison IC2012n [21], which was launched for personal neutron dosimeters routinely used to measure personal neutron dose equivalent, $H_{p,n}(10)$. Participants from the whole world can register their system for EURADOS intercomparisons to test it. Irradiation laboratories irradiated the participating dosimeters with different energy spectra and doses H_{irrad} . After the dose is evaluated by the participants the dose values H_m were compared with the irradiated doses (reference values), given by the irradiation laboratories by calculating the response value R by equation (2.8).

The EURADOS IC2012n is an important action in the field of regular performance tests in neutron dosimetry for international level because until today it is the most extensive intercomparison worldwide to test and compare different neutron dosimeter systems.

2.5 Challenges in personal neutron dosimetry

In contrast to photon dosimetry there are two additional challenges for neutron dosimeters to measure the whole body dose equivalent.

1. Neutron fields are mixed fields.

The fact that neutrons do not emerge alone disturbs the measurement. Wherever neutrons are generated, they interact and secondary particles such as photons and protons are generated. Thus, a neutron field always consists of photons as well, so they are mixed fields. Sometimes photons already origin from the source as well.

Therefore, the neutron dose has to be extracted from the signal induced by mixed fields.

2. Strong energy dependence.

Measuring the dose equivalent over a wide range of neutron energies from thermal up to a few MeV is a challenge in neutron dosimetry. A conversion coefficient P_E is used to convert neutron fluence Φ (particles n per area A) at a point in the radiation field into the personal dose equivalent at 10 mm depth at the ICRU tissue slab phantom, where E is the energy of the incident neutrons impinging on the phantom at an angle α . The conversion coefficient of the personal dose equivalent in 10 mm depth, $H_{p,n}(10)$ varies very strongly depending on the energy.

$$H_{p,n}(10) = \frac{\Phi \cdot P_E}{10^{-9}} \quad [P_E] = \text{pSv} \cdot \text{cm}^2 \quad [H] = \text{mSv}. \quad (2.10)$$

In Fig. 2.6 (left) it is visible that P_E increases by a factor of about 60 between 10 keV and 20 MeV. This is based on the fact that different interactions (describes in Chapter 2.2) with tissue dominate for different neutron energy regions. While for large energies the elastic scattering dominates, for small energies the capture reactions are the relevant processes. The same fluence results in a higher dose equivalent for higher energies.

This strong energy dependence of the conversion coefficient presents challenges for the design of a personal neutron dosimeter because energy spectra of neutron fields usually reach over a wide energy range. Furthermore, neutron dosimeters usually have a strong energy dependence, but opposite to that of the P_E -factor (see Figure 2.2). Figure 2.6 on the right shows an example of a neutron dosimeter response. For low energies the dosimeter shows a large signal and for high energies a small signal. Fast neutrons begin to deposit dose equivalent via elastic scattering on hydrogen, but the energy deposited is small and hence difficult to measure. [22]

High energy neutrons produce a high dose but are more difficult to detect, the dosimeter response for them is two orders of magnitude lower than for thermal neutrons.

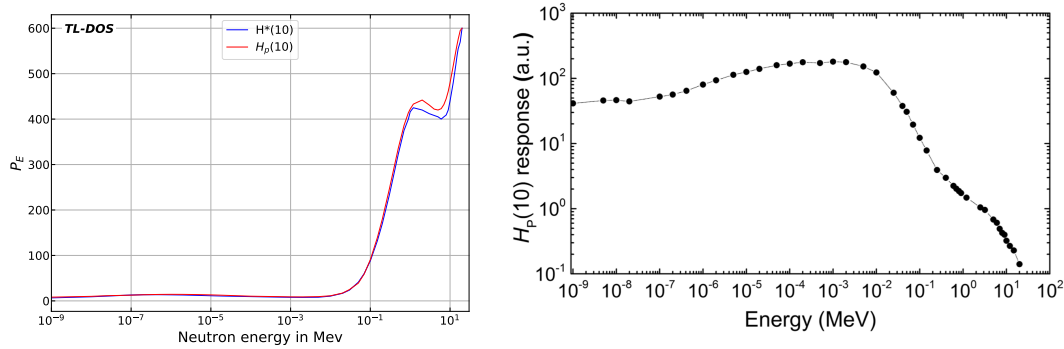


Figure 2.6: Left: Conversion coefficient to calculate the whole body dose from the neutron fluence as a function of the neutron energy. The values for the coefficient are defined in Ref. [22]. Right: $H_{p,n}(10)$ response of a TLD albedo dosimeter calculated with Monte Carlo simulations as a function of neutron energy as example for a dosimeter response [23].

An energy measurement of the neutrons impinging on the dosimeter is often not available, and since neutron fields at the workplace are never monoenergetic (see Chapter 2.2.1), the energy dependence of the dosimeter response has to be compensated to avoid under- or overestimating of the dose.

A common solution for these problems is the use of bubble [24], track [25, 26] and albedo dosimeter [27]. All of them have various advantages and disadvantages and no dosimeter system combines the energy response, sensitivity, space dependency and accuracy required for a personal dosimeter good [28, 21]. Currently, in Germany personal neutron dosimetry is performed with albedo dosimeters which are described in detail in the next chapters. They are optimized for the sensitive range of most applications.

2.6 The albedo method to measure $H_p(10)$

There are several ways to solve the challenges of neutron dosimetry described in the previous chapter. One of them is the albedo method which is exemplified more in detail below and was first used by Burgkhardt and Piesch [29].

An albedo dosimeter consists of four detectors in total, see Figure 2.7. The detectors work in pairs, one detector neutron- and photon sensitive and one only sensitive to photons. The neutron signal will be determined by the difference of these two:

$$H_n = H_{n+\gamma} - H_\gamma. \quad (2.11)$$

H_j is the measured dose of the detector sensitive to j , for example $H_{n+\gamma}$ is the dose induced on the neutron+photon sensitive detector. In principle, this method can be used with various detector types, but usually thermoluminescence detectors (TLDs, explained in Chapter 3) are used for this method.

While this solves the problem of mixed fields and separates the signal contributions, the challenge of the strong dosimeter energy dependence remains. That is why there are always two of such detector pairs in a badge, one field and one albedo pair. While the field pair measures the radiation and dose $H_{n,F}$ of the neutron field, the albedo pair detects the neutrons and photons scattered back from the body or the phantom. The energy range of the radiation is estimated by the ratio of the two specific neutron signals, see Section 2.7.2. The detector pairs are shielded from the other direction in the badge by boron filters. Boron moderates and shields neutrons well, see Chapter 3.4.

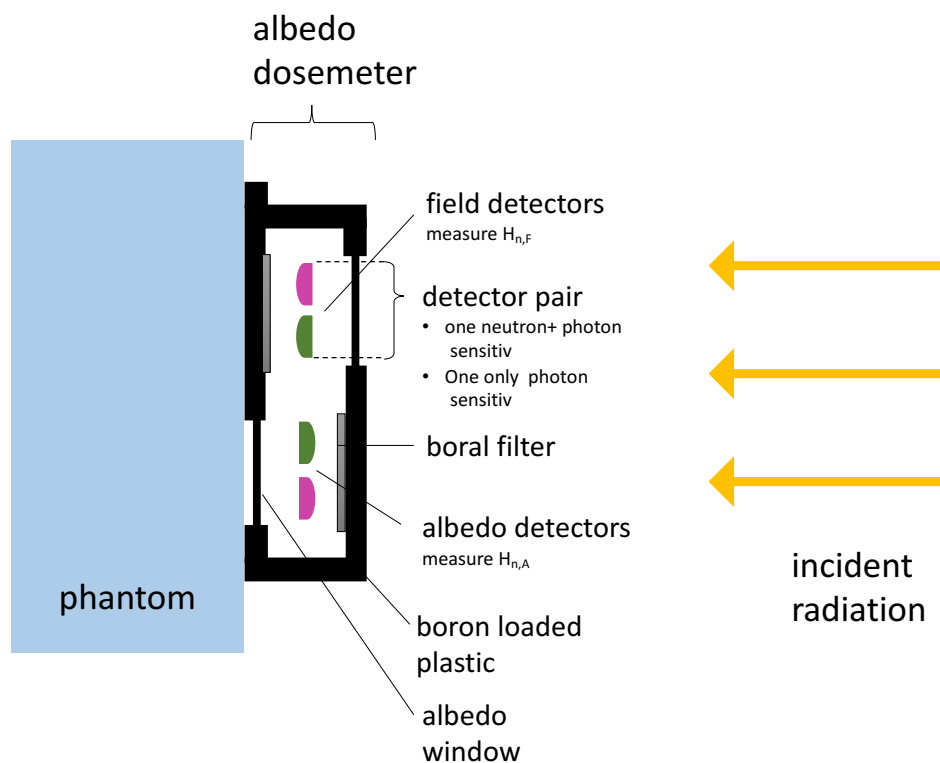


Figure 2.7: Illustration of the albedo method to measure the photon and neutron equivalent dose $H_p(10)$. An albedo dosimeter (in black) is irradiated on a slab phantom and its components like field and albedo detectors and shielding filters are also shown. Detectors sensitive to photons are displayed in green and photon+neutron sensitive detectors in pink.

2.7 History of personal neutron dosimetry with TLDs

In Germany official personal neutron dosimetry has been performed with so-called neutron films for decades. These are nuclear track films that detect recoil protons.

In the 1970s the neutron albedo dosimeter was developed [29]. Albedo dosimeters allow an indirect measurement of neutrons moderated in the body of the user to give information about the neutron dose equivalent. They have been used for neutron dosimetry at the monitoring service Karlsruhe (KFK) since 1982. Initially, it was used for test purpose only. In contrast to the films, the albedo dosimeter covers a lower energy range, in which most of the neutron scattered radiation fields are located [28]. Workers are rarely exposed to the bare source; instead the neutrons in the workplace fields have lost energy via several or many scattering processes, so they have a very broad range of energies (see Figure 2.1). Typically the energy distribution features a thermalized peak ($E_n < 0.4 \text{ eV}$), a smaller intermediate energy component ($0.4 \text{ eV} < E_n < 10 \text{ keV}$) and a residual fast distribution ($E_n > 10 \text{ keV}$), see Figure 2.1. A neutron dosimeter should in particular be able to detect neutrons below $E = 500 \text{ keV}$.

In consequence of the development and usage of albedo dosimeters, the project 'Testing of an albedo neutron dosimeter' (1983-1986) was launched and funded by the BMU (Federal Ministry for the Environment, Nature Conservation and Nuclear Safety). Four governmental measurement services with different detector systems participated in this project. (Participated thermoluminescence detector (TLD)-systems: Alnor, Harsahw, Panasonic, Vinten)

Finally, after gathering of experience, the question should be clarified whether albedo dosimeters should be officially used in Germany in the future.

2.7.1 Implementation and results of the albedo projekt

The KFK report (1988) discusses the performance and the results of the mentioned project 'Testing of an albedo neutron dosimeter' [28].

As first step, many field calibrations (see Section 4.4.1) were carried out in various fields of neutron dosimeter applications. Figure 2.8 shows the results of these field calibrations. R is the dosimeter response and Z is a parameter which can be calculated from the different measurements of an albedo dosimeter. After these measurements, four application areas of the dosimeter were defined for routine use considering the intention that in each range the energy-dependent response $R_{E,\Omega}$ should not exceed a value of 2.

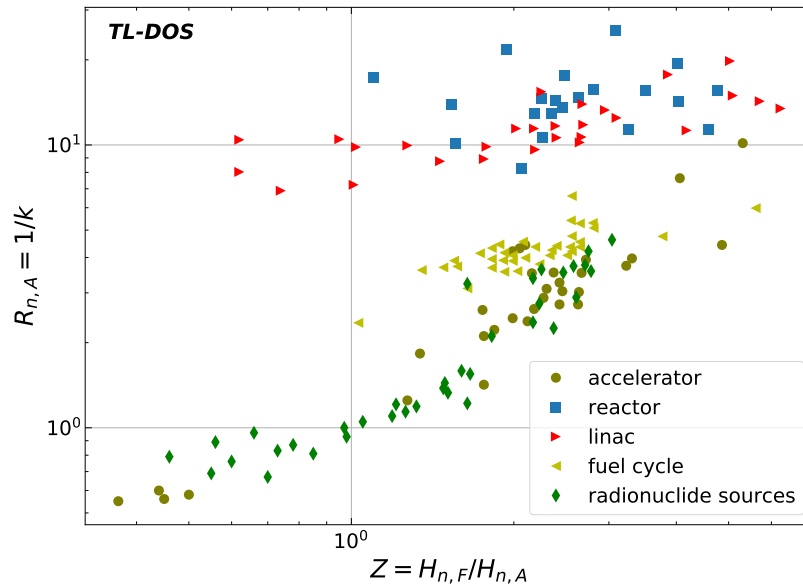


Figure 2.8: Response of the albedo dosimeter used for field calibration in various neutron workplace fields performed in the course of the KFK albedo project. Measurement results of KFK report [28]. Digital data courtesy of Burghardt.

Field calibrations are not performed everywhere, but in typical areas for an energy range. Then, curves to estimate R are determined for using them for all other measurements in this application to restrict the strong energy dependence.

It distinguishes between neutron scattered radiation fields behind strong shielding or weak shielding when handling fissile material, handling neutron sources and particle accelerators of high energies.

In radiation fields of high alternating neutron energy e.g. high-energy particle accelerators, an additional nuclear track detector (a polycarbonate foil), which allows measurements above 3 MeV, can be used as supplement to the albedo badge. If the dose measured with the albedo dosimeter is exceeded a limit defined in [2], there will be a subsequent field calibration for the field of proof. [28]

The second step of the project was to prove that the dosimeter fulfills the requirements for routine personal monitoring. After field calibration tests, the albedo dosimeter was used by different monitoring services, including MPA NRW. Interesting and important results are found. Surprisingly high neutron exposures, which could not be detected with the NTA film, were measured at irradiation channels of the research reactor F2 and also in other applications of the albedo dosimeter.

Consequently, the neutron film was replaced by the albedo dosimeter. The albedo dosimeter has become the official dosimeter for individual neutron monitoring in Ger-

many (1986). Since an improved detection limit was confirmed, dose values were measured and exceedance of dose limit values were detected that had not been measured before, the committee of the federal states for nuclear energy issued the recommendation to use the albedo dosimeter in personal monitoring. It was also new that the equivalent dose of hard beta radiation, photon radiation and neutron radiation could be separated within one dosimeter. [28]

Until today, the albedo dosimeter is still used in Germany with its advantages, especially the detection of low-energy neutrons, also because there is no other energy-independent solid state neutron dosimeter for routine use. The four German monitoring services use Harshaw TLD systems with different detector thicknesses (see also Section 4.3.1).

2.7.2 Conventional determination of $H_p(10)$ in Germany

Since the albedo dosimeter became the standard for personal neutron dosimetry, an evaluation specification had to be stipulated quickly in a standard in order to guarantee uniformity. While in 1998, DIN 6802-4 [30] was published for Germany and the PTB's reference fields were defined on the basis of the four application areas and their field calibrations, the international standards have covered albedo dosimeters in ISO 21909-2 [31]. The DIN standard is currently being revised and describes the evaluation method of albedo dosimeters explained in the next paragraphs.

The person dose equivalent $H_p(10)$ is divided into a photon dose equivalent $H_{p,\gamma}(10)$ and a neutron dose equivalent $H_{p,n}(10)$. Both can be determined from measurements with an albedo dosimeter.

The photon dose is calculated with equation (2.12).

$$H_{p,\gamma}(10) = k_{\gamma;E} \cdot (k_F \cdot M_2 - M_{0,2} - \dot{H}_{nat} \cdot t_e). \quad (2.12)$$

Where $k_{\gamma;E}$ is the correction factor for the energy dependence and k_F is the correction factor for fading (explained in Chapter 3). The latter is assumed to $k_F = 1$ in this thesis because of the measurement equipment used. Generally, M is the product of the calibration factor N and the measurement signal S , indicating the measured dose. M_2 is the dose indication at position 2, i.e. of the photon sensitive albedo detector. $M_{0,2}$ corresponds to the signal resulting for a measurement of a non-irradiated photon albedo detector. \dot{H}_{nat} accounts for the natural ambient dose during the exposure period t_e into account.

According to the DIN 6802-4 the neutron dose $H_{p,n}(10)$ is calculated by multiplying the albedo neutron measurement $H_{n,A}$ with the energy-specific correction factor (k factor) k :

$$H_{p,n}(10) = k_{n,E,\Omega} \cdot H_{n,A} \quad (2.13)$$

with

$$H_{n,A} = M_{A,1} - M_{A,2} \quad (2.14)$$

$$= (k_F \cdot N_{\gamma,1} \cdot S_{A,1} - S_{0,A,1}) - (k_F \cdot N_{\gamma,2} \cdot S_{A,2} - S_{0,A,2}). \quad (2.15)$$

Parameter M already contains the signal measured, fading corrections, calibration to ^{137}Cs and the background subtraction. M_A is the signal of the inner 'Albedo' detectors and the numerical index is a byword for the detector position in a dosimeter badge.

The neutron calibration factor $k_{n,E,\Omega}$ depends on the range of application specified by the users themselves. The ratio Z between outer $H_{n,F}(field)$ and inner $H_{n,A}(albedo)$ neutron display is calculated:

$$Z = \frac{H_{n,F}(field)}{H_{n,A}(albedo)}. \quad (2.16)$$

The energy dependence is calculated according to the four application areas defined as N-ranges in Table 2.1. These and the whole analysis method were specified using the data presented in Figure 2.8.

Table 2.1: Variety neutron fields are classified into four typical application areas [30, 27].

N-category	Z	k	example application
N1	<1.05	$0.55 \cdot \nu_1$	nuclear power plant
	$1.05 \leq Z \leq 2.5$	$10^{-0.235} \cdot Z^{-1.15} \cdot \nu_1$	research reactor, heavy shielding
	>2.5	$0.2028 \cdot \nu_1$	medical linear accelerators
N2	Z	$1.25 \cdot \nu_2$	fuel element cycle criticality, low shielding
N3	<0.3	$7.5 \cdot \nu_3$	radionuclide neutron sources
	$0.3 \leq Z \leq 1.05$	$10^{0.639} \cdot Z^{-0.452} \cdot \nu_3$	
	$1.05 \leq Z \leq 7$	$10^{0.654} \cdot Z^{-1.15} \cdot \nu_3$	
	>7	$0.48 \cdot \nu_3$	
N4	<0.5	$10 \cdot \nu_4$	accelerators for research and technology
	$0.5 \leq Z \leq 7$	$10^{0.654} \cdot Z^{-1.15} \cdot \nu_4$	
	>7	$0.48 \cdot \nu_4$	

The corresponding functions calculate an energy dependent neutron correction factor, so that the response of the dosimeter is corrected. The curves are graphically shown in Figure 2.9. In routine dosimetry the calculated Z is inserted into one of the four step functions (Figure 2.9), so that the $k_{n,E,\Omega}$ factor is determined by this curve.

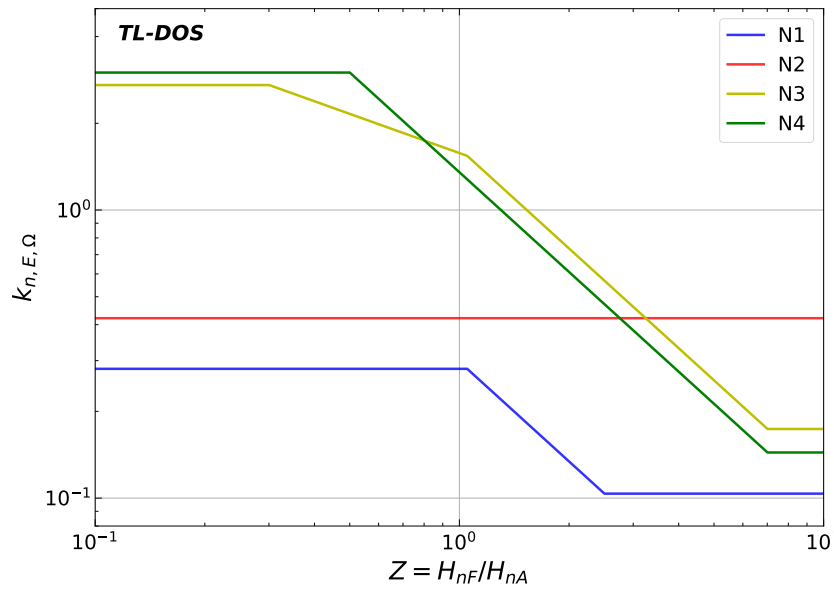


Figure 2.9: Functions of the four albedo dosimeter applications to determine the energy dependent neutron correction factor $k_{\gamma,E}$.

Chapter 3

The TL-DOS neutron dosimeter system

The MPA NRW develops an own technology as dosimetry system for individual monitoring in cooperation with the TU Dortmund in the thermoluminescence dosimeter system project called TL-DOS. The TL-DOS system is a compact dosimeter system which includes different dosimeters to measure the whole body dose, the eye-lens dose, the partial dose for photon and beta radiation or clinical quantities. All TL-DOS dosimeters are based upon the physical phenomenon of thermoluminescence (TL).

In this thesis, a TL-DOS neutron dosimeter is designed to complete the system. Two goals are pursued. One is to optimize all components of the TL-DOS system for a neutron dosimeter with a better energy dependence of the dosimeter response and the other is to analyze neutron fields with respect to energy distributions in order to understand the appropriate correction factors applied to the dosimeter and modify the analysis of the dosimeter appropriately.

This chapter presents central aspects of theoretical principles of TL, detector design and the readout process. Specifically, the thesis focuses on the neutron dosimeter whose used to explain the TL-DOS system.

A dosimeter system consists of several components which are detectors, a badge, a readout device, the human or a back-scatter body and an analysis tool. The components modified compared to the TL-DOS photon dosimeter [14] are explained in this chapter and a calibration method for the new system is discussed.

3.1 Basics of thermoluminescence

TL dosimetry systems are widely used internationally in dosimetry. The phenomenon of TL was scientifically first mentioned by Robert Boyle in 1663 as 'glimmering light' from a diamond [32].

In 1953, TL materials were first used in dosimetry to measure radiation following an atomic weapon test and in medicine to treat cancer patient. Due to their high sensitivity

and small size, TL materials are still used for dosimetric purposes in many countries around the world. [33]

When a TL material, such as a crystal, diamond or salt, is irradiated, it stores the deposited energy and emits the stored energy as photons during heating ('thermo'). These photons are typically in the wavelength range of blue light and called TL light (TL-light). In the dose range of personal dosimetry the emitted light is proportional to the dose irradiated.

The theoretical background of the principle of TL can be explained within the solid state energy-band model. The highest occupied electron energy band, called the valence band, is completely filled preventing electrons from moving. The next higher energy band is called the conduction band. Between these two no allowed states exist in insulators and semiconductors. This is referred to as the band gap.

The most popular and common TL material is Lithium Fluoride doped with Magnesium and Titanium (LiF:Mg,Ti) for TL dosimetry. Since the band gap is $E_{gab} \approx 13\text{ eV}$, it is an isolator. Figure 3.1 shows the band model of a TL material with its conduction band, valence band and band gap. [33]

If energy is deposited in the material for example through photo effect or compton effect during an irradiation, an electron can be excited into the conduction band which enables movement in the crystal lattice. The electrons which can move freely in the conduction band leave a positive charge behind, which is also mobile. It is referred to as a hole, since it stems from the absence of a valence electron.

Subsequently, there are two main possibilities for an electron and a hole. Either the electron recombines directly with a hole while relaxing back and energy ΔE becomes free by emitting a photon. Or they can be locally bound in, so-called, traps due to their meta stable nature. Traps are additional local energy levels in the band gap in a depth of ΔE from the conduction band caused by lattice defects, impurities and the doping with Magnesium and Titanium. This process is displayed as step 1) in Figure 3.1. [33]

A trapped electron can escape from a trap and be lifted back into the conduction band by external energy supply. With regard to TL, energy is added to the system through heat. With increasing temperature, the probability for the escaping process increases. Starting from the conduction band, the electron can recombine with a hole. This process is shown as step 2 in Figure 3.1. As a result, visible blue TL-light is emitted in this so-called recombination center. A localized energy level can act either as trap or as recombination center. [33]

Since there are several traps with different ΔE at different energies, certain amounts of energy are needed to release electrons from traps. The probability to release an electron from a ΔE trap depends on temperature and is determined by the Boltzmann distribu-

tion:

$$p = \exp\left(-\frac{\Delta E}{k_B T}\right). \quad (3.1)$$

If the material is heated up after irradiation, electrons escape from different traps as described above. This effect increases with the temperature. As can also be deduced from Boltzmann statistics, the frequency of emptying of traps at one temperature is different for various traps.

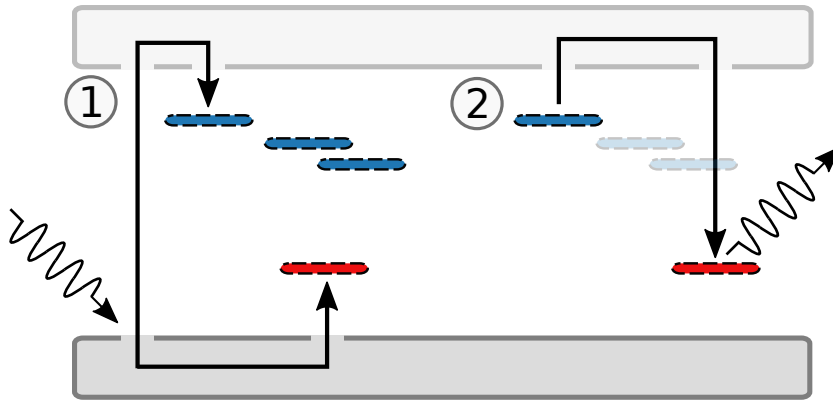


Figure 3.1: Schematic representation of the TL process in the band model. The valence band is shown in gray and the conduction band in white. 1) Energy from irradiation is stored. Electrons are trapped in the traps marked in blue and holes in the traps marked in red. 2) Energy is released during heating. Electrons and holes recombine and light in the blue-wavelength range is emitted. [34]

Due to the fact that only isolators and semiconductors have a band gap, only these can be TL materials.

The emitted TL-light is detected and the photons are counted. Usually the TL intensity is studied as function of temperature T or measurement time t to display the data. It results in a so-called glow curve, whose shape characterizes a TL material.

3.1.1 Glow curve of LiF:Mg,Ti

A glow curve of LiF:Mg,Ti, irradiated with photons to a dose of 5 mSv and measured at 573 K, is shown in Figure 3.2. A few mSv are a typical dose for investigations in the personal dosimetry range. In that figure a typical glow curve without significant storage time before or after the irradiation, featuring peaks 3–5, is reproduced. The peaks are numbered in the common nomenclature [35]. Peaks 1 and 2 are notably smaller than the other peaks due to their quick fading (see Section 3.1.3) and not visible in the figure. In most recorded glow curves, depending on the fading time, only the peaks 2–5 or 3–5 are

visible. The peaks are strongly overlapping with each other and each peak arises from a particular trapping-recombination mechanism [36, 37].

The probability of filling a trap and thus, also the intensity of an individual peak depends on the dose, so that the total integral of a glow curve is directly proportional to the irradiated dose.

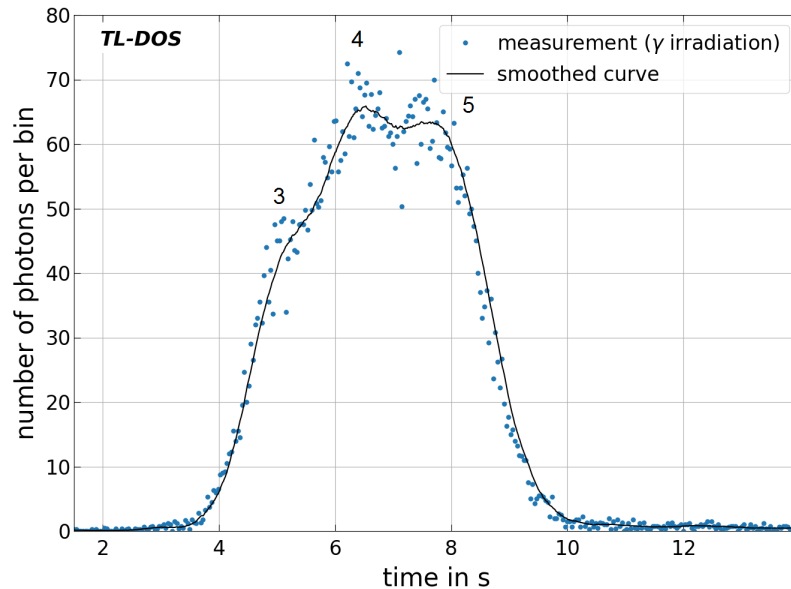


Figure 3.2: Typical glow curve from LiF:Mg,Ti measured at 573 K with exponential heating after a 5 mSv photon irradiation with ^{137}Cs . The smoothed curve is calculated to guide the eye and peaks are label with numbers. Glow peaks 3 through 5 in the common nomenclature [35] are visible. Peaks 1 and 2 are not visible due to the fading effect (explained in Section 3.1.3).

3.1.2 High temperature glow peaks

If there are many electrons in the conduction band at the same time, the probability to fill even deeper traps increases. This state can be achieved either by irradiation with a high dose or with particles that have a high ionization density. If the TL material is irradiated with such particles that have locally a higher ionization density than photons, such as alpha particles or neutrons, not only the peaks 3–5 become visible during measurement, but also peaks 6 and 7 occur. These glow peaks are only appear at higher temperatures ($> 573\text{ K}$) because the electrons need more energy to escape from these traps, they are called high-temperature peaks. An example of such a glow curve with peak 3–7 after alpha irradiation is shown in Figure 3.3.

In personal dosimetry peaks 6 and 7 are also called high-LET peaks, because they depend on the LET of irradiation particle and are mainly visible after alpha or neutron irradiation

which have a high LET. [38]

For many dosimeter systems, these additional high-LET peaks are neglected but they offer prospects of additional information from the glow curve. For this reason, the TL-DOS neutron dosimeter (Chapter 3.3) is designed to measure these peaks.

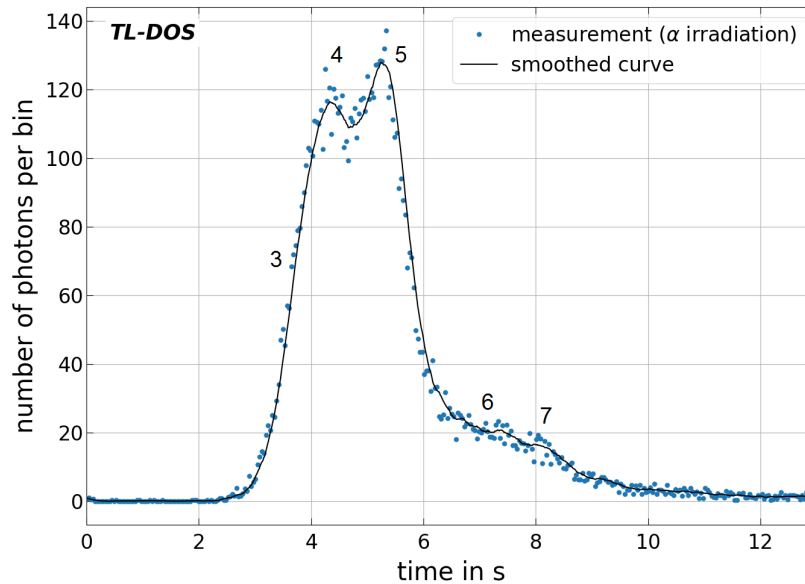


Figure 3.3: Typical glow curve from LiF:Mg,Ti measured at 653K with exponential heating after an alpha irradiation (^{241}Am) for 640 s. The smoothed curve is calculated to guide the eye and peaks are labeled with numbers. Glow peaks 3 through 7 in the common nomenclature [35] are visible. The signal gain (6+7) compared to a photon glow curve is notable.

3.1.3 Fading and re-trapping effects of thermoluminescence materials

Thermoluminescence has also undesirable effects. The most common and important effect is post-irradiation fading. The Boltzmann distribution shows that even at room temperature, escaping electrons from traps and so recombination of electrons is not negligible. As a result, the signal of the individual peaks decreases over time until it disappears completely. Fading effects of the TL-DOS system have already been examined in Refs. [39] and [40].

Each trap, can be assigned a certain half-life at room temperature. States that require less energy to detrapp 'fads' faster than those deeper in the band gap. For peaks 1 and 2 the half-life is of the order of minutes, whereas the half-life of stable peaks (4-5) is amounts to years. To compensate this effect, there are different methods in measurement technology (see Chapter 3.3), e.g. various pre- or post-heating steps, or the glow curve

analysis [34].

Another effect that should be suppressed is the rearrangement of electrons in the traps after irradiation. After an electron has escaped from a trap, it can not only be recombined but also directly trapped in a trap again. This effect is referred to as re-trapping.

In addition, there is also the pre-irradiation fading. The shape of the glow curve changes depending on the storage time before an irradiation. The behavior of the individual peaks correlates strictly with the heating profile before an irradiation. A possible explanation for this effect is that the multiple defective structures of deeper traps are composed of the shallow ones, which can cluster to deeper traps [37]. This cluster phenomenon depends on the heating treatment before an irradiation and can also be eliminated by suitable measurement programs including further steps before the readout.

3.2 TL-DOS neutron detectors

After the general physical principle of TL has been introduced in Chapter 3.1, the TL-DOS detectors are presented in the following. The choice of TL material, the production of detectors and tests of the neutron sensitive TL detectors are discussed. Lithium fluoride doped with magnesium and titanium is used as sensitive material for the TL-DOS system. It is widely used in dosimeter applications due to its tissue similarity and flat energy response for photon irradiations.

3.2.1 Sensitive material LiF:Mg,Ti and its neutron cross section

While standard photon TL-DOS detectors apply LiF:Mg,Ti (MT-N) as TL material, for the neutron dosimeter two different isotopic compositions, enriched in Li-6 (MT-6) and in Li-7 (MT-7), are used. This is necessary to use the albedo principle to overcome the challenge that neutron fields are always mixed fields (see Chapters 2.5, 2.6). On the one hand detectors are produced with the neutron and photon sensitive material MT-6 and on the other hand MT-7 detectors which are almost only sensitive to photon radiation are produced. For distinction, the detectors are referred to as Li-6 and Li-7 detectors in all following chapters. The natural Li (Li-N) consists of 93% Li-7 and 7% Li-6 which would mainly measure the photons. [41]

The neutron cross sections σ of the two materials are shown in Figure 3.4 (left). This figure illustrates that Li-6 is much more sensitive to neutrons as Li-7. The dominant process of

the Li-6 is neutron capture (Section 2.2.2), where an alpha particle is generated [11]:



This alpha particle induces the signal in the material. For smaller neutron energies there is more signal in the detector than for higher energies, because the probability of an interaction is higher (compare dosimeter response in Chapter 2.5). In comparison to Li-6, the cross section of the Li-7 is significantly lower and close to 1 barn. It means that neutron radiation hardly induces any signal on a Li-7 detector. The difference between both materials is shown in Figure 3.4 (right). Thus, both LiF:Mg,Ti signals can be subtracted from each other for neutron dose estimation. With this method neutron and photon separation works best for thermal neutrons, because the difference is largest in the range of thermal neutrons.

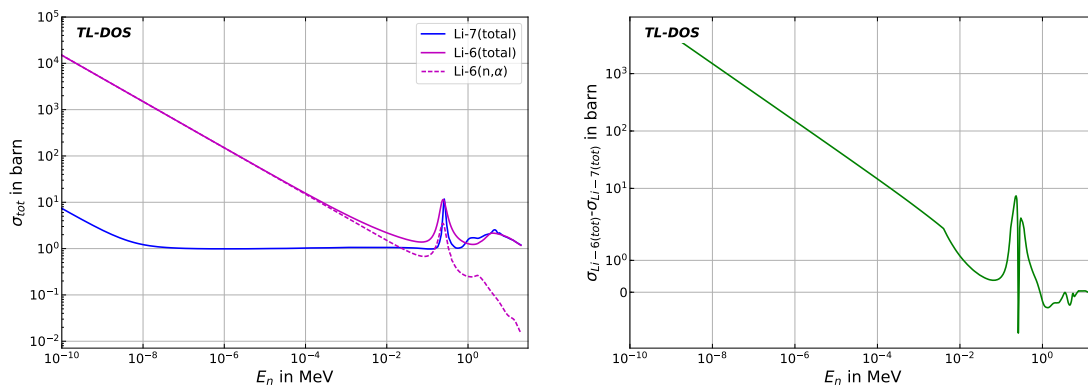


Figure 3.4: Left: Neutron cross section for both detector TL materials depending on the energy. The neutron cross section of Li-6 is separated in neutron capture (dotted) and total cross section (line). Right: Difference of the Li-6 and Li-7 cross section in dependence of the energy. Data extracted from [42].

3.2.2 Design of a TL-DOS detector

At the beginning of a standard TL-DOS detector production a ceramic layer is sprayed onto an aluminum carrier plate by flame spraying to reduce thermal radiation from the plate during heating for the readout process. Depending on the detector type, an amount between 1-15 mg of LiF:Mg,Ti is hot sintered onto the substrate. For neutron detectors, the Li-6 or Li-7 can be applied either as powder form or as solid chips. The form

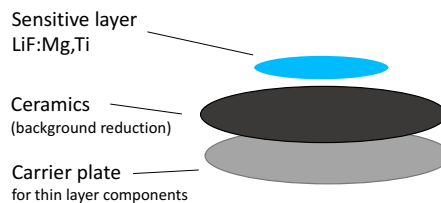


Figure 3.5: Schematic of a TL-DOS detector with its individual layers produced in different production steps.

of the sensitive material to be used in the future is discussed in the following chapter. In addition, a barcode is written on the backside of the carrier plate with a laser to uniquely identify the detectors. While standard TL-DOS detectors have a diameter of 17 mm, neutron detectors have an adapted one of 10 mm. It is modified since four detectors are needed in one dosimeter badge to estimate the neutron dose.

3.2.3 LiF:Mg,Ti in powder or chip form

On a base detector chip the sensitive TL-material can be applied either in chip or in powder form. During this process the amount of LiF:Mg,Ti can be defined.

Detectors with 25 mg LiF:Mg,Ti in chip form were produced and compared to TL-DOS detectors with 10 mg LiF:Mg,Ti as powder. 10 mg is the optimum value in terms of large signal yield and maximum space on the aluminum carrier. Both types are manufactured with the same material and same standard procedure.

Chips are cheaper, more readily available and consist of a larger amount and a thicker layer of TL-material than powder-detectors, but the hot-sinter process for this form would have to be revised because pieces of the chip would crumble or flake off through repeated use. During the handling of the detectors they are mechanically damaged in addition to the non-optimized sinter process.

The production of detectors with powder can be controlled better and yields high quality detectors. The system is designed for this process as standard, which ensures due to experience in Ref. [43] that the powder remains on the carrier. However, not many vendors exist for Li-6 powder and it is expensive. For first tests chips were crushed to produce powder to study which configuration is best while using the same material.

A signal dose linearity is verified for both detector configurations described for Li-6 and Li-7 types. Per type, 6–8 detectors are irradiated with doses between 1 mSv and 10 mSv at the ^{137}Cs facility of the MPA NRW. Each dose is measured four times. The mean values of the measured counts and its standard deviation are determined and graphically presented in Figure 3.7. Linear functions are fitted to the data.

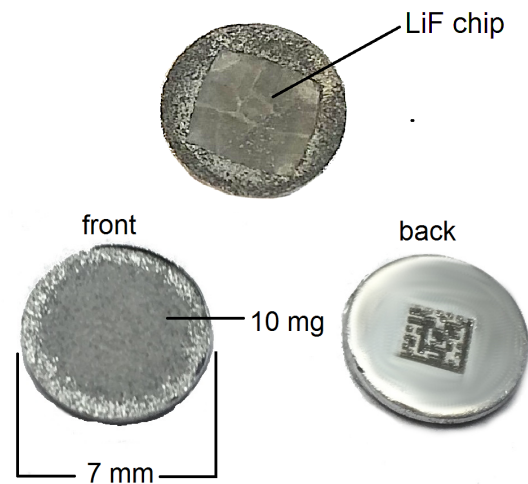


Figure 3.6: Front and back side of TL-DOS detectors with different material configurations. Above: with LiF:Mg,Ti in chip form. Bottom: with LiF:Mg,Ti as powder. A barcode is visible on the backside of the detector.

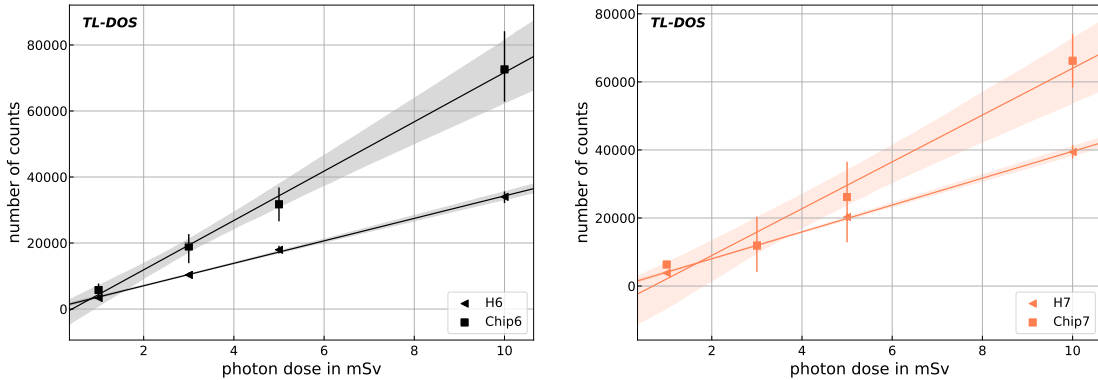


Figure 3.7: Signal-to-dose linearity for detectors produced with LiF:Mg,Ti in chip form and LiF:Mg,Ti in powder form (H6,H7). All were irradiated with the ^{137}Cs facility. Left: for detectors with Li-6 as sensitive TL-material. Right: for detectors with Li-7 as sensitive material.

On the one hand, the gradients of chip detectors is significantly larger than the gradients of typical TL-DOS powder detectors for both LiF:Mg,Ti types, because chip detectors consist of more than twice as much sensitive material. On the other hand, the measured values of chip detectors scatter much more strongly. One possible reason is the fact that there is less material on a detector from measurement to measurement because the sensitive material crumbles. This amount of material is undefined and varies for all detectors because the production procedure is not optimized for chip detectors.

In the final design, the TL-DOS neutron detectors will be produced with the standard powder method. The powder is applied in a thin layer (250 μm) to the aluminum carrier resulting in a minor effect of self-absorption to achieve an optimal measurement of TL signal. The cross-section of a detector is illustrated in Figure 3.8 to exemplify the distribution.



Figure 3.8: Cross-section of a neutron TL-DOS detector produced with LiF:Mg,Ti in powder configuration. The detector is cut in the middle by a laser.

3.2.4 Different manufacturers and kinds of LiF:Mg,Ti

LiF:Mg,Ti is mainly produced by two different companies whereby both materials have partly different characteristics. Powder for the TL-DOS dosimetry system is usually sourced from Radpro in Poland. For the neutron system powder is also tested from the American manufacturer Harshaw. This powder is used for most commercial neutron

systems. The materials differ in their production process, so that the materials may have different properties. While Harshaw sells TLD-600 and TLD-700 (in the plots: H6,H7) [44], MT-6 and MT-7 is distributed by Radpro.

The comparison of both types is based on measurements of signal dose linearity. Data for both types of powder are recorded as described in Section 3.2.3. The results are shown as mean and its standard deviation depending on the photon dose in Figure 3.9.

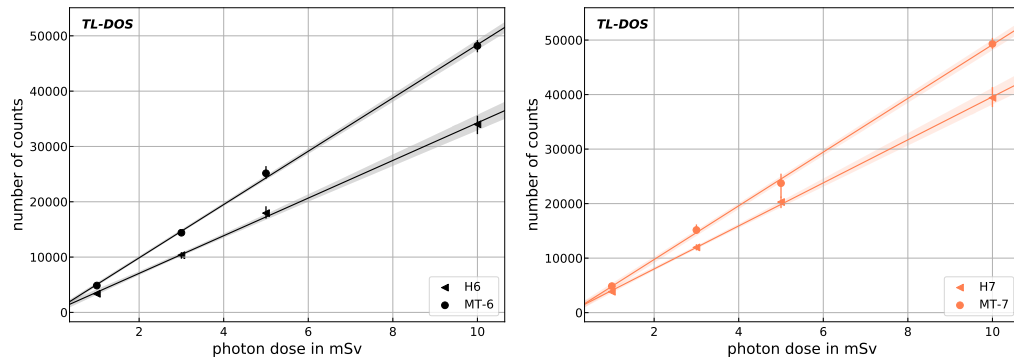


Figure 3.9: Signal-to-dose linearity for detectors produced with TLD-600 and TLD-700 (H6 and H7) and MT-6 and MT-7. All were irradiated with the ^{137}Cs facility. Left: for detectors with Li-6 as sensitive TL-material Right: for detectors with Li-7 as sensitive material.

The detectors produced with MT-6/MT-7 powder are about 35% more sensitive than TLD-600/TLD-700 detectors. Similar results are found for both material types.

Since the detector sensitivity is optimized with powder from Radpro and other TL-DOS dosimeters use MT-N powder, the material of this company is chosen for the neutron detector applications in future. The advantages are a high sensitivity what results in a better detection of small doses.

Thus, the final design of 7 mm diameter TL-DOS detectors with MT-6 and MT-7 in powder form is optimized for use in the TL-DOS system.

3.2.5 Background of TL-DOS neutron detectors

Li-6, Li-7 and standard TL-DOS detectors (Li-N) are evaluated directly after a signal erasing step, so that only background is measured. The Figure 3.10 compares the two detectors (Li-6, Li-7) used for the neutron dosimeter with standard TL-DOS detectors. The results of ten measurements are shown for each type as box plot with its median and the first and third quartiles marked as box. 25% of the values are lower as the first quartile. The minimum and maximum counts are marked as whiskers.

The background measured for Li-6 and Li-7 detectors is similar than for standard Li-N one ([45]), justifying their use in the TL-DOS system regarding the background.

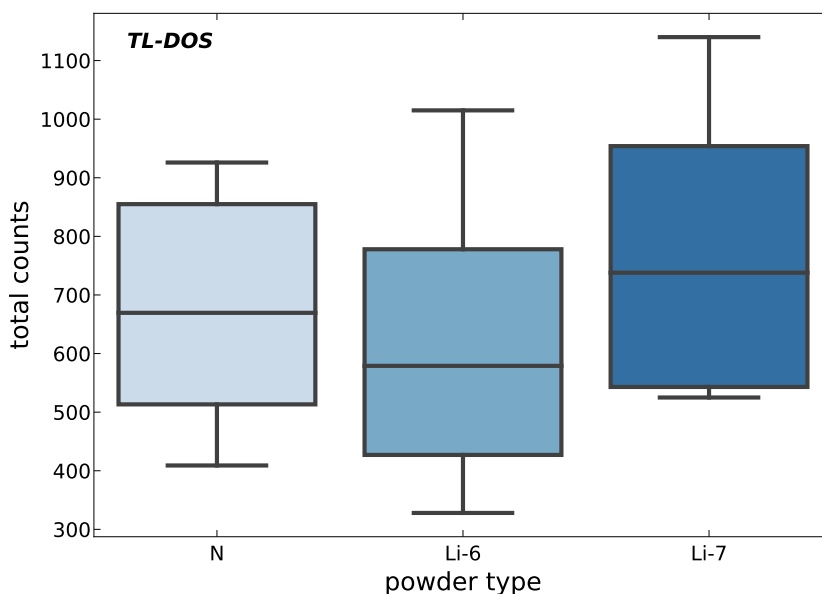


Figure 3.10: Background of detectors: Total number of counts presented as median and quartiles for three different detector types measured for 15 s directly after erasing them.

3.3 TL-DOS prototype readout device

For all measurements in this thesis the TL-DOS prototype readout device is used. It is a compact system integrating several stations with different tasks. The whole device is referred to as reader and is shown in Figure 3.11.

The carousel (A) can be equipped with up to 32 detectors, where they are identified by a bar-code scanner (B). With the help of the robot pincer (C) a detector can be transported from the carousel to any of the three main stations (D, E, F). First, the detector is placed in the pre-heating unit (D) which consists of one heating plate and one plate at room temperature. At this station a detector is heated for 10 s at 428 K to compensate for thermal fading (see Section 3.1.3). This step erases the first peaks (1,2 and a part of 3) of the glow curve, so that only the stable long-lived peaks of a glow curve remain. To stop this process it is cooled for 3 s while lying on the plate with room temperature. In a second step, the detector enters the measuring unit (E). There it is pushed onto a hot plate so that it heats up exponentially and emits TL-light. This light is measured by a photo multiplier tube (PMT) after passing through corresponding optics and optical filters. Usually, the hot plate of the measuring station is operated at a constant temperature of $T = 573\text{ K}$ for measurements after photon irradiations, but can be varied up to $T = 653\text{ K}$. After a 15 s measuring process, at last the detectors are heated in the heating station (F) for 15 s at 673 K and cooled down to room temperature for 15 s. If signal is still stored on the detector after the measurement, the signal is completely erased in this

step. [46]

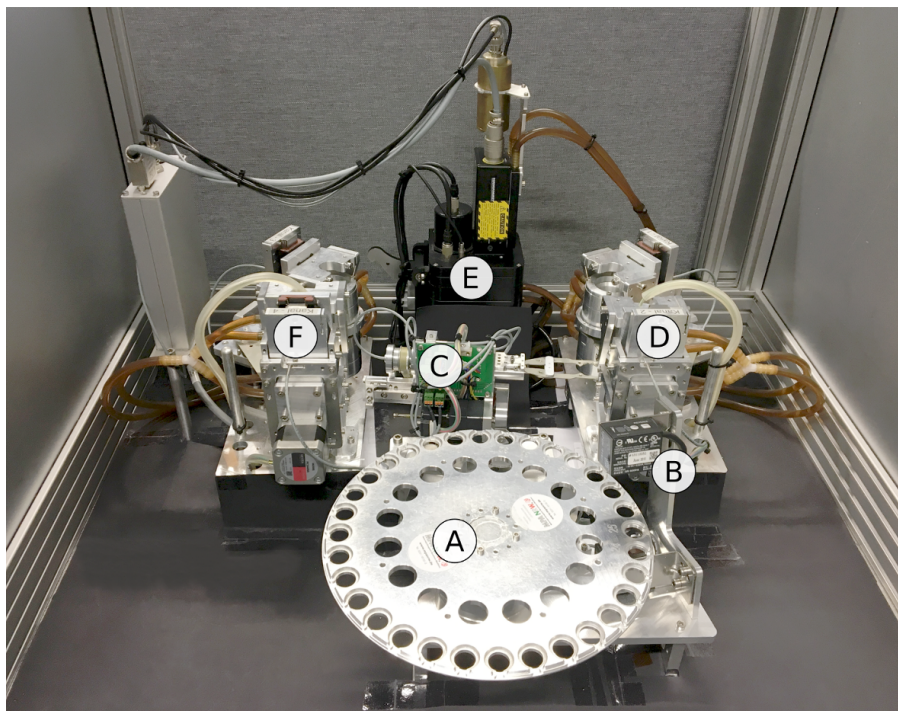


Figure 3.11: The compact readout device, TL-DOS reader, with its components: A) carousel, B) bar-code scanner, C) robot pincer for transport, D) pre-heating unit at 428 K, E) main readout unit featuring a heating plate at a constant temperature (usually $T=573$ K) and F) heating station to erase all signal of a detector.

3.3.1 Adapter for readout of neutron detectors

The TL-DOS reader has been developed for whole body detectors [47, 48] with a diameter of 17 mm, see Figure 3.12 (second object from the right). The neutron detectors are smaller and thinner than other TL-DOS detectors. They have a diameter of only 7 mm compared to 17 mm.

In order to be able to read all detectors with the same device, they are placed in a so-called adapter [49], see Figure 3.12 (left). This combination has the same thickness and size as a TL-DOS whole body detector, so that all mechanical steps can be passed through in the reader.

In contrast to the standard detectors, the neutron detectors are not firmly connected to their adapter and have a smaller sensitive layer. Therefore, the heat transfer of the hot plate to the adapter and the sensitive material during readout is investigated in the following.



Figure 3.12: From left to right: One TL-DOS adapter in combination with a neutron detector, only an adapter for readout of small elements with the TL-DOS standard reader, standard TL-DOS whole body detector, 1 cent coin to compare all sizes.

Heat transfer: adapter vs. standard detector

Glow-curve measurements of adapters and standard detectors are performed to investigate the heat transfer of the adapter method. Glow curves of these measurements are recorded to compare them with each other. Logging the detector temperature during a measurement is technically not possible.

As an alternative to get information about the heat transfer, the area in which the glow curve is visible, called region of interest (RoI), is calculated (see Chapter 3.6) to estimate the end of the glow curve for 35 measurements as a function of the heating time each. The data are shown as box plot in Figure 3.13.

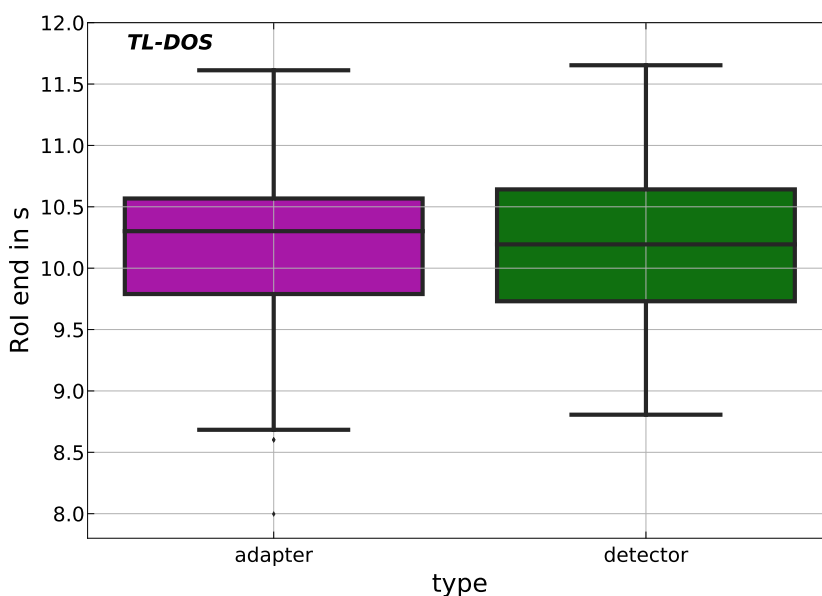


Figure 3.13: End of the glow-curve region for detector and adapter measurements. Both are irradiated with 5 mSv ^{137}Cs , pre-heated at 428 K and measured at 573 K.

The standard detector already reaches its glow-curve end after (10.2 ± 0.1) s averaged.

For measurements when using an adapter it is accomplished approximately after a similar time. The results for adapter technique and detectors are in a good agreement within the uncertainties. According to previous studies in the TL-DOS project it is common to read out the detectors for 15 s. It is confirmed that this time is sufficient as a measurement period for both and is thus specified for the neutron dosimeter as well. The similar ending time indicates that it is not necessary to increase the measurement time in order to get a longer heating transfer.

3.3.2 Optimization of the temperature profile

While standard TL-DOS detectors are read out at 573 K, this temperature is not sufficient for neutron detectors. Figure 3.14 (left) shows a signal recorded after neutron irradiation at $T = 573$ K. From about 12 s the signal runs in a plateau due to the incomplete read out of the glow curve. No clear glow peak is formed but a constant higher signal than background because the measuring temperature is too low to release all trapped electrons. To ensure also the readout of additional traps during measurement, the temperature is increased to $T = 653$ K.

If detectors including the filled deeper traps are read out at $T = 653$ K, the high temperature peaks (6+7) appear in the glow curve (Figure 3.3). This means that more signal is measured and no information of the additional peaks gets lost. Further peaks cannot be found in the glow curve, because they would be indistinguishable from the background.

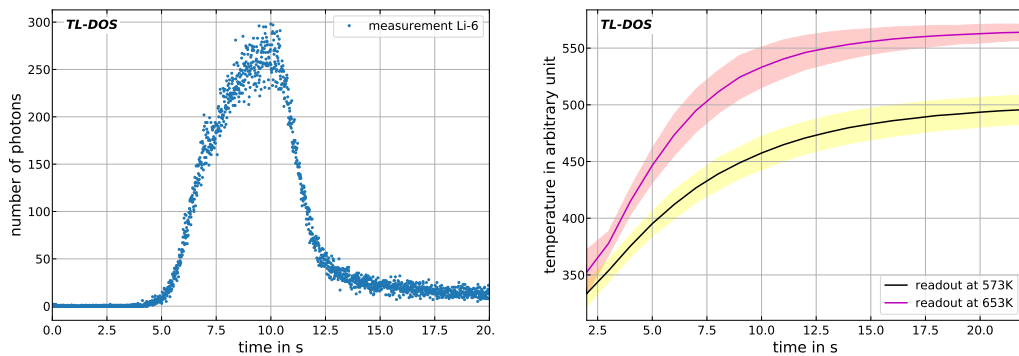


Figure 3.14: Left: A glow curve measured at $T=573$ K after an irradiation with neutrons is shown. Note that the signal has not been read out completely. Right: Temperature measurements of detectors during the readout step at two different temperatures performed with an infra-red sensor. The same setup is used for both scenarios.

An advantage of the temperature increase is the resulting higher heating rate $\beta = dT/dt$. It means that the glow curve is recorded faster.

Further measurements of the neutron detectors have been performed with an infra-red sensor once for the measurement process $T = 573$ K and once for $T = 653$ K. The

measurements were repeated ten times in succession and the averaged data are shown together with their error band in Figure 3.14 (right). The temperatures are given in arbitrary units because no calibration of the infra-red sensor is available. However, the two curves are comparable as both were measured with the same setup. As expected a larger heating rate is found for higher temperatures.

Besides the time gain the temperature increase has a negative effect as well. Due to blackbody radiation, the background increases when measuring an empty detector. This rise is defined by the Stefan–Boltzmann law:

$$P = \sigma \cdot A \cdot T^4. \quad (3.3)$$

To specify the increase 5–8 unirradiated detectors are measured for six different temperatures. The background rises exponentially with rising temperature, see Figure 3.15. This undesired effect is studied to be minimized by suitable methods in order to separate signal from background. Therefore, background reducing filters are discussed in the next chapter.

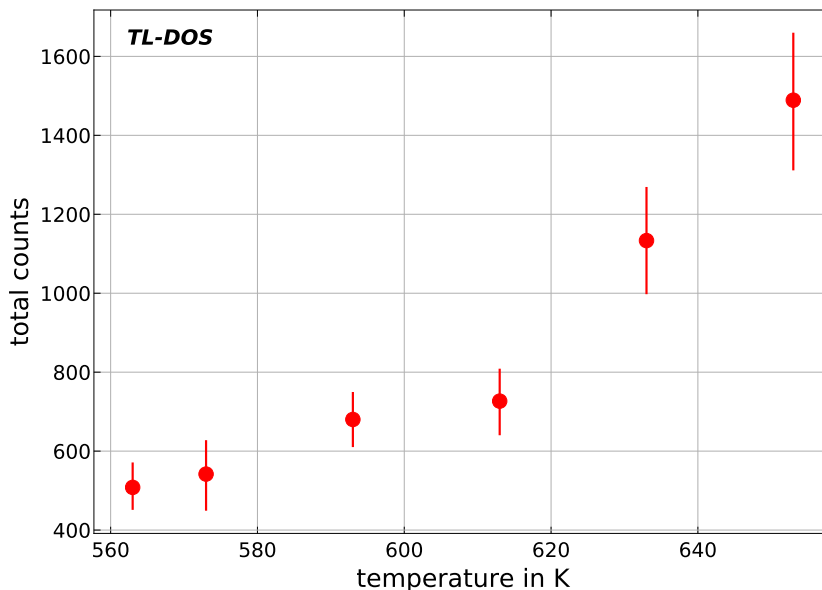


Figure 3.15: Background for different measurement temperatures when measuring unirradiated detectors with the standard TL-DOS reader.

3.3.3 Reduction of background with optical filters

As TL-DOS standard, a blue color filter FD1B [50] is included in the optics in front of the PMT. By an optical filter light of a certain wavelength is transmitted and other

wavelengths are cut off. In case of the TL-DOS system, wavelengths that would contribute to background are cut off. The transmission spectrum of the filter determines which wavelengths are transmitted. An FD1B filter transmits light particularly well in the blue wavelength range.

In Ref. [51] best results for background reduction were found for the combination of one FD1B and one BG40 filter [52]. A filter combination, which ensures good transmission for TL-light (emission maximum around 400 nm [53]) and largely shields the rest of the spectrum, was looked for. A BG40 filter helps to eliminate wavelengths above 750 nm.

Before the optical filter BG40 is added to the measuring unit of the reader, some test measurements are carried out. Measurements are performed without detectors to measure the background of the reader, with detectors and with irradiated detectors. Table 3.1 lists all combinations measured at different temperatures with and without the filter.

Table 3.1: Setup combinations to check the filter BG40 installation with different parameters like measurement temperature, filter and irradiation source. Two scenarios are measured without detectors to test only the background of the reader.

number	temperature T in K	with or without filter	irradiation
1	653	without	without detector
2	653	with	without detector
3	653	without	no
4	653	with	no
5	573	with	^{137}Cs
6	653	with	^{137}Cs
7	573	without	^{137}Cs
8	653	without	^{137}Cs
9	653	without	$^{241}\text{Am}+^{137}\text{Cs}$
10	653	with	$^{241}\text{Am}+^{137}\text{Cs}$

With the BG40 filter an improvement of the background number of photons by 96% is found for background measurements without detectors. The background of measurements with detectors is also reduced by 74% with an additional filter.

Figure 3.16 shows two background measurements without a detector. The data without the additional filter are marked in red and the data recorded with an installed BG40 filter are shown in blue. A background decrease is clearly visible.

It is reasonable to assume that not only background but also desirable signal is reduced. For detectors irradiated with ^{137}Cs , the filter yields following values for glow curve integrals compared to glow curves measured without this filter:

$$\begin{aligned}
 573 \text{ K} : & \quad (89 \pm 15)\%, \\
 653 \text{ K} : & \quad (90 \pm 10)\%.
 \end{aligned}$$

After alpha irradiation, very similar results for the glow curves are determined using the BG40 filter as well:

$$653\text{ K} : (91 \pm 10)\%.$$

The uncertainty is large and in agreement with 100%. In addition, the PMT lost about 6% of its sensitivity within ten days in which the data are recorded. This decrease is not included in the above mentioned percentages. As the measurements with the BG40 filter were performed at a later time, they have to be corrected. More details about the decrease effect will be discussed in the next chapter.

Due to the large uncertainty and the sensitivity-decrease effect of the PMT, the possible signal reduction is not considered for the decision to use or not to use the BG40 filter.

Although the BG40 filter cuts off only a small amount of TL-signal, it is useful and improves the signal-to-background ratio significantly. In summary, this filter is installed for the TL-DOS neutron dosimeter system and used for all further measurements. Thus, the background is reduced resulting in a more robust dose estimation of detectors with unknown irradiation.

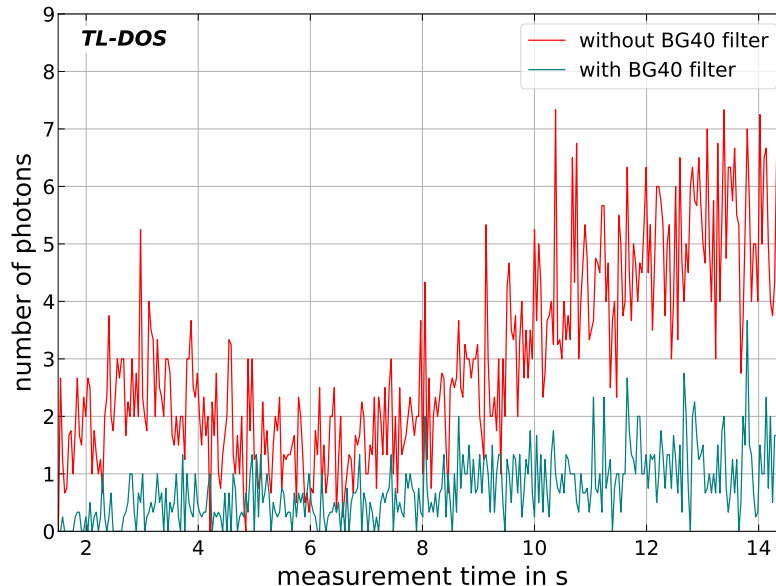


Figure 3.16: Smoothed data of two measurements of reader background calculated by Savitzky-Golay-filter (Ref. [54]). Measured at 653K with a FD18 filter, with and without the additional BG40 filter.

3.3.4 Sensitivity decrease of the readout system

In the past, an undesirable effect of the measuring unit was observed: The PMT sensitivity decreases with time and the number of measurements [34, 47].

To specify and quantify this effect, a group of dedicated 20 detectors referred to as control group is defined. This group is irradiated once a week, after 400 d only once a month, with a dose of 5 mSv with the ^{137}Cs facility and read out with this reader. The average of the glow curves, after background subtraction, are shown in Figure 3.17. The error bars show the standard error of mean. Before read out, the detectors were pre-heated as discussed in Section 3.3.

During the measurement campaign the control group was upgraded from R14 to R16 detectors with respect to the current production status whose procedure is in a permanent development. The corresponding data is marked in blue (R14) and green (R16) points. In a transition phase, both groups of 20 detectors respectively were measured to distinguish possible detector effects from PMT behavior.

Especially at the beginning (first 300 d) an exponential decay is found. For the last 150 days the signal can be assumed to be constant. When considering the individual peaks instead of the integral, the same conclusion is drawn.

Later measurements are corrected for this decrease of the PMT output.

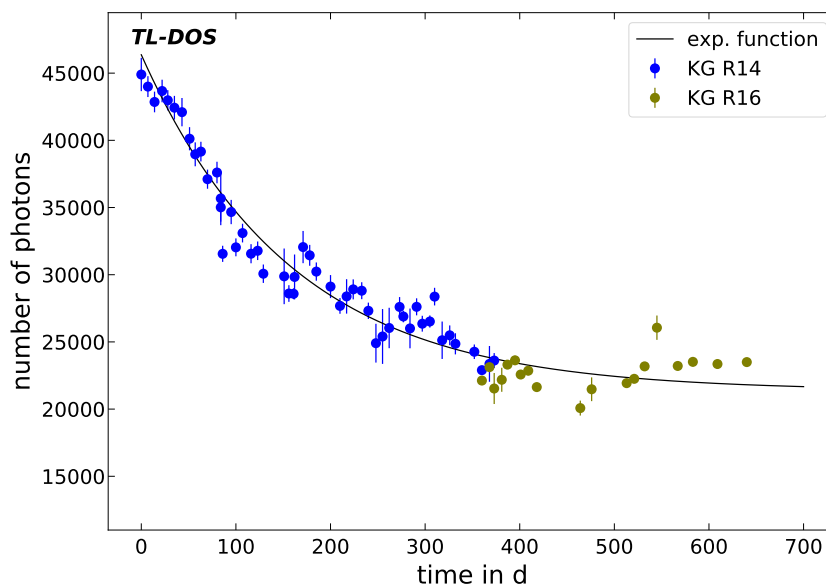


Figure 3.17: Data of all control group measurements between May 2017 and April 2019. All detectors are irradiated with ^{137}Cs , pre-heated at 428 K and measured at 573 K. R14 and R16 are two different groups of detectors. R16 are detector with a higher production standard. An exponential function is fitted to the data. The data until 150 days are adopted from Ref. [47].

In addition, different dates are marked in Figure 3.18 (enlarged section of Figure 3.17). While the time of moving the reader to another building with a different nitrogen supply is shown in cyan, the day of the filter installation (see Section 3.3.3) is marked in violet. One reader cleaning is marked in black. During cleaning, the entrance window to the reader optics is cleaned so that it is more permeable. After all marked times, no significant change of the signal level is detected in the data directly after this step. Thus, it is concluded that the sensitivity of the PMT decreases with time.

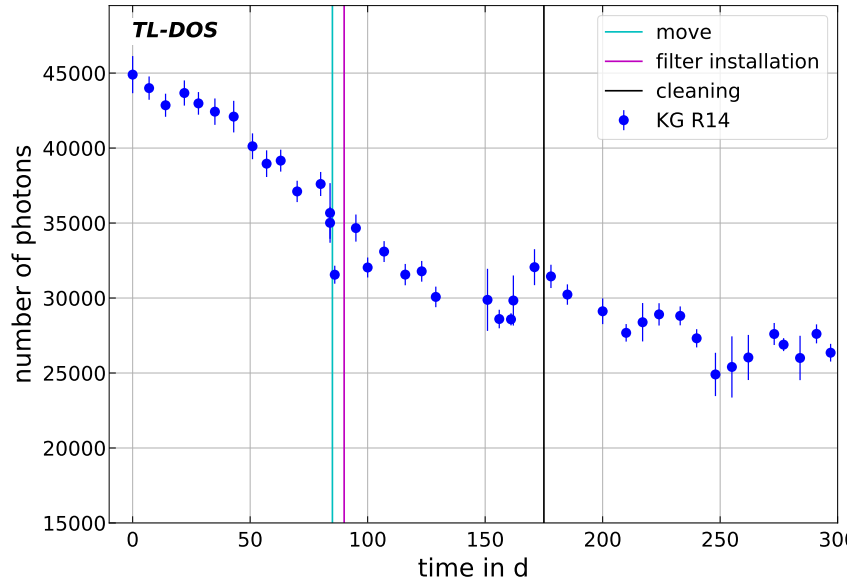


Figure 3.18: A section of the control group data (see Fig. 3.17) with different distinctive points like cleanings, reader move and the installation of the BG40 filter (tested in Section 3.3.3).

3.4 TL-DOS albedo dosemeter badge

The TL-DOS neutron dosemeter consists of four detectors within a badge using the albedo principle, see Chapter 2.6.

While two field detectors in a carrier card detect the radiation from the field, two further detectors, the so-called albedo detectors, measure the backscattered radiation of the body (see Section 2.6). Therefore, two of the detectors in a carrier card face the front and two face the back, see Figure 3.19 (left), because the detectors have a preferred measuring direction. The card has a barcode number so that it is uniquely identifiable. Since each pair (field and albedo) consists of a Li-6 and a Li-7 detector, the field and albedo neutron dose can be calculated by subtracting both signals (equation (2.11)).

The carrier card is inserted into an albedo badge developed at the TU Dresden [55].

Figure 3.19 (right) shows such a badge with its two entry windows for the field detectors. Inside there are two filters consisting of boral (Figure 3.19 (middle)), each is designed to protect the detectors from radiation from the other direction. In this way the detectors measure approximately only the field respectively only the albedo radiation. Boral has a high number of protons, a large effective cross section for neutron radiation. Therefore, it is a good material for neutron shielding. Other materials for example boron nitrite were investigated in Ref. [56] and boral was confirmed as best material.

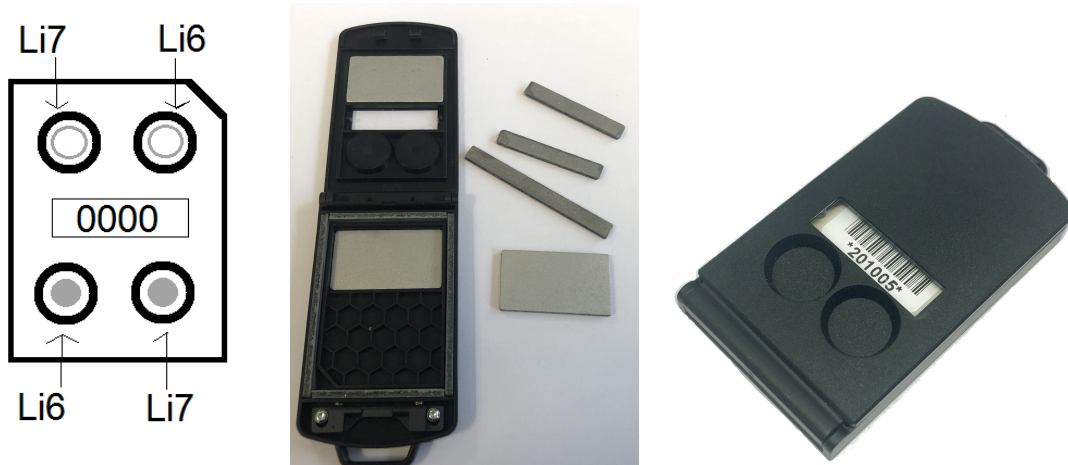


Figure 3.19: Left: Schematic of a carrier card with four TL-DOS detectors. Middle: Open albedo badge with boral filters for shielding detectors. Right: Closed albedo badge with two entry windows.

3.5 Detector and dosemeter calibration with Caesium-137

Before a dose is calculated from the measured values of a neutron dosemeter, the four detectors of one badge are calibrated. In this thesis the calibration of the detectors is performed with the ^{137}Cs facility of the MPA NRW. ^{137}Cs is a widespread calibration source, because it has approximately a monoenergetic energy spectrum. It emits 662 keV gammas and also beta radiation, whereby the latter can be neglected at the facility used because the beta irradiation is shielded.

A calibration has to be performed under well known conditions that are set the same for all detectors and are repeatable. In this chapter parameters like the readout temperature, a calibration function and a so-called frame factor due to badge influences are defined to specify the calibration scenario for the TL-DOS neutron dosemeters.

3.5.1 Readout temperature for calibration measurements

As already described in Chapter 3.3, measurements of neutron detectors are usually performed at 653 K to make all peaks visible. However, during construction, the reader has been optimized for measurements at 573 K and is therefore more reliable at this temperature. For this reason, it is more practical to calibrate all detectors at 573 K instead of 653 K. Furthermore, the high temperature peaks are hardly visible after gamma irradiation like ^{137}Cs in personal dosimetry dose range. In comparison to peak 5, the intensity of the high temperature peaks is negligible and cannot be separated from the background for gamma irradiations in this range.

To find a suitable temperature 18 detectors (nine Li-6 and nine Li-7) are irradiated with 5 mSv ^{137}Cs and measured at 573 K. The same detectors are irradiated once again but measured at 653 K this time. The results are shown as a box plot in Figure 3.20. The median and quartile for the total signal, the gross signal (the range where the glow curve is visible) and the net signal (after background subtraction) are plotted against the readout temperature. The total integral is significantly higher for 653 K, as the background is increased due to the black body radiation (see Figure 3.15). Usually the net integral is used for the evaluation of the data.

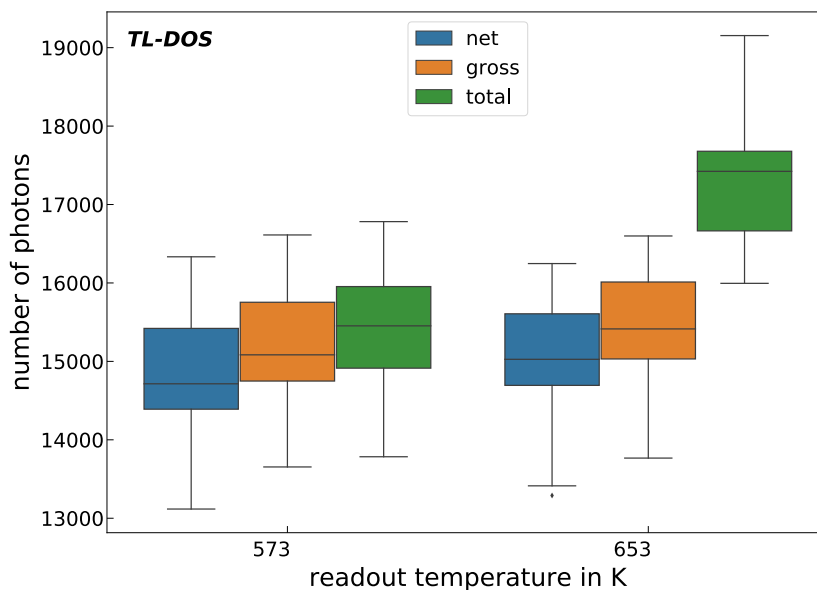


Figure 3.20: Number of photons with its median and quartiles for three different integrals of a glow curve for two readout temperatures. All detectors are irradiated with photons and are pre-heated before measuring them. The median of the net signal of the higher T is only 1% higher.

It is evident that it does not matter at which of the two temperatures the detector is read

out after the background is subtracted. For the higher temperature (653 K) the median is a bit higher but both (573 K and 653 K) are still in agreement with the quartiles. For measurements at 573 K a standard deviation of 6% is found and it results in 5% for a readout at $T = 653$ K. It is in the same range for both temperature. Thus, the neutron detectors are calibrated at 573 K in the following.

3.5.2 Li-6 and Li-7 calibration functions

The TL-DOS neutron dosimeter consists of two different detector types, Li-6 and Li-7. Either they can be treated equally, or two calibrations have to be determined. In Figure 3.21, the results of ten detectors, each irradiated four times with four different doses, are averaged and a linear function is fitted to the data. The Li-6, Li-7 and Li-N detectors are compared with each other based on the recorded signal dose linearity (Figure 3.21).

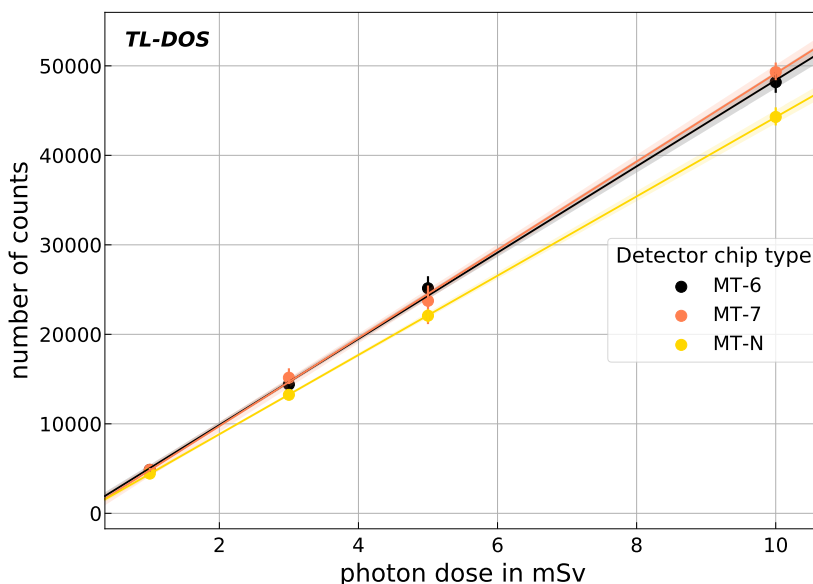


Figure 3.21: Signals for three different TL-DOS detector types as function of dose. All are irradiated with ^{137}Cs , pre-heated and measured at 573 K. Additionally, linear functions are fitted to the data.

The lines of the Li-6 and Li-7 detectors are close together. The gradients m agree within the uncertainties:

$$\begin{aligned}
 m_6 &= (4684 \pm 64) \frac{1}{\text{mSv}}, \\
 m_7 &= (4789 \pm 63) \frac{1}{\text{mSv}}, \\
 m_N &= (4429 \pm 42) \frac{1}{\text{mSv}}.
 \end{aligned}$$

The data of Li-N detectors has the lowest signal response for all values and results in the smallest m . Measurements with this type have to be calibrated separately.

A possible reason for this phenomenon is the particle size of powder. While Li-N powder has a particle size of $68\ \mu\text{m}$ – $80\ \mu\text{m}$, the grain size for Li-6 and Li-7 is larger with $60\ \mu\text{m}$ – $200\ \mu\text{m}$ [57]. As this range of grain size covers a larger interval, the sensitivity might be different for these detector types [49].

The two detectors used for the neutron dosimeter could be calibrated with one function. Although the calibration functions for Li-6 and Li-7 are in reasonable agreement, separate curves are used for all evaluations in this thesis to achieve a more precise dose estimation. The impact of individual detector calibration and a common group calibration is studied in Section 4.2.2.

If the time between calibration and measurement is long, the signal is corrected (see Chapter 3.3.4) to take the signal decrease of the PMT into account. An example for the application of an older calibration to newly measured data is shown in Figure 3.22. The data of the control group and times of calibration (green) and measurement (red) are shown.

For these two measurements the signal results in different number of photons. During the evaluation of the measurement data the signal has to be corrected, see Section 3.3.4.

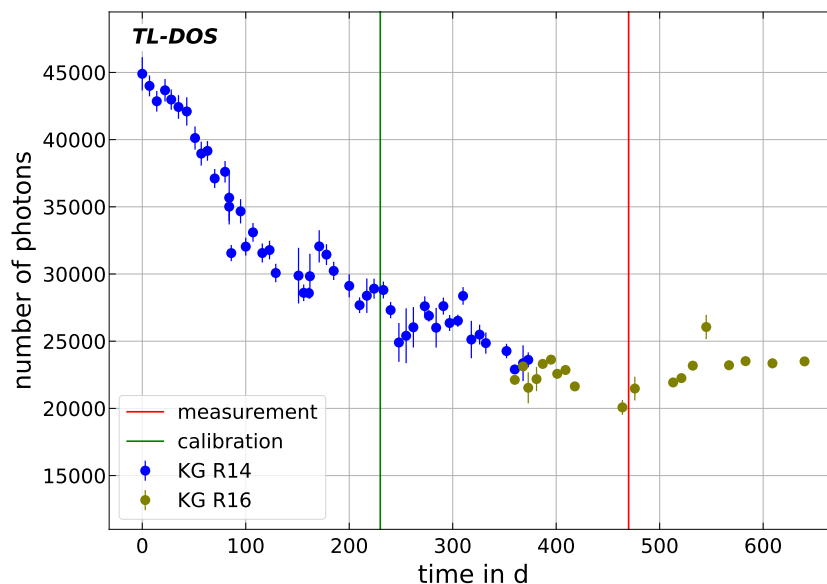


Figure 3.22: Data of the detector control group (see Fig. 3.17) with a calibration and a measurement time. It should be noted that the data need to be corrected before analysis because of the signal decrease. It is a part of the calibration procedure.

3.5.3 Frame factor k_{fb}

Parameters for bare detector calibrations are defined in the chapter above, but a dosimeter badge and the human body (or the phantom) also have an influence on the signal and have to be considered. During irradiation, a badge including detectors is placed on a phantom to measure the $H_p(10)$ dose and is not irradiated free in air. Therefore, the calibration of bare detectors is not sufficient. So the whole calibration usually is performed with a badge on the $H_p(10)$ phantom.

Calibrating all detectors in a badge on the phantom is complicated and time consuming for routine usage. Especially, there are two possible positions for each detector in a neutron dosimeter, which have to be calibrated individually. To irradiate only a few detectors during one run a lot of detectors have to be packed and unpacked in badges. Irradiation in an irradiation frame consisting of 16.5 cm x 16.5 cm PMMA is much faster because up to 50 detectors are irradiated at once. Therefore, a conversion factor k_{fb} is introduced and determined, which converts a calibration in frame into a calibration in badge. This allows the using of a frame calibration for the neutron dosimeter in the future. Figure 3.23 shows how the factor k_{fb} is calculated for TL-DOS detectors.

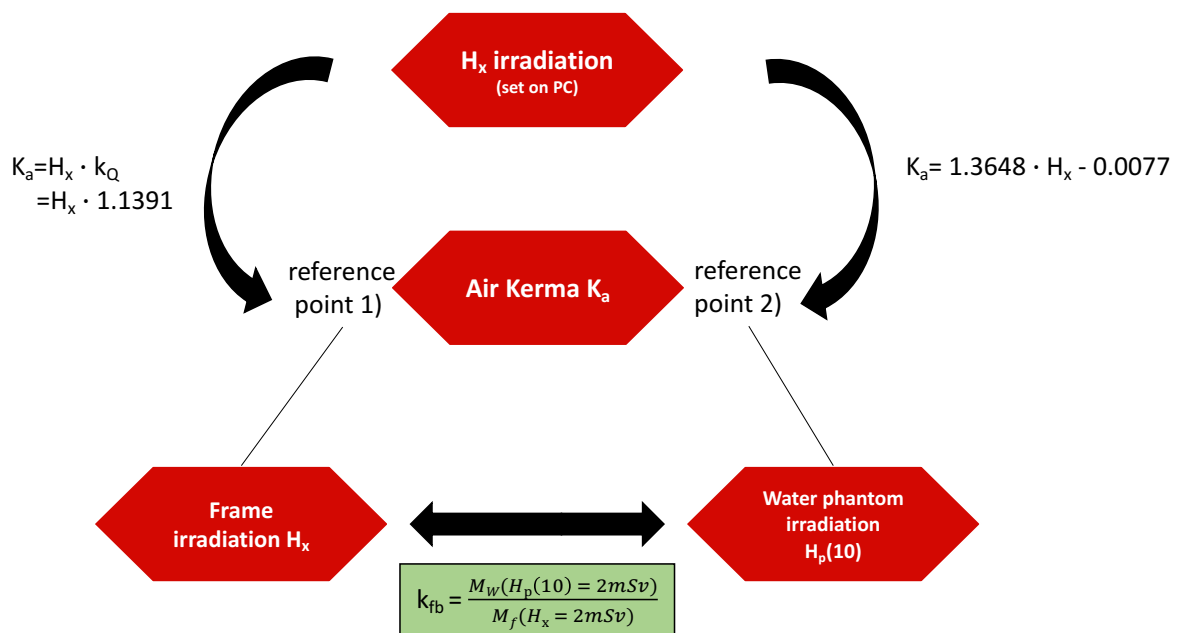


Figure 3.23: Illustration of the approach to calculate a conversion factor k_{fb} for frame to badge irradiations. k_Q cited from [58] and the linear function for K_a is determined in a paragraph below. The index at the measured value M specifies the measurement at the water phantom W or in the frame f.

At the ^{137}Cs facility only the radiation quantity H_x can be set in mSv. Frame irradiation are usually performed in H_x and irradiation on a phantom are performed in $H_p(10)$. Therefore, kerma has to be calculated for frame and phantom irradiations to compare them.

The irradiation in a frame and the irradiation on a phantom is performed at different distances from the source (see Figure 3.24) because the phantom is mounted on a table in front of the standard irradiation point (point 1 in Figure 3.24) for reasons of space, resulting in different reference point. At these two reference points the air kerma K_a is not the same for one H_x adjusted. While the conversion from H_x to air Kerma K_a for frame irradiations at reference point 1) is given by the factor $k_Q = 1.1391$ in the calibration certificate [58] (see Figure 3.23), the H_x -to- K_a -conversion for water phantom irradiations is determined by measurements at reference point 2) and discussed in the next paragraph. It is necessary to know the dose at the reference point, where the dosimeters are located during irradiation, to determine the frame factor.

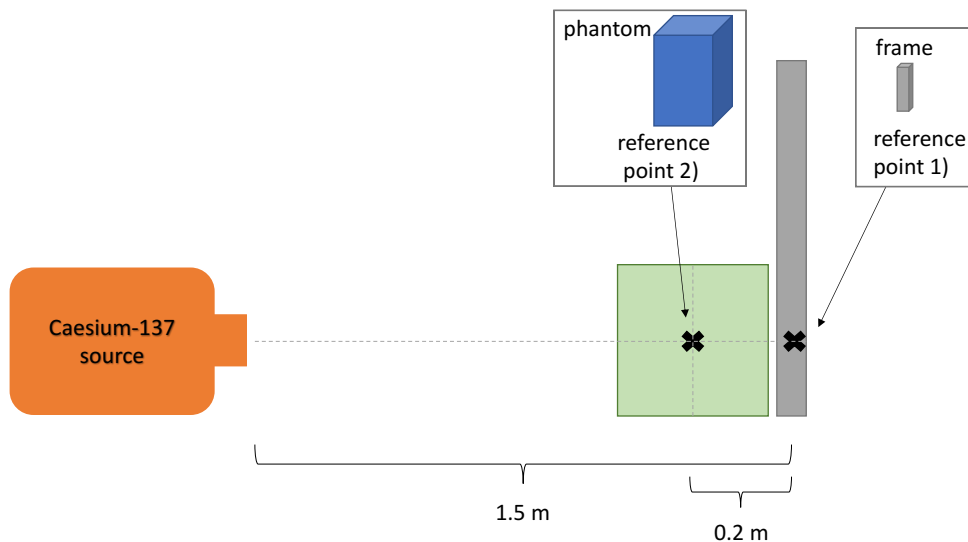


Figure 3.24: Schematic of the ^{137}Cs facility. The reference points for frame irradiations and phantom irradiations are marked. The desk for the phantom is illustrated in green and the gray areas represent fix components of a transport system.

Kerma determination

To measure air kerma at reference point 2) an ionization chamber and an UNIDOS device (secondary standard and reference dosimeters) are used. The ionization chamber, which is surrounded by a plexiglass case to create secondary electron equilibrium, collects charges generated by ionizing radiation. The UNIDOS device uses correction factors to calculate the air kerma for a point. In addition to the current temperature, the air

pressure is taken into account to calculate one correction factor . Certain H_x doses (dose quantity that can be set at the facility) are set and the kerma is measured at point 2) in Figure 3.24. Each dose is measured five times and a linear relationship $K_a = m \cdot H_x - b$ is observed. Thus, the data are described by

$$m = (1.3648 \pm 0.0004) \text{ mGy/mSv},$$

$$b = (0.0077 \pm 0.0008) \text{ mGy},$$

see Figure 3.25. Starting from kerma, the dose can be converted into all other dose quantities using conversion factors.

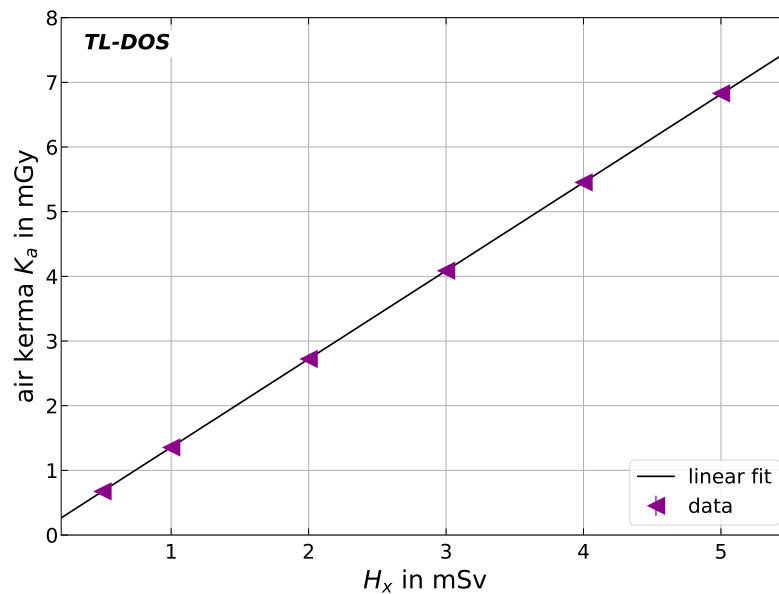


Figure 3.25: Linear relationship between dose quantities H_x (given at the irradiation facility) and air kerma measured with an ionization chamber at reference point 2). Data are plotted as mean values with their standard errors. A linear function is fitted to the data.

To determine the factor k_{fb} , two irradiations are performed. First, irradiations with $H_x = 2 \text{ mSv}$ and 24 detectors in a frame are carried out and evaluated. Secondly, irradiations in the neutron badge (Chapter 3.4) are performed with the same detectors but irradiated with $H_p(10) = 2 \text{ mSv}$ at the water phantom. If the two measured integrals of one detector are divided by each other (see Figure 3.23), different factors result for all four positions

in a neutron badge:

$$k_{fb,F6} = 1.03 \pm 0.03,$$

$$k_{fb,A6} = 0.92 \pm 0.01,$$

$$k_{fb,F7} = 1.07 \pm 0.02,$$

$$k_{fb,A7} = 0.92 \pm 0.01.$$

For the measurements in this thesis, all calibration measurements are carried out in a frame, multiplied by the factor k_{fb} , so that an $H_p(10)$ irradiation is simulated on the phantom. This is comfortable and time-saving.

The following calibration equation results for the four detectors in a dosimeter badge with the measured signal M :

$$H_{p,i}(10) = \frac{(M_i \cdot k_{\text{PM decrease}}) + b'_i}{m'_i}, \quad (3.4)$$

$$\text{with } i = [F6, A6, F7, A7].$$

3.6 Analysis software

For the TL-DOS system there are two analysis programs to evaluate glow curves measured in dependence of the time. One is the program TL-view used by the MPA NRW and the other is the software GCana.py [34], which was developed at the TU Dortmund University. Both are initially designed for photon irradiations measured at 573 K and representing peaks 1–5. In this chapter both programs are briefly introduced. While TL-view can be directly used to evaluate the data of the TL-DOS neutron dosimeter, GCana.py has to be adjusted for the analysis of neutron induced glow curves.

3.6.1 TL-view

The program TL-view presents the data recorded as function of time using the total photon count within a defined region of interest (RoI). The software defines the RoI in which the glow curve is visible and determines integrals belonging to the glow curve, i.e. the photon count sum (see Chapter 3.3).

In the RoI range the background is determined and subtracted from the glow curve. Different integrals, for example the gross integral or the net integral, can be selected and exported.

The measured glow curves can be displayed quickly, which is practical to get a first overview of a measurement. The main disadvantage is that only a total glow curve can be viewed integrally, i.e. glow peaks are not considered individually.

3.6.2 Analysis software: GCana.py

Another software is GCana.py. It is a glow curve deconvolution tool presented in [34]. A glow curve is deconvoluted into its individual glow peaks by applying theoretical models in order to examine them more closely. These models describe glow curves in a temperature-dependent way, requiring the time-dependent curves being transformed into the temperature regime before being analyzed. The transformation procedure is explained in the next section.

This analysis strategy has been developed for data measured at 573 K after photon irradiation, but neutron induced glow curves are measured at 653 K and additional peaks are visible. Therefore, different steps of the analysis have to be adapted, described in the following section.

3.6.3 Deconvolution with seven glow peaks

As first step, the RoI has to be adjusted. A RoI is determined by highly smoothing a glow curve with a Savitzky-Golay filter (Ref. [54]), combining single glow peaks into one broad peak. Starting from the maximum of the peak the borders of the RoI are estimated by searching for a given threshold on the TL intensity [37]. The number of iterations is set one higher as the old setting ($n = 2$) to find the glow curve also correctly for neutron induced curves. Figure 3.26 shows a glow curve on the left with the old settings and on the right with the new ones ($n = 3$), where the RoI is better estimated because significantly less glow curve signal is cut off by the red dotted lines.

The reader does not measure the detector temperature during a readout process due to loss of sensitivity caused by space limitations. Instead, the temperature is reconstructed with an exponential function, as the detector is pushed onto the hot plate and heats up exponentially. For temperature reconstruction, a superposition of multiple Gaussian functions are fitted into the time-dependent glow curve (regarded as prefit). Using the fit, the positions of the maxima of the peaks on the time axis are determined.

A second optimization process for readout of neutron detectors is the modification of the parameters for this prefit. Before a modification, the peak positions are not found optimally (reduced $\chi^2 > 30$). This is because the curves measured at higher temperatures are compressed in time regime. To find the peak positions more reliably, the start parameters for the Gaussian fits are adjusted resulting in a reduced χ^2 smaller than ten which is a

normal result for photon glow curves. Resulting Gaussian functions are shown in Figure 3.27 on the left. Usually only peaks 3–5 are fitted, because for these glow peaks the

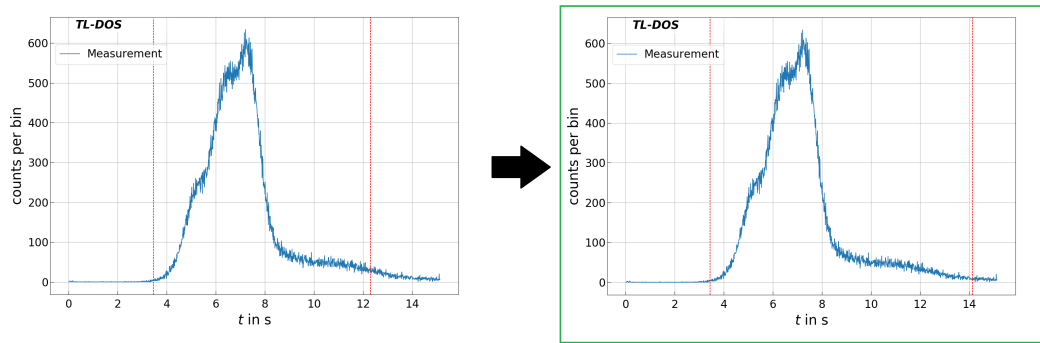


Figure 3.26: Adaptation of the RoI determination to High-LET induced glow curves. Left: A glow curve measured at 653 K and pre-heated after alpha irradiation with ^{241}Am before modification. In red the RoI limits are marked. Right: The same glow curve after modification with better RoI limits marked in red.

corresponding peak temperature is known from previous measurements (see Ref. [59]). For the high-LET peaks the peak temperatures are not known for the TL-DOS system. Consequently, they are not used for temperature reconstruction.

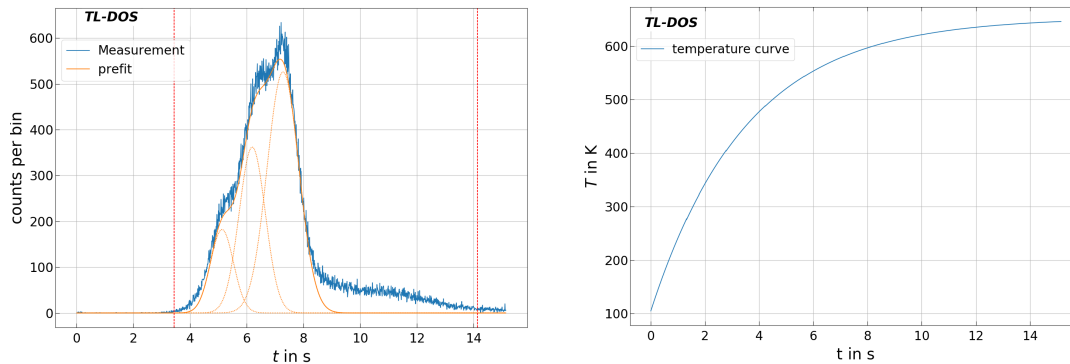


Figure 3.27: Left: A glow curve with three Gaussian functions to determine the peak maxima is shown. The RoI is marked as red dotted lines. Right: Exponential temperature profile of a detector measured at 653 K.

Each time value of the peaks is assigned a temperature, i.e. totally three data points are created. Using these data (t, T) , the exponential fit for the calculated T -curve is performed, so that the whole glow curve is transformed with this temperature curve [34]. This temperature reconstruction has to be adjusted regarding the maximal temperature, because the glow curves are recorded at 653 K and instead of 573 K.

On the right side in Figure 3.27 the T -profile for a measurement at 653 K is displayed.

Then, the reconstructed temperature curve is used to transform the glow curve from the time regime to the temperature regime, see Figure 3.28.

The glow curve is fitted with its individual peaks and a background function using an approximation from Wilkinsen proposed by Kitis et al. [60]. Here, two more peaks, peak 6 and 7, are added to the already existing peaks 2–5. In addition, the start parameters of the glow curve fit have been adjusted. Figure 3.28 shows a glow curve fitted after the modifications. Hence, the reduced χ^2 of the fit is reduced to maximal ten.

Since no temperature measurements of peaks 6 + 7 are available for the TL-DOS system, literature values are assumed for the start parameters of these both [61]. However, these temperatures are not verified for the TL-DOS system, so that the two peaks cannot be separated with the necessary precision. Furthermore peak 6 is usually strongly overlapping with peak 7 [36], whereby separation is difficult. Therefore, peaks 6+7 are considered together in the following investigations for safety reasons. These are considered together because they are highly overlapping and the fit temperature for the temperature reconstruction are not known either. So, it is not assured that the glow curve fit can separate the two satisfactory.

The output of the glow curve fit is a set of different peak parameters including individual integrals of the peaks.

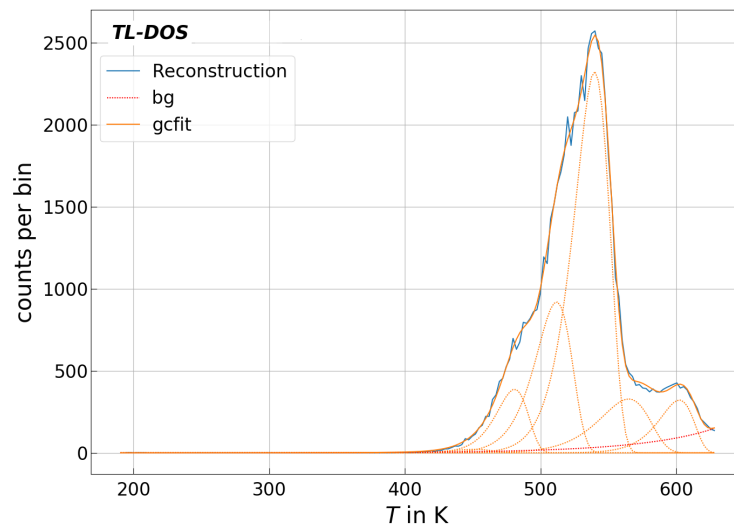


Figure 3.28: While in blue a glow curve transformed in the temperature regime is displayed, the fitted curve is shown in yellow with glow peaks 2 through 7 in the common nomenclature [35]. The background function (bg) is shown as red dotted line.

Due to fitting a glow curve and deconvoluting it into its individual peaks, the TL-DOS neutron dosimeter offers new possibilities and chances to get more information from a measurement. This will be further investigated in Chapter 6.

Chapter 4

Characterization of the TL-DOS dosimeter in neutron fields

In this chapter different neutron fields are described and the new neutron TL-DOS dosimeter is characterized and tested dosimetrically in these neutron fields. The response of the detectors in an albedo badge is analyzed after neutron irradiations.

The new dosimeter is characterized in well-known neutron fields in order to calibrate the system and compare it with other personal neutron dosimeter systems. In addition, the measurements are evaluated with different methods which are compared to specify a final guideline for the analysis.

After the measurements in the reference fields are well understood, further measurements are performed in workplace fields. These 'real' neutron fields are investigated using the field calibrations technique described in Section 4.4.

4.1 Neutron reference field facilities at the PTB

The International Organization for Standardization (ISO) recommends different types of radioactive neutron sources for routine calibration of neutron monitoring used for radiation protection purpose [62]. In Germany the Physikalisch-Technische Bundesanstalt (PTB) operates six neutron fields for dosimeter calibration. These fields are well known and therefore, they are called reference fields. The fields are generated by different neutron sources and their definitions are listed in Table 4.1. In order to ensure consistent fields with little scattered radiation, at the PTB all irradiations are performed in a low scattering room with a size of 7 m x 7 m x 6.5 m. The distance between the centre of the neutron source and the point of test during an irradiation is also given in Table 4.1. The angle α of incidence with respect to the detector normal is 0° for all direct irradiations. For irradiations with a shadow object (in-scattered irradiation), the field is called isotropic. [63]

Since the setups and sources are well known, each field can be characterized by measurements and Monte Carlo calculations [63]. The PTB calculates the irradiated dose $H_{p,n}(10)$ from the fluence of direct and in-scattered neutrons with the fluence-to-personal-dose-equivalent conversion coefficients $h_{p\Phi,dir}(10;\alpha)$ and $h_{p\Phi,ins}(10;isotropic)$, see equation (2.10).

Table 4.1: Setup parameters of the well-defined reference fields of radionuclide sources at the PTB and the thermal neutron calibration facility in terms of the calibration of neutron personal dose equivalent $H_{p,n}(10)$. The numbers assigned to the fields according to DIN 6802-4 are called c-points in this thesis. The distance is defined between the source and the irradiation point. [30, 63]

neutron field	c-point	\bar{E} in MeV	N category	distance in cm
thermal neutrons	-	$<2.5 \cdot 10^{-8}$	-	30
^{252}Cf ($\text{D}_2\text{O};\text{Cd}$) + shadow object	1	0.099	1	170
^{252}Cf ($\text{D}_2\text{O};\text{Cd}$)	2	0.565	1	58
^{252}Cf (bare) + shadow object	3	0.410	2	170
^{252}Cf (bare)	4	2.13	3	58
$^{241}\text{AmBe}$	5	4.15	4	58

As already described in Chapter 2, the strong energy dependence for neutron dosimeters is well known and was measured during the study in the 1980s (Chapter 2.7). Based on the field calibration measurements these neutron reference fields have been defined, which well represent the N-categories (explained in Chapter (2.7)) of the KFK report and cover the whole necessary energy range.

It is necessary to perform irradiations with neutron fields, where the energy spectra are known, in order to be able to deduce the correct dose for other unknown irradiations.

Today, the reference fields are usually used to calibrate an albedo dosimeter system because they still represent the four N categories of an albedo system. The energy-dependence of the dosimeter is clarified by defining the N categories for different neutron energy ranges.

Additionally, the fields serve for testing neutron dosimeters, for example in intercomparison tests like the one of EURADOS organization [21].

4.1.1 Energy spectra of the reference fields

Different neutron energy spectra with k - Z combinations (Figure 2.8) which are observed in workplaces are simulated by the reference fields with broad energy spectra. The energy

spectra of the reference fields are not designed to simulate spectra as realistic energy spectra of workplace fields as possible (compare Figure 2.1), but to represent the (k, Z) data obtained in the KFK report as well as possible. The spectra of the reference fields range from thermal neutrons to an $^{241}\text{AmBe}$ field with an average energy of 4.15 MeV. Thermal neutrons are free neutrons with a kinetic energy less than 100 meV, which are created by scattering neutrons with higher kinetic energies elastically at atomic nuclei several times. At the thermal neutron calibration facility of the PTB, sixteen $^{241}\text{AmBe}$ neutron sources are placed in a high-purity graphite block to moderate the fast neutrons [64]. The $^{241}\text{AmBe}$ sources emit neutrons with energies predominantly in the range above 1 MeV.

The energy spectra of the $^{241}\text{AmBe}$ and the different ^{252}Cf fields, c-points one to five, are illustrated in Figure 4.1. The fields have very different energy distributions, but they all range from thermal to epithermal to fast neutrons. However, the characteristics and shaping of the individual energy regions are very different to simulate a lot of real neutron workplace fields. For example the energy of a moderated ^{252}Cf field ranging from an energy at about 0.5 eV to several MeV. It is used for the calibration of personal dosimeters of the albedo type because its k factor is similar to that found inside a typical nuclear power reactor.[63]

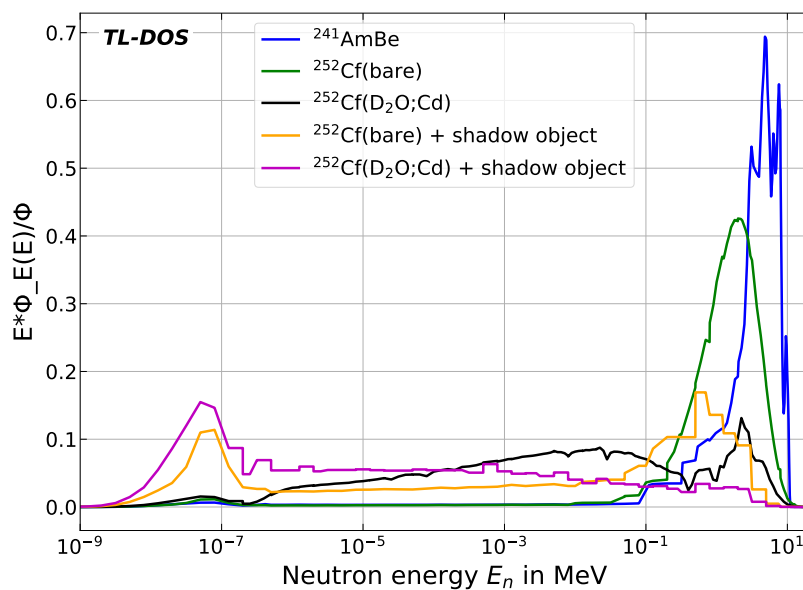


Figure 4.1: Fluence rate spectra for various calibration sources of the PTB. E is the neutron energy, $\Phi_E(E) = d\Phi/dE$ is the spectral fluence rate and Φ is the total fluence rate at the point of test. Energy spectra are displayed in different colors for the direct and the in-scattered part from the ^{252}Cf , $^{241}\text{AmBe}(\alpha, n)$, and $^{252}\text{Cf}(\text{D}_2\text{O}, 1\text{mm Cd})$ sources at 58 cm distance and for the in-scattered $^{252}\text{Cf}(\text{bare})$ and $^{252}\text{Cf}(\text{D}_2\text{O}, 1\text{mm Cd})$ fields with a shadow object at a distance of 170 cm [63].

4.1.2 Convolutions of the reference fields with LiF:Mg,Ti cross sections

On a TL-DOS detector the largest signal is induced for neutrons in the thermal energy range, and also the neutron-gamma separation works best in this energy range, as shown in Figure 3.4.

All reference fields contain a large fraction of higher energy neutrons as well. For the measurement of the albedo dose it does not matter since back-scattered neutrons are already moderated and therefore in a lower energy range. The induced signal on a field detector is considered below.

The product of the fluence of a neutron field and the neutron cross section of LiF:Mg,Ti is a measure for the signal induced on the detector. Both cross section of the detector materials Li-6 and Li-7 are convoluted with the reference fields. The results are presented for convolution with Li-6 as line and for convolution with Li-7 as dashed line in the same color in Figure 4.2 for five neutron fields.

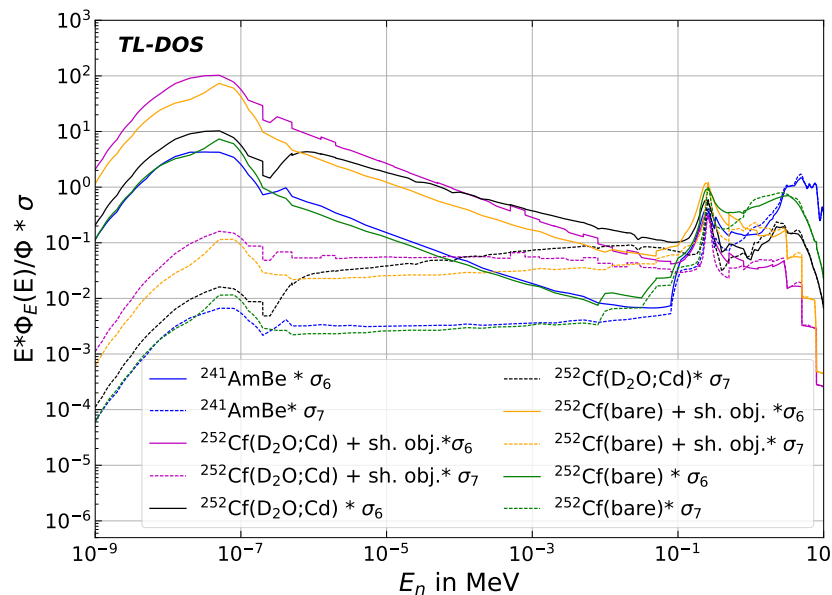


Figure 4.2: Convolution of the fluence of the reference fields with the neutron cross section of Li-6 and Li-7 ($E * \Phi_E(E)/\Phi \cdot \sigma$) as a function of the neutron energy. One field is marked in the same color and the materials (Li-6/Li-7) are marked with different styles.

The thermal part of such neutron fields contributes the biggest share of the induced signal. In the high energy area the signal of both convolutions are similar for one field, so the same amount is induced on the detectors Li-6 and Li-7. The higher the integral of a curve in Figure 4.2, the more signal is induced on the detector. Since every field has a thermal neutron part, the detectors can be used for this application and the estimation

of the neutron dose works reasonably well by subtracting the signals of the different detector types to subtract the photon dose. Usually, real workplace fields have an even higher proportion of thermal neutrons than artificial reference fields, because the neutrons scatter and moderate more on walls or structures.

4.2 TL-DOS dosimeter calibration for neutrons

TL-DOS neutron dosimeters are irradiated in the reference fields of the PTB to perform first tests in well known fields with the new TL-DOS system and to define the N categories subsequently. An ISO recommended water phantom (see Chapter 2.3) is used for all irradiations. In terms of personal dose equivalent $H_{p,n}(10)$, four dosimeters are fixed on the front plane of the phantom during an irradiation. Figure 4.3 shows the setup which is used for the $^{252}\text{Cf}(\text{D}_2\text{O};\text{Cd})$ irradiation behind a shadow object (field two in Table 4.1) in the low scattering room.



Figure 4.3: Irradiation setup for four albedo dosimeters at an ISO standard water phantom in the isotropic $^{252}\text{Cf}(\text{D}_2\text{O},\text{Cd})$ + shadow object reference field at the PTB. All irradiations are performed in the low scattering room. Left: Source, middle: shadow object, right: phantom with detectors. [64]

The TL-DOS neutron dosimeters are irradiated with $H_{p,n}(10) = 3\text{ mSv}$ in all fields, only the thermal irradiation is performed with $H_{p,n}(10) = 0.5\text{ mSv}$ because the irradiation time of this field is significantly longer than for the other fields. In each field a total of four badges is irradiated.

After the irradiated detectors are pre-tempered and measured at 653 K in the TL-DOS reader as described in Chapter 3.3, all detectors are calibrated to the signal of a ^{137}Cs irradiation to minimize single detector effects as explained in Chapter 3.5.

The dosimeters with four detectors each are evaluated according to DIN 6802-4. For this the ratio Z and the correction factor k are determined for each badge according to equations (2.16) and (2.13). These two factors are presented in Figure 4.4 for each of

the six fields in a scatter plot k - Z -plane. Additionally, the Z and k uncertainty of the measurements are shown. The uncertainty on k is due to the dominated uncertainty of the neutron irradiation. For each irradiation in the reference fields an $H_{p,n}(10)$ dose and its uncertainty are given by the PTB. These values are used for uncertainty propagation. The uncertainty on Z is calculated from the TL-DOS system uncertainties and the calibration method of the detectors. The uncertainties of an individual measurement are very small compared to the scattering for all measurements in one field and are therefore neglected in further analyses.

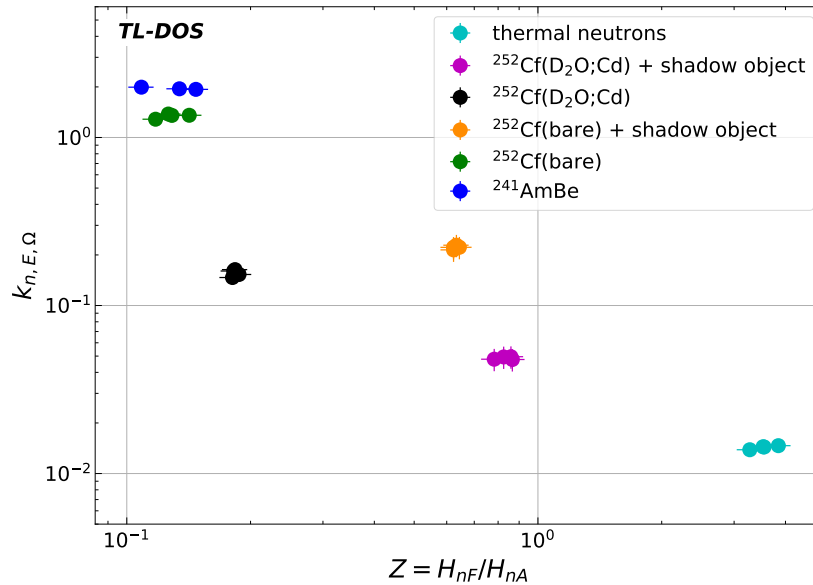


Figure 4.4: Calculated ratio Z and correction factor k for all six neutron fields; irradiated with $H_{p,n}(10)=3\text{ mSv}$ and 0.5 mSv , respectively. Four dosimeters are irradiated in each field and the uncertainties are estimated with the uncertainties of irradiation and calibration.

The values for the correction factor k extend over a large interval, note the logarithmic y-scale in the figure above. The response of the TL-DOS dosimeter is strongly dependent on the neutron field or neutron energy, as expected (see Chapter 2.5), and has to be corrected for dose estimation.

For fields with a lot of fast neutrons, a high k factor and a low Z ratio are found. If the Z ratio is less than one, there is more signal on the albedo detector than on the field detector. These neutron fields have such high energies that they hardly induce any signal on the field detector. In this energy range, the cross section for Li-6 is very low or similar to Li-7 (see Figure 3.4). After back-scattering of the fast neutrons from the body or a phantom, they are moderated and induce as thermal neutrons significantly more signal on the albedo detector (see the thermal range of Li-6 cross section). The higher the thermal part of the total energy spectra, the higher is the Z ratio for this field.

For the dosemeter response there are different consequences depending on the k factor, if:

- $k < 1$: it is higher than for ^{137}Cs ,
- $k = 1$: it is the same as ^{137}Cs ,
- $k > 1$: less signal is measured than after a ^{137}Cs irradiation with an equal dose.

The smaller the k factor, the higher the sensitivity of the dosemeter and the easier is the detection of smaller doses. Therefore, small k factors are desirable which is the case in most fields for the TL-DOS system. Furthermore, a small range of the k factor implies a weaker energy dependence of the dosemeter.

It is noticeable that the values of the ratio Z scatter significantly stronger for the $^{241}\text{AmBe}$ field, blue dots in Figure 4.4, than for all other fields and all k factors. The signal induced on the field detector which is used to calculate H_{nF} varies strongly. Irradiations with larger neutron energies induce less signal on the field detector, so that it is more difficult to separate the glow curve from the background.

In routine practice the energy correction factor k is unknown and has to be calculated from the measurement of the Z ratio (see Chapter 2.7). Figure 4.4 shows that the k factor can assume values between approximately 0.02–2. A wrong assignment could result in a strong over or underestimation of the dose.

If all measured data and all fields could be described by only one function, this curve could be used to estimate the k factor for the corresponding field after irradiation. The four N categories as described in Section 2.7.2 would not have to be defined and no dosemeter could be classified in the wrong category.

In order to test if the data can be described by only one function, the measurements of the reference fields are evaluated with two different glow curve tools. On the one hand the program TL-view (Section 3.6.1) is used, which determines the counts after a background subtraction in the time regime. On the other hand, the evaluation of the measurements is repeated with the integrals which are output from the glow curve fit in the temperature regime. The tool GCana.py to fit glow curves is explained in Chapter 3.6.2.

The results for Z and k are shown in Figure 4.5 for both analysis to fit a linear function with $y = m \cdot x + b$ through the data each. Furthermore, for both data sets the Pearson's correlation coefficient P is calculated:

$$P_{\text{TL-view}} = -0.936,$$

$$P_{\text{GCana.py}} = -0.936.$$

Both analyses yield the same value of P . This means that both data sets can be described equally bad by one linear function. The deviation between the fit and the data is large

for both analyses. In principle both techniques can be used for analyses, since for both variants similar values for the k factor and the Z ratio are found. For all next analyses the evaluations are performed with the glow curve analyses tool GCana.py to get more parameters of a glow curve.

Whether the Z ratio is the best choice for determination of the k factor is discussed in Chapter 7.

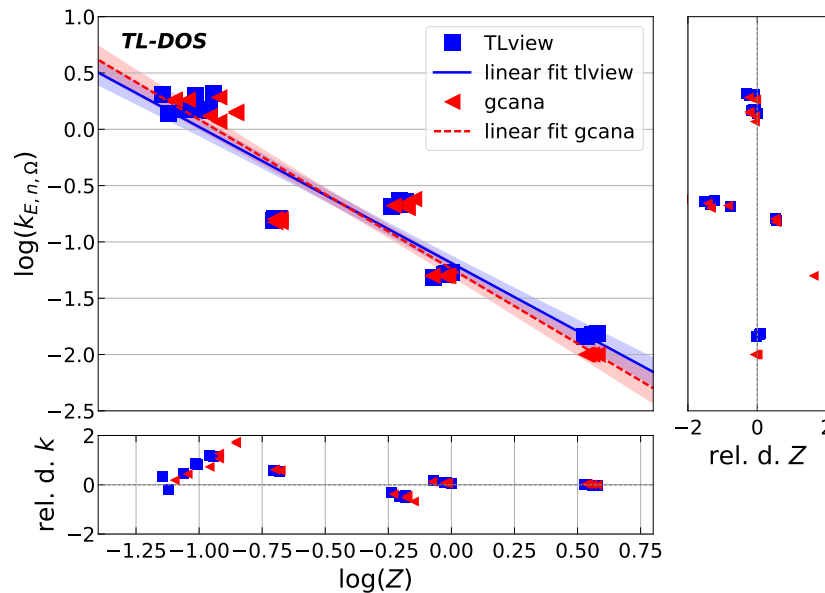


Figure 4.5: Logarithmic Z - and k factors of the reference fields with a linear fit, calculated by two glow curve analysis tools and measured with the TL-DOS neutron dosimeter. Relative difference of the Z and k data to the fit.

4.2.1 Analysis with and without the high-LET peaks of a glow curve

Neutron thermoluminescence systems previously used in personal dosimetry read out the detectors at a maximum temperature of 573 K. An advantage of the new TL-DOS system is the measurement at 653 K, so that the high-LET peaks are measured as well (see Chapter 3.3).

After glow curve deconvolution with peaks 3–7, the measurements of the reference fields are analyzed once from peak 3 up to peak 5 and once from peak 3 up to peak 7 in order to determine the influence of the high-LET peaks on the k factor. This approach is chosen to simulate commercial systems and the TL-DOS neutron standard. The entire glow curve is used for the evaluation with the high-LET peaks, the red points in Figure 4.6. The analysis of the glow curve up to peak 5 neglects peaks 6 and 7 for the determination of the total integral. The data for both methods are shown in Figure 4.6. For each field,

the four measurements of k and Z are averaged and the standard deviation is plotted as error bars to consider the scattering.

All k factors of the evaluation with the high-LET peaks (red points) are clearly below those without the high-LET peaks (blue hash), since more signal is measured. The measurement of additional signal results in a gain of the dosimeter sensitivity. The Z range is compressed because particularly the signal of H_{nF} increases in percentage terms. Especially for fields with higher energies - fields with a large k factor - the uncertainty on the k and Z factors is reduced by taking peak 6 and 7 into account. A strong reduction is observed for the Z ratios, as the fluctuations of the data of the $^{241}\text{AmBe}$ field are reduced without the high-LET peaks. (Field with the highest k factor in the figure.)

With the Figure 4.6 it is affirmed, if it is possible to measure the high-LET peaks, this should be used to reduce the uncertainties and to increase the sensitivity of the system as presented for the new TL-DOS neutron dosimeter.

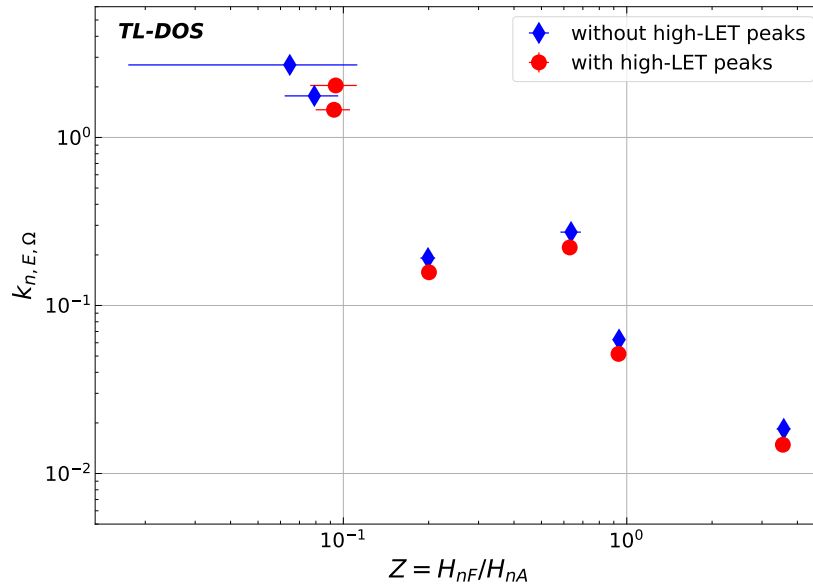


Figure 4.6: Correction factor k and ratio Z measured with the TL-DOS neutron dosimeter in the reference fields of the PTB. Four badges irradiated with $H_p(10) = 3 \text{ mSv}$ and in one field with 0.5 mSv . The measurements are analyzed with and without the high-LET peaks.

4.2.2 Individual- or Batch-Calibration of the dosimeter

While the calibration of the new TL-DOS neutron dosimeters is already described in Chapter 3.5, in this chapter two more precise methods which can be used for detector calibration are compared.

One method is the individual-calibration or so-called one-point-calibration. Each detector is irradiated once with a defined dose in ^{137}Cs , so that an individual calibration factor can be determined for each detector via one measurement point. The individual effects of a detector are reduced for the measurement and can be neglected because each is calibrated on its own sensitivity. However, it is a disadvantage if a mistake happens exactly during the only one calibration measurement and pass unnoticed. Additionally, this method has a large statistic uncertainty.

A further method is the so-called batch-calibration, which considers not each detector individually but a whole detector production batch together. For this purpose, some detectors of a batch are used to record signals of different photon doses between 0.5 mSv and 10 mSv. A linear fit with uncertainty analysis defines the relationship between the measurement signal and the dose. Therefore, the measurements and fit function presented in Chapter 3 are used. Not every detector has to be measured individually and therefore this method is less time-consuming. Furthermore, an outlier measurement is immediately noticeable because there are a few measurements for every dose. In addition, the calibration is not only done with one dose, but with a dose range. This obtains a better result for the later used personal dose range. However, this method can only be applied if the detectors are produced very uniformly and are comparable to each other in one batch.

The data of the reference neutron field measurements have been evaluated with both methods and for both the k factor and Z -ratio are calculated. Figure 4.7 illustrates the results of both calibrations. The differences of the k factor and the Z values for the two methods are also exemplified.

For one field very similar results are found, whereas all other k factors are shifted up to 50% on the y-axis. In principle, both data points, blue and red once, have the same trend and a similar standard deviation. The difference between the numerical values are also very small for every field.

The detectors of the neutron TL-DOS dosimeter will be evaluated by the batch calibration in future. It is possible because the detectors are all manufactured very uniformly and offers the advantages mentioned above.

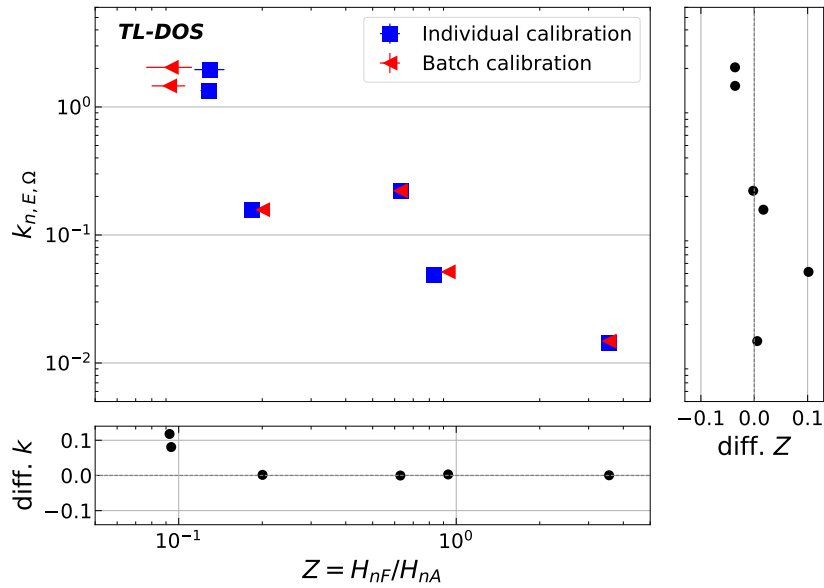


Figure 4.7: Average correction factor k and average ratio Z with their standard deviation measured with the TL-DOS neutron dosimeter in the reference fields of the PTB, irradiated with $H_p(10) = 3 \text{ mSv}$ and 0.5 mSv . The detectors are calibrated with the individual and the batch method. Absolute difference between k and Z values for all six fields.

4.2.3 Adjustment of the TL-DOS dosimeter application categories

After definition of the data evaluation by using the high-LET peaks and a batch calibration, the four application categories can be determined to divide the energy dependence of the new dosimeter.

An albedo neutron dosimeter is calibrated for neutron measurements by the four functions of the different N categories. Depending on the field of application of the dosimeter, the correction factor k can be determined with the appropriate function.

The measured values of the reference fields and the four N functions are shown in Figure 4.8 (left) for the TL-DOS neutron system. The functions explained in Section 2.7.2 have been adapted so that they are described by the data as well as possible. According to DIN 6802 the adjustment of the functions is performed with the factor ν (see equations in Table 2.1) [65]. Normally, the same ν -factor is used for all four functions, but this is not possible for the data of the TL-DOS albedo dosimeter. For the TL-DOS system the functions are fitted to the data of the reference fields with factor ν as free parameter of the N categories N1 to N4. As best result the following parameters are found to describe

the TL-DOS neutron system measurements:

$$\begin{aligned}\nu_1 &= 0.28 \pm 2\%, \\ \nu_2 &= 0.18 \pm 2\%, \\ \nu_3 &= 0.18 \pm 2\%, \\ \nu_4 &= 0.18 \pm 1\%.\end{aligned}$$

This adjustment is not sufficient because the data are also shifted in the Z direction and

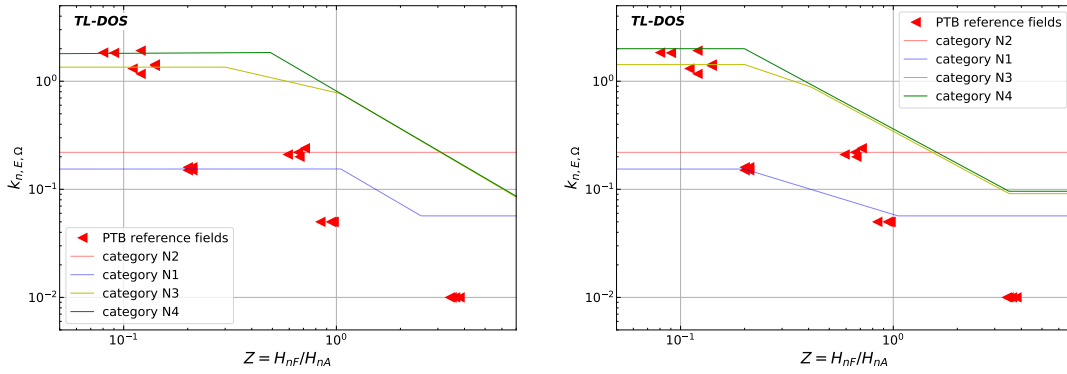


Figure 4.8: Data of the reference field irradiations and functions of the four N categories for the TL-DOS dosemeter. Left: Adjustment of the functions only by the ν -factor, according to the DIN. Right: Adjustment of all parameters of the functions to get the best result.

not only on the k axis. Not only the total dosemeter sensitivity is increased, but also the difference between the field and the albedo dose changes. In addition to the ν -factors, the exponents of the functions and the intervals for Z have to be adjusted. For example, the parameters could be modified to:

$$\begin{aligned}\nu_1 = 0.28 : & & 0.2 < Z < 1.05 : k &= 10^{-0.68} \cdot Z^{-0.6} \cdot \nu_1 \\ \nu_2 = 0.18 : & & & k = 0.18 \\ \nu_3 = 0.18 : & & 0.2 < Z < 0.41 : k &= 10^{0.41} \cdot Z^{-0.667} \cdot \nu_3 \\ & & 0.41 < Z < 3.5 : k &= 10^{0.258} \cdot Z^{-1.061} \cdot \nu_3 \\ \nu_4 = 0.18 : & & 0.2 < Z < 3.5 : k &= 10^{0.258} \cdot Z^{-1.061} \cdot \nu_4\end{aligned}$$

However, there is no standard regulation for this step in the DIN.

The description of the reference fields with the step functions works only conditionally well. The applications for personal neutron doseimeters have changed since the development of the analysis principle in the 1980s. This situation requires that the N-categories

should be questioned and discussed in detail. This is done with measurements in workplace fields, which are described in Chapter 4.4.

4.3 Comparison to commercial TL albedo neutron systems

In this chapter, the new TL-DOS neutron dosimeter is compared to commercially available thermoluminescence albedo systems.

At the individual monitoring service MPA NRW the so-called MPA Albedo GD02 neutron system [6], which is distributed by the company Thermo Fisher Scientific, is used for official monitoring of persons exposed to radiation. The system consists of the same albedo badge as the TL-DOS dosimeter, but the detectors are square chips with 25 mg of sensitive thermoluminescence material. In addition, it does not use MT-N powder but TLD-100 from Thermo Fisher Scientific as LiF:Mg,Ti material. In summary, form, type and material amount of the detectors are different from the TL-DOS system (see Chapter 3.2).

A detector card is building from four TLD-100 chips are firmly welded into a carrier card, see Figure 4.9. In contrast to the TL-DOS Reader, the readout of the detector card is done with a gas heating reader (model: Harshaw 6600) at 563 K. Fading effect elimination is done by applying a fading correction factor to the measurement instead of the pre-heating procedure used for TL-DOS.

Figure 4.10 shows the $k - Z$ -plot for the MPA Albedo GD02 (blue dots) as well as for the TL-DOS neutron system (red triangles). Both systems are irradiated in the same neutron reference fields, albeit to different doses.

The relationship between the k factor and Z ratio is comparable for both systems, indicating that the TL-DOS albedo system works adequately well. The MPA Albedo GD02 system has a PTB type approval and is used in practice as the official neutron- $H_p(10)$ -dosimeter by the MPA NRW monitoring service.

All k factors for the respective fields are generally much smaller for the TL-DOS dosimeter than those for the comparison system. The TL-DOS albedo system effectively measures more signal, because on the one hand the high-LET peaks are considered and on the other hand the detectors are more sensitive to neutron radiation (see Section 4.3.1).

The Z ratios are also smaller for the TL-DOS system. The denominator H_{nA} of the

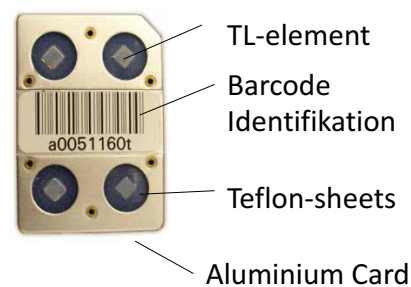


Figure 4.9: Harshaw TLD card with four detector chips of Thermo Fisher. Two Li-6 and two Li-7 detectors.

equation (2.16) becomes larger because especially for the measurement of thermal neutrons, which are usually dominant in back-scattered fields, more signal is induced on the detector.

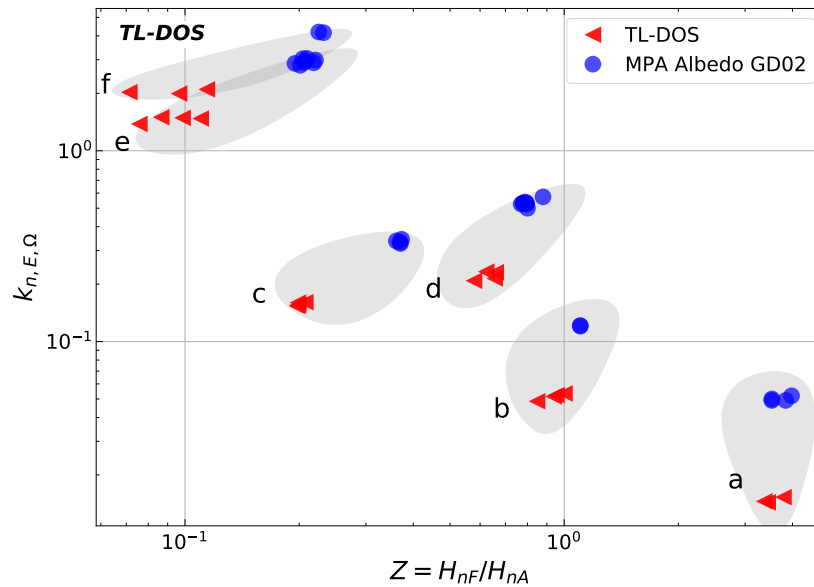


Figure 4.10: The calculated neutron field-specific calibration factors k and Z for the MPA Albedo GD02 and the TL-DOS system obtained from the measurement in reference fields of the PTB. a: Thermal, b: $^{252}\text{Cf}(\text{D}_2\text{O};\text{Cd})$ +shadow object, c: $^{252}\text{Cf}(\text{D}_2\text{O};\text{Cd})$, d: $^{252}\text{Cf}(\text{bare})$ +shadow object, e: $^{252}\text{Cf}(\text{bare})$, f: $^{241}\text{Am-Be}$.

The difference in k factors and Z ratios for TL-DOS and MPA Albedo GD02

The difference of the k factor and Z ratio between the two systems is calculated for each of the six reference fields and the numerical values are listed in Table 4.2. All Z ratios of the TL-DOS system are on average 0.17 ± 0.01 lower for all reference fields. For the k factor, consequently for the whole system, a sensitivity gain of approximately a factor of two is found for TL-DOS compared to the MPA GD02 (see Table 4.3), despite the fact that TL-DOS detectors consist of less than half the amount of thermoluminescence material compared to the Harshaw chips.

The dose detection limit of $100 \mu\text{Sv}$ will be thus reached significantly easier with the TL-DOS system. Even for fields with higher energies, the value for the k factor is close to one, which means that the detector response is strongly similarly to a ^{137}Cs irradiation, so even small doses can be measured in these fields with no problem.

Table 4.2: Absolute difference Δ of the Z ratios and k factors between the MPA GD02 system and the TL-DOS neutron system for all reference fields of the PTB neutron calibration facilities.

field factor	thermal	Cf(mod.)+s	Cf(mod.)	Cf+s	Cf	AmBe
ΔZ	0.17 $\pm 18\%$	0.16 $\pm 19\%$	0.17 $\pm 6\%$	0.17 $\pm 18\%$	0.20 $\pm 1\%$	0.14 $\pm 1\%$
Δk	0.04 $\pm 2\%$	0.07 $\pm 1\%$	0.18 $\pm 2\%$	0.31 $\pm 6\%$	1.48 $\pm 4\%$	2.18 $\pm 1\%$

Fluctuation of the k and Z factors

In addition to the system sensitivity, the fluctuation behavior of the Z values and especially of the k values is interesting as well. In Table 4.3, the fluctuation for the k factors and Z -ratios are averaged for all six fields. It is calculated from the relative standard deviation.

It is found that the fluctuation of k is in a similar range with $\sigma_k/k = 1\text{--}5\%$ for both systems and all fields. Concluding again, the TL-DOS system can be used as an alternative to the MPA GD02 because the spread of the second system is sufficient for approval. On average, the systems have the same fluctuation for the k factors and also for the Z values respectively. The TL-DOS data scatter is even more evenly, thereby uniform methods can be used for understanding the behavior of scattering.

Table 4.3: Relative standard deviations of the calibration factor k and ratio Z for two dosimeter systems and the six reference fields provided by the PTB.

Field	TL-DOS				MPA GD02			
	Z	σ_Z/Z	k	σ_k/k	Z	σ_Z/Z	k	σ_k/k
Thermal neutrons	3.55	6%	0.01	2%	3.72	5%	0.05	3%
$^{252}\text{Cf}(\text{D}_2\text{O};\text{Cd})+\text{shadow object}$	0.94	4%	0.05	2%	1.10	1%	0.12	1%
$^{252}\text{Cf}(\text{D}_2\text{O};\text{Cd})$	0.20	1%	0.15	2%	0.37	2%	0.33	2%
$^{252}\text{Cf}(\text{bare})+\text{shadow object}$	0.63	1%	0.22	2%	0.80	4%	0.53	4%
$^{252}\text{Cf}(\text{bare})$	0.10	7%	1.46	2%	0.21	4%	2.94	3%
$^{241}\text{Am-Be}$	0.09	7%	2.00	1%	0.23	2%	4.18	1%

4.3.1 Impact of the detector thickness

The TL-DOS system is compared to other available official neutron dosimeters to discuss the impact of the detector thickness on the k and Z factors. For this purpose, results of

the annual comparison (see Section 2.4) are collected from various individual monitoring services in Germany. The four individual monitoring services provide different systems, but for dose estimation each uses the same albedo principle. The various combination designs which are compared to the TL-DOS system are visualized in Table 4.4.

The difference between the MPA GD01 and the MPA GD02 is the albedo badge. The system GD01 uses an old badge design. Whereas the measurements of the Mirion Technologies (AWST) GmbH in Munich (AWST Munich) system are performed with the new badge; the same badge type like MPA GD02 and used for the TL-DOS system. The main modification to the old badge is an enlarged albedo window. The system provided by the AWST Munich use the same material for a detector as the MPA NRW system, but in a different thickness of the chips. These are distinctly thinner with 0.34 mm compared to 0.89 mm MPA detectors.

In addition to the MPA GD02 albedo and TL-DOS albedo, the k - Z values for the two further systems are shown in Figure 4.11. The TL-DOS system has the lowest k factors and thus the highest sensitivity of all the five systems presented in Table 4.4. For all systems a similar behavior is found.

The effects of the detector thickness and the badge on the factors are examined more in detail below.

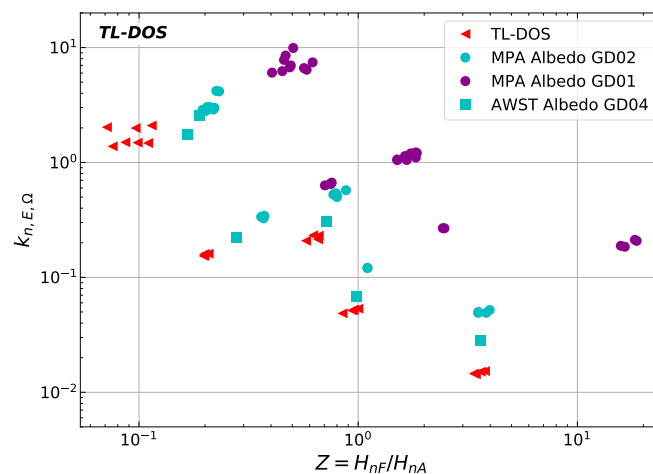

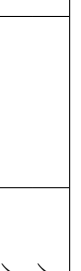

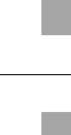
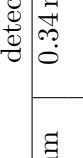


Figure 4.11: The correction factor k and the calculated ratio Z of different albedo systems including various detectors and neutron badges, irradiated in the six neutron reference fields of the PTB. Data provided from different monitoring services. Same marker style = same thickness.

Due to a higher readout temperature of the detectors and measurement of additional signal the sensitivity increases, but another influence on the sensitivity gain is the detector thickness.

Table 4.4: The designs of the albedo dosimeters used at the individual monitoring services in Dortmund and Munich. The components: badge, detector thickness and form, sensitiv material, readout device and readout temperature are considered. All presented neutron systems use different temper profiles, which are not discussed in detail here. It is important, if the detectors are read out at a temperature higher or lower than 573 K.

System name	badge		detector			material		meas.temp.	
	old	new	0.89 mm	0.34 mm	0.25 mm	TLD-600/TLD-700	MT-6/MT-7	<573 K	653 K
AWST-TL-GD04									
TL-DOS		✓		✓	✓			✓	
MPA GD02		✓	✓			✓		✓	
MPA GD01	✓		✓			✓		✓	✓

The results in Figure 4.12 imply a relationship between the k factor and the detector thickness for the three dosimeter systems, MPA GD02, AWST-TL-GD04 and TL-DOS. To neglect effects of the badge only the data measured with the new albedo badge have been considered. Exemplary, the data found in the $^{241}\text{AmBe}$ field and the Cf(mod.)+shadow object field are presented in Figure 4.12 to explain the effect for different neutron energies. The k factor increases with increasing thickness of the sensitive material and a linear function is drawn to guide the eye.

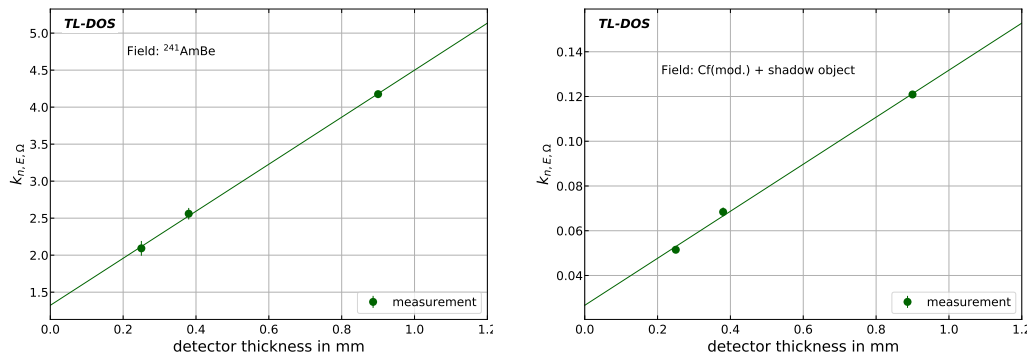


Figure 4.12: The correction factor k for three neutron dosimeter which have various detector thicknesses with a line to guide the eye. Presented for two fields with different energies. Left: AmBe field. Right: Cf mod. + shadow object field.

This effect is caused by the calibration measurement (irradiated in ^{137}Cs) to determine the neutron dose H_{nA} . To estimate the dose measured with a neutron dosimeter, the detector signal is calibrated to the signal of a photon irradiation. Due to the dose build-up effect, the same photon irradiation induces more signal in a thicker detector than in a thinner one. This signal is used to determine a calibration factor, which is correspondingly smaller for thicker detectors. The calibration factor is applied to the signal of the unknown neutron irradiation to calculate H_{nA} . In contrast to a photon irradiation, the influence of the detector thickness is negligible for neutron irradiations. Therefore, H_{nA} which is used in equation (2.13) for dose estimation results in a higher value and thus, resulting in a smaller k factor.

Since the sensitivity of the system should be as high as possible, the thickness is well optimized for the TL-DOS system.

4.3.2 Effects of the badge type

The increased sensitivity of a dosimeter system with the new badge GD02 compared to badge GD01 has already been shown in Ref. [3] and are confirmed by the data in Figure 4.11. If the GD02 data (marked in blue) are compared with each other, the phenomenon is corroborated.

For all described systems the differences of the k and Z factors between the highest value and the lowest value are calculated. It is the difference between the results of the measurements in the $^{241}\text{AmBe}$ field and in the thermal field. Furthermore, these both are the reference fields with the highest and lowest mean neutron energy.

$$\text{diff } Z = Z_{\text{thermal}} - Z_{\text{AmBe}}$$

$$\text{diff } k = k_{\text{AmBe}} - k_{\text{thermal}}$$

The calculated Z difference are listed in Table 4.5. The trend is found that diff Z gives information about the badge used. The Z difference of the new badge has been compressed compared to the old one. The difference of the old badge (GD01) is almost factor five higher.

Table 4.5: Difference between the highest and the lowest value for Z and k calculated for all four albedo systems with the new and the old dosimeter badge.

System	diff Z	diff k	badge type
TL-DOS	3.5 ± 0.2	2.1 ± 0.1	new
MPA GD02	3.5 ± 0.2	4.13 ± 0.08	new
AWST-TL-GD04	3.5 ± 0.1	2.53 ± 0.04	new
MPA GD01	16.8 ± 0.6	9.0 ± 0.5	old

In addition, it seems that the difference of the k factors is also dependent on the different detector types. Since, the smallest differences can be found for the TL-DOS system, it is optimized regarding to the energy dependence. This is an advantage to accomplish the second challenge of the strong energy dependence described in Chapter 2.5 as well as possible.

4.4 Neutron field calibrations in workplace fields

Additionally to characterizing the new TL-DOS neutron dosimeter in reference fields, the system is investigated in workplace fields. Workplace fields are neutron fields that occur at human workplaces, e.g. at nuclear power plants and accelerators. They are not adapted to the N categories like the reference fields, but the energy spectra of these fields are usually unknown (see Chapter 2.2). Therefore, so-called field calibrations are carried out using the neutron sphere technique explained in the next section. Using this technique, the local dose $H_n^*(10)$ is determined and thus, the k factor for this field can be calculated. This factor is used as the correction factor for dose estimation if a person wears a neutron dosimeter in the corresponding area.

Sections 4.4.1 and 4.4.2 describe how such a field calibration is performed. In the following

sections, four field calibrations are presented as examples for workplace fields with very different energy spectra to include a large region of the k - Z plot.

4.4.1 Layout and procedure of field calibrations

Field calibrations are performed according to DIN 6802-4:1998-04 using so-called neutron moderator spheres, see Figure 4.13 (left). These polyethylene (PE) moderator spheres are 30 cm in diameter and provide low energy and directional dependence in the middle of the sphere. The neutron field is assumed nearly isotropic at this point [66].

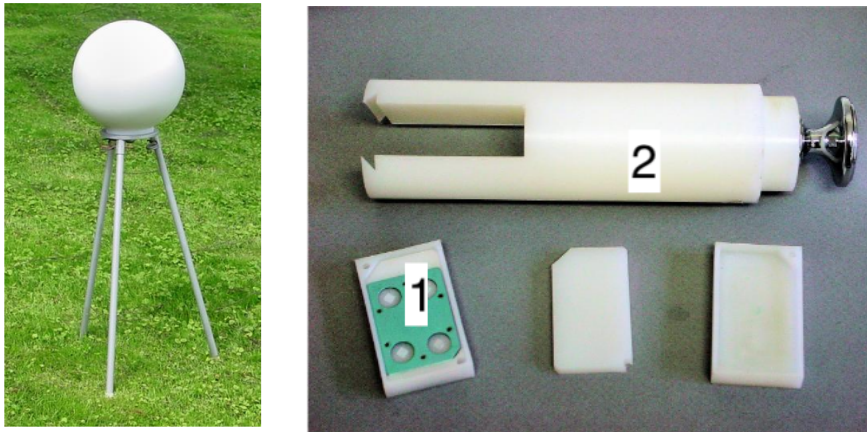


Figure 4.13: Left: Neutron moderator sphere on a 70 cm high tripod. Right: Sphere rod with its components to fix the detectors in the phantom: (1) detectors in a carrier card (2) sphere rod. Modified from Ref. [6].

A detector card (Figure 3.4) with neutron sensitive TL detectors is inserted into the card holder (1) of the sphere rod (2) and the latter one is placed into the center of the PE sphere. The albedo card in the sphere is used to estimate the ambient neutron dose $H_n^*(10)$ at the location of the measuring point and is used as reference value. The ambient neutron dose is calculated from these measurements according to:

$$H_n^*(10) = k_{n,E} \left[\frac{k_{n,\text{lin}}}{2 \cdot N_{\text{direct}}^*} [(M_1 - M_2) + (M_4 - M_3)] - \dot{H}_{\text{nat}} \cdot t \right]. \quad (4.1)$$

For this purpose, two neutron doses are calculated from the four measured dose values M_i of the detectors 1–4 (equation (2.15)), calibrated in ^{137}Cs with background subtraction (see Chapter 3.5). In addition, a correction factor for neutron radiation and energy dependency $k_{n,E}$, a correction factor $k_{n,\text{lin}}$ for non-linearity of the neutron signal displayed and the dose of natural background radiation \dot{H}_{nat} are taken into account. For the TL-DOS system the non-linearity is $k_{n,\text{lin}} \equiv 1$ and the dose rate of natural background is assumed to be $\dot{H}_{\text{nat}} = 2 \mu\text{Sv/d}$. The parameter N_{direct}^* is the corrected calibration factor

for direct neutron radiation and has to be determined for each system individually by irradiations in the reference fields of the PTB before using it. For the TL-DOS system the determination of N_{direct}^* is presented in Section 4.4.2.

In addition to the detectors in the sphere center, a set of four personal dosimeters are irradiated in diametrically opposed positions on the surface of the PE phantom. The four neutron badges are attached to the equator of the sphere as shown in Figure 4.14 and are used to record a calibrated signal. It is assumed that the occurring neutron energies are too small to penetrate the whole sphere [67].

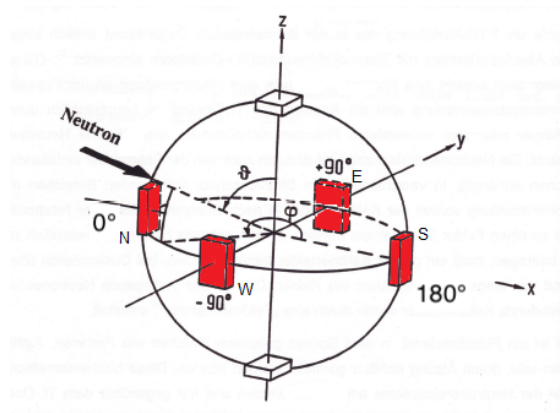


Figure 4.14: A sketch of a neutron moderator sphere with four positions to locate the albedo dosimeters on the sphere during an irradiation in a neutron field. Two opposite badges are a measurement pair (N+S and W+E).

The dosimeters are evaluated using the albedo method described in Chapter 3 and the ratio Z is determined. With a field calibration, the system ratio X is calculated twice (two dosimeter pairs: Nord+South and West+East) as well. Therefore, two opposite badges are always used respectively:

$$X = \frac{H_{\text{nF,(N/E)}} + H_{\text{nF,(S/W)}}}{H_{\text{nA,(N/E)}} + H_{\text{nA,(S/W)}}}. \quad (4.2)$$

In the last step, the k factor is determined for the field at the point of the sphere with the ambient dose measurement inside the sphere as basis:

$$k_{\text{n,E},\Omega} = \frac{H_{\text{n}}^*(10)}{H_{\text{nA,(N/E)}} + H_{\text{nA,(S/W)}}}. \quad (4.3)$$

Such measurements are performed in four workplace fields to characterize the TL-DOS neutron dosimeter in this neutron fields.

4.4.2 Determination of N_{direct}^* for TL-DOS

For calculating N_{direct}^* two further irradiations are performed in the reference fields. On the one hand a sphere with four TL-DOS detectors is irradiated in the $^{252}\text{Cf}(\text{bare})$ reference field with $H_{\text{tot},n}^*(10) = 5 \text{ mSv}$. The dose is divided in the neutron direct irradiation $H_{\text{DIR},n}^*(10) = 3.72 \text{ mSv}$ and the neutron in-scattered irradiation $H_{\text{INS},n}^*(10) = 1.27 \text{ mSv}$. On the other hand one sphere with four TL-DOS detectors is irradiated in the $^{252}\text{Cf}(\text{bare})$ Cf + shadow cone field with $H_{\text{SCH}}^*(10) = 2.5 \text{ mSv}$. [64]

The doses H_{ges} (DIR+INS) and H_{SCH} of the two irradiations are calculated by averaging the neutron doses of one detector card with

$$H_j = \frac{H_{n1} + H_{n2}}{2}. \quad (4.4)$$

The neutron doses H_n are estimated by subtract the measured value of a Li-6 detector and a Li-7 detector of each other. All values are entered into the formula:

$$N_{\text{direct}}^* = \frac{N_{\text{direkt}}}{N_\gamma} = \frac{1}{N_\gamma} \cdot \frac{H_{\text{DIR}}}{H_{\text{DIR},n}^*(10)} \quad (4.5)$$

$$= \frac{1}{N_\gamma \cdot H_{\text{DIR},n}^*(10)} \cdot \left(H_{\text{ges}} - \frac{H_{\text{SCH}} \cdot H_{\text{INS},n}^*(10)}{H_{\text{SCH},n}^*(10)} \right). \quad (4.6)$$

N_{direct} is the calibration factor for the neutron direct radiation and M_{DIR} is the measured dose of direct radiation in Sv. The correction factor for ^{137}Cs gamma radiation N_γ is one for the TL-DOS neutron system, resulting in a calibration factor

$$N_{\text{direct}}^* = 2.8 \pm 0.2.$$

4.4.3 Field calibrations at the ELBE positron source

Two field calibrations are performed at the Epos to test an application in the N1 category. Epos is operated for material investigations at the radiation source ELBE (electron linear accelerator for high brilliance and low emittance beams) of the Helmholtz-Zentrum Dresden-Rossendorf. The positrons have a kinetic energy E_{kin} from 0.5 keV up to 15 keV. The measurements are performed at different points in the accelerator where slightly different neutron energy spectra and doses are expected. The setup of the spheres with the albedo dosimeters are presented in Figure 4.15 (left). The right picture shows the location of the measurement point in the room that is not in the direct beam but in the scatter field. [68]

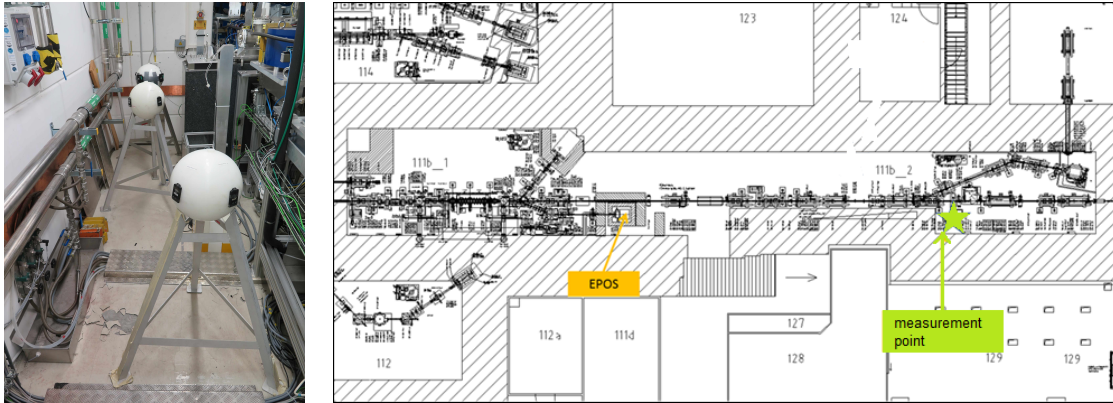


Figure 4.15: Left: Neutron moderator spheres with four TL-DOS albedo dosimeters for field calibrations at Epos. Right: The location of both spheres in the facility room. The measurement point is drawn as green star.

From earlier measurements it is known that many thermal neutrons occur at both measurement points. Therefore a classification into the N1 category is expected.

The field calibrations are evaluated according to Section 4.4.1 and the results for the ambient neutron dose are shown in Table 4.6.

Table 4.6: The calculated ambient neutron dose $H_n^*(10)$ measured at two different points at Epos. The doses are extracted from [68].

position	$H_n^*(10)$ in mSv
sphere 1	7.4 ± 0.6
sphere 2	8.2 ± 0.6

The Z and k factors are determined for both measurements with this calculated ambient doses and are shown in Figure 4.16 together with the results of the reference field measurements and two N categories. The following mean values are found for field calibrations at Epos:

$$\bar{k} = 0.09 \pm 0.01,$$

$$\bar{Z} = 1.11 \pm 0.02.$$

The k - Z -factor combination confirms the expected N1 category for the field. The results are similar to the data of the ^{252}Cf ($\text{D}_2\text{O};\text{Cd}$) + shadow object reference field. Therefore, it is claimed that irradiations and field calibrations of the TL-DOS neutron dosimeter in workplace fields work as expected.

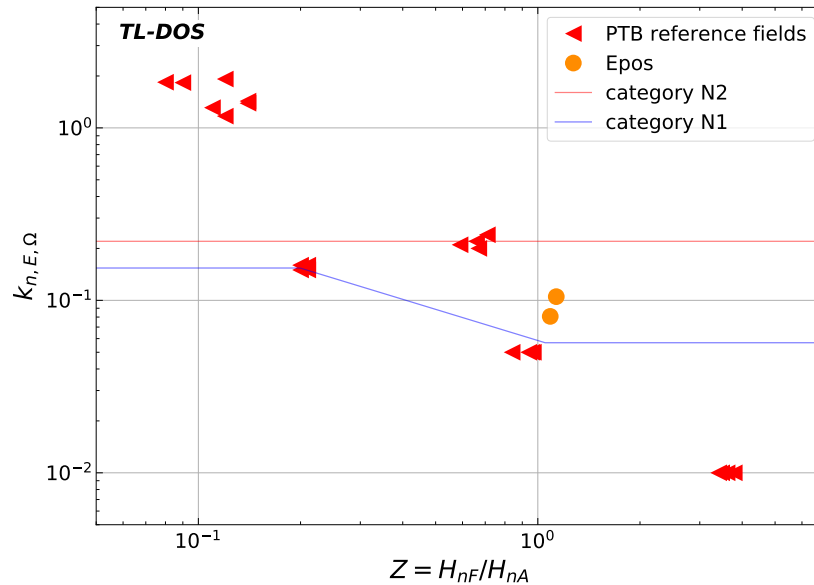


Figure 4.16: The correction factor k and the ratio Z measured with the TL-DOS neutron system. In red are marked the data of the reference fields, in orange the field calibration at EPOS and as lines the N1 and N2 categories. The field calibrations at EPOS are classified to the N1 category.

4.4.4 Field calibrations in a castors storage hall

Another application of albedo dosemeters is in castor storage halls. According to the DIN 6802-4:1998-04 usage in this areas is usually classified in the N2 category.

Two field calibrations are performed at the same time in a castor storage hall. Over a period of one week two moderator spheres each, equipped with four badges and one detector card inside, are positioned next to six castor containers at a distance of 1m. The exact positioning of the spheres K4 and K6 (logistical labels of the spheres) is sketched in Figure 4.17 as black stars next to the blue castor containers.

Different doses are expected for K4 and K6 because it is known that the six castors differ in their dose rates due to their age and content. The dose at position K4 should be larger than at the second position K6. This is also reflected in the control area around the castors, which is illustrated in Figure 4.17 as red line. In the east direction the control area is larger then in the west direction.

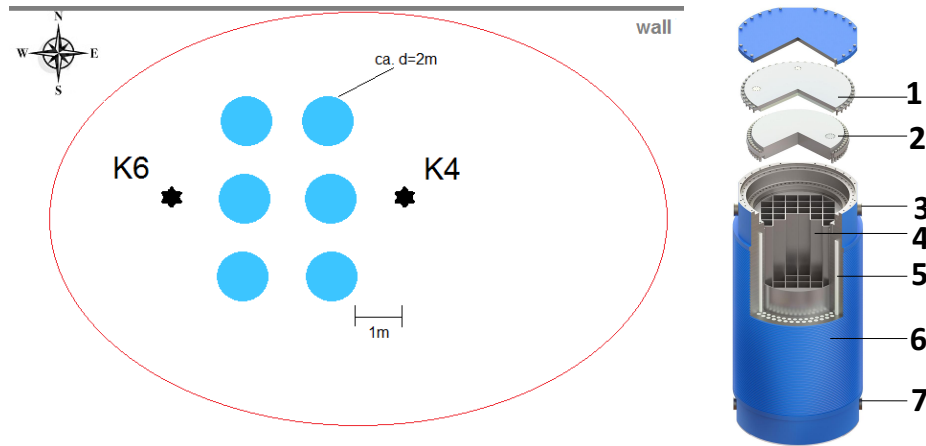


Figure 4.17: Left: Measurement setup for two field calibrations in a castor storage hall to measure the neutron and gamma dose $H_p(10)$. All castors are marked in blue and two measurement points are illustrated as black stars. Right: Structure of a loaded castor type container: 1) secondary cover with pressure switch and moderator plate 2) primary cover 3) lifting lugs 4) pack basket 5) moderator rod 6) container body with cooling fins 7) lifting lugs [69].

Using equation (4.1) the local dose $H^*(10)$ is calculated and yields after one week to:

$$K4 : H_n^*(10) = (1.78 \pm 0.15) \text{ mSv},$$

$$K6 : H_n^*(10) = (0.54 \pm 0.05) \text{ mSv}.$$

Subsequently, equations (2.16) and (4.3) are used to calculate the Z ratios and k factors to enter them in the k - Z -scatter plot. The results are shown in Figure 4.18 together with the EPOS field calibration and the measurements in the reference fields. The N1 and N2 functions are also shown for a better classification of the field calibration data in a N category.

The measurements with the TL-DOS neutron dosimeter show that a classification of these fields in category N2 according to DIN 6802-4:1998-04 is unconfirmed. As an alternative to a classification in category N2, a classification of the measurement in category N1 is proposed. In particular, Figure 4.18 shows that the results of the field calibrations are close to the N1 curve and category, so they can be assigned to the range N1. Some points are above and others below the function. Thus, the average of the points are on the N1 function. The measured (k, Z) values are exactly between the two reference fields that simulate the N1 category. If the TL-DOS neutron dosimeters are not evaluated with their measured k but with the N1 function, the average dose would deviate by 6.3 % from the measured dose. A dose overestimation is clearly better than a dose underestimation. In dosimetry the evaluation is made conservative in case of doubt. So the personal dose

is rather overestimated than underestimated. However, with N2, the dose would be overestimated strongly.

Category N1 is thus sufficient and is recommended for applications like explained above.

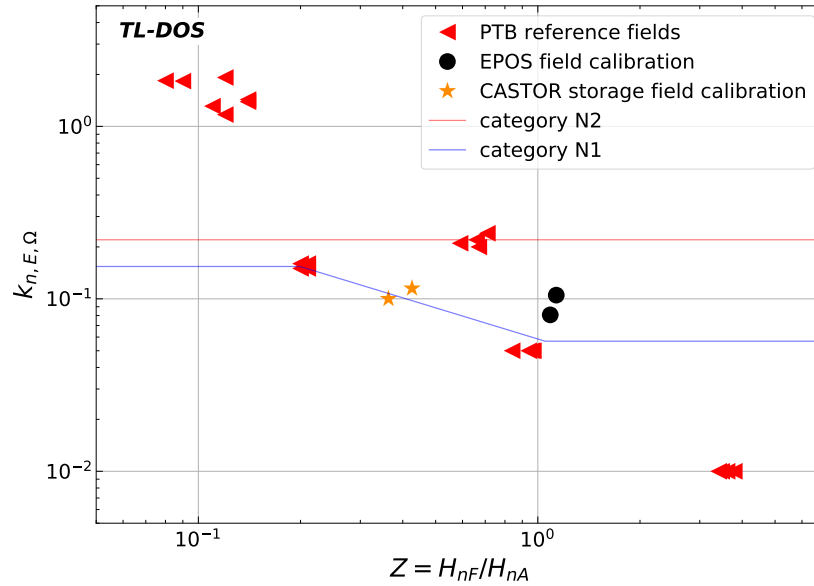


Figure 4.18: The correction factor k and ratio Z measured with the TL-DOS neutron system. As orange stars the field calibrations in a castor storage hall, in red the data of the reference fields, in black the field calibration at EPOS and as lines the N1 and N2 categories. All data are measured with the TL-DOS system with different $H_p(10)$ doses.

The same measurement was repeated using the Harshaw Albedo GD02 MPA system. The resulting doses obtained with the four dosimeters described above are given in absolute values for both systems in Table 4.7.

A good agreement of the systems is observed for the $H_n^*(10)$ dose. As expected, the k factors for the TL-DOS system are significantly smaller than the ones of the comparison system. The sensitivity gain of factor two discussed in Chapter 4.3 is also confirmed here.

Table 4.7: For two TL neutron personal dosimeters the calculated dose, the correction factor k and the ratio Z are listed for two position in a castor storage hall with six castors to compare the results of the TL-DOS dosimeter and the albedo MPA GD02 whose uncertainties are not given for this measurement.

system	position	$H_n^*(10)$ in mSv	k	Z
TLDOS	K4	1.78 ± 0.15	0.12	0.36
TLDOS	K6	0.54 ± 0.05	0.14	0.42
GD02	K4	1.67	0.20	0.54
GD02	K6	0.57	0.21	0.58

Both systems, TL-DOS albedo and the MPA GD02 albedo suggest that the N2 category is not appropriate. This is demonstrated in Figure 4.19, where the measurement of the reference fields and the field calibrations in the castor storage hall are presented for both dosimeter systems.

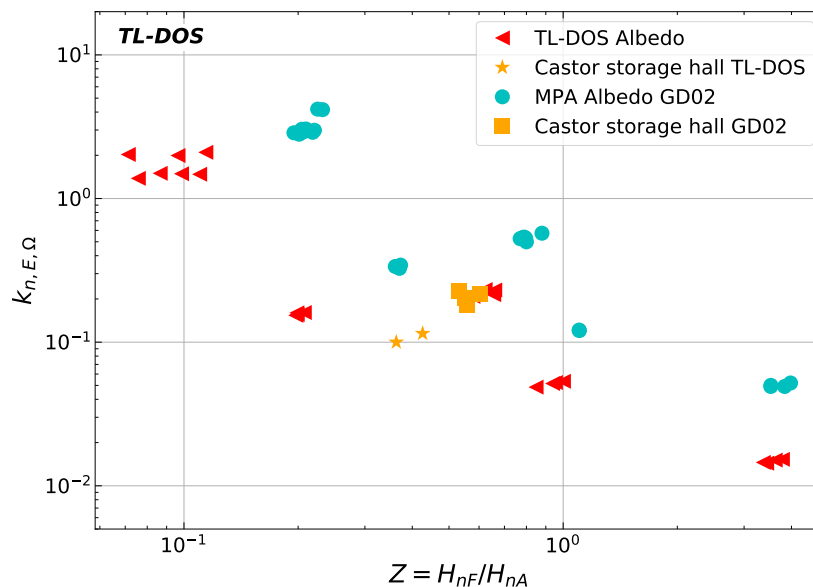


Figure 4.19: The correction factor k and ratio Z measured with the TL-DOS neutron system in red and with the MPA GD02 in blue. The results of the field calibrations in the castor storage hall are marked in orange stars (TL-DOS) and orange square (MPA GD02). All data are measured with different $H_p(10)$ doses.

Already in 1999, it was assumed by measurements performed in the nuclear power plant 'Kernkraftwerk Philippsburg' (KKP) that application in such fields should be classified in N1 category [70]. The individual dose monitoring AWST Munich has carried out comparable field calibrations on other castor storage facilities [70], which also yield the classification in N1. The annual report of the Safety Department of the Research Centre (2006) (report FZKA7330) also recommends the classification into N1 based on a field

calibration at the Philipsburg nuclear power plant.

Therefore, the measurements performed with the TL-DOS neutron system are communicated to the standard committee of the DIN. The committee has reconsidered the classification of the storage halls for fuel assemblies in certain areas during the revision of the DIN 6802-4:1998-04 and take the presented measurements and research into account.

4.4.5 Field calibrations at the proton therapy centre Essen

The West German Proton Therapy Centre Essen (WPE) operates a cyclotron to treat cancer patients with proton therapy. There are different treatment modalities to spread the proton beam for treatments. One is the double scattering. It uses two inserted scatterer in the pathway to spreading the beam in the lateral direction and creating a uniform dose in depth direction. Some protons are scattered and secondary particles like neutrons or especially high energy neutrons occur. Proton therapy is a growing industry, it is therefore very interesting to specify the neutron field produced during an irradiation. [71] Several field calibrations with different settings are performed during such irradiations in a treatment room. By these measurements it is possible to check the classification (N-category) of applications in proton therapy facilities for the TL-DOS neutron dosimeter.

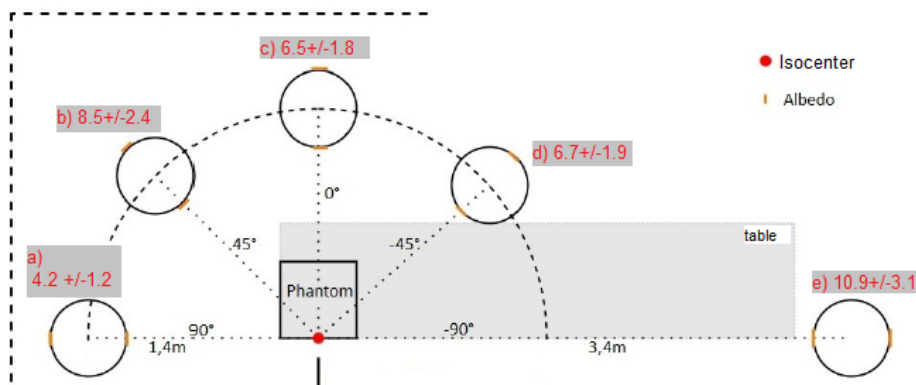


Figure 4.20: Five positions of field calibrations in a treatment room of the WPE. The RW3 plate phantom on the patient table is irradiated with protons in double scattering mode. At the positions a) - e) the $H_n^*(10)$ dose was measured in mSv in Ref. [51] with the Harshaw MPA system. The results are written in red.

Different positions in a treatment room were examined in Ref. [51]. Figure 4.20 shows the five positions and doses measured there with the Harshaw MPA albedo system accordingly. The field calibrations of Ref. [51] were performed around the patient table. At

position e), next to the table, the highest dose is found. At this location more scattered neutrons are produced in the room than at the other four positions because the measurement is performed closer to the table, where radiation scatter. For this reason, all field calibrations are performed with the presented TL-DOS neutron dosimeter at position e).

Figure 4.21 shows the setup used in detail. An RW3 plate phantom ((30x30x30)cm³, water equivalent) on the table is irradiated at gantry 270° position in double scattering mode with the following parameters:

- maximum proton beam energy $E=172$ MeV,
- modulated distal proton beam = R20M10,
- proton dose: 145 MU–2000 MU.

R is the beam range, M is the modulation and MU are the monitor units.

At a distance of 3.4 m the moderator phantom is placed next to the patient table to measure the secondary neutrons at an angle of $\alpha = 90^\circ$ to the beam's eye view. Four neutron badges are attached to each sphere and three irradiations with different proton doses are performed. After readout of the inner detector card, for each irradiation the $H_n^*(10)$ dose is determined by equation (4.1) and the results are shown in Table 4.8. The higher the proton dose and thus the irradiation time, the higher the neutron dose at position e).

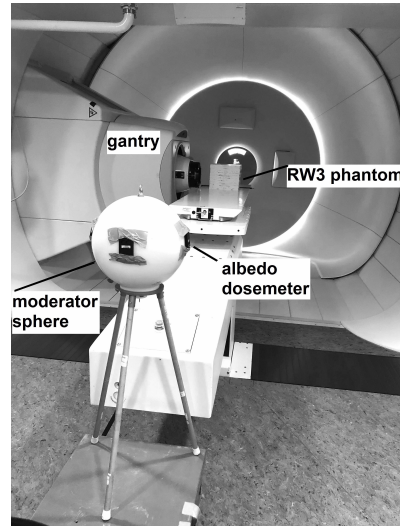


Figure 4.21: Setup to perform field calibrations with a neutron moderator sphere and TL-DOS neutron dosimeters in a treatment room of the WPE. The RW3 plate phantom on the patient table is irradiated with different proton doses and the secondary neutrons are measured at the point of the sphere.

Table 4.8: The calculated neutron ambient dose equivalent $H_n^*(10)$ for field calibrations at the WPE with various proton doses. The phantom is irradiated with protons and the scattered neutrons are measured at a distance of 3.4 m.

dose \ measurement	1	2	3
proton dose in MU	2000	1000	145
$H_n^*(10)$ in mSv	4.68 ± 0.41	2.57 ± 0.22	0.51 ± 0.04

The four albedo badges of one irradiation are calibrated and evaluated according to equations (2.16) and (4.3). The calculated k and Z factors are classified in the k - Z -

scatter plot as seen in Figure 4.22. After averaging, k results in

$$\bar{k} = 0.294 \pm 0.027.$$

The measurement indicates, that categories N3 or N4 are applicable in this situation because the values are between the measurements of the reference fields $^{252}\text{Cf}(\text{bare})$ and $^{252}\text{Cf}(\text{bare})+\text{shadow object}$ which simulates these categories.

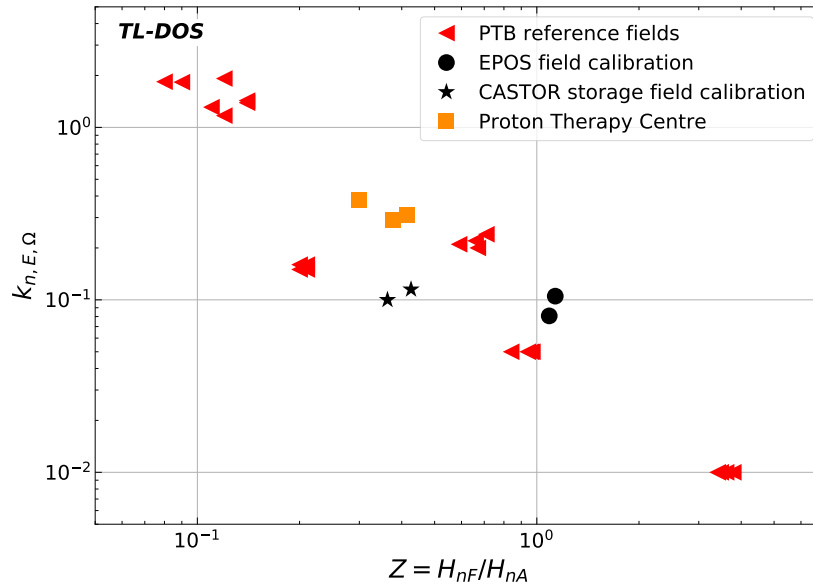


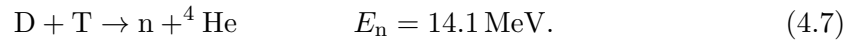
Figure 4.22: The correction factor k and the ratio Z measured with the TL-DOS neutron system. In orange the field calibrations at the WPE performed with different doses are marked. The field calibrations in a castor storage hall are the black stars, in red the data of the reference fields and as black dots the field calibration at EPOS are shown. All data are measured with the TL-DOS system but with different $H_{p,n}(10)$ doses.

4.4.6 Field calibration at a neutron generator

Further field calibrations are performed at a neutron generator at the Fraunhofer Institute for Technological Trend Analysis INT to test the TL-DOS neutron dosimeter in fields with high energies. The Fraunhofer Institute offers a neutron source from THERMO-Fisher D-711 which is suitable for investigations in security and material analysis.

Neutron generators produce neutrons by fusing isotopes of hydrogen. In this case deuterium ions are accelerated with 150 kV onto a target which contains tritium, see equation (4.7). The formation of an ^4He ion and a neutron with a kinetic energy $E_n = 14.1$ MeV

are the results.



The neutron emission is nearly isotropic because the neutron energy is much larger than the kinetic energy of the deuterium ions. In the irradiation room the neutrons scatter on walls and objects, so that the neutron field is not isotropic. The energy of the generated neutrons is at the upper limit of the dosimeter's requirement range (see Chapter 2.4). Calibrated uranium fission chambers monitor the neutron fluence during an irradiation at the Fraunhofer Institute. [72]

Field calibrations are performed at three different positions in the room with the TL-DOS system. Figure 4.23 shows a room plan with the setup of the neutron generator and three neutron moderator spheres (K4-K6).

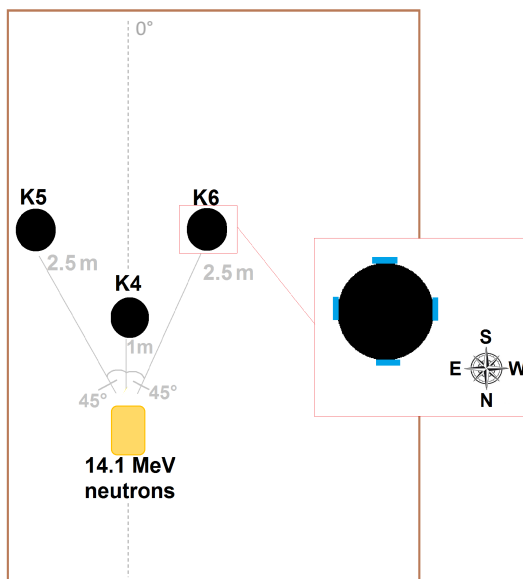


Figure 4.23: Setup for the field calibrations at a neutron generator which emits 14.1 MeV neutrons. Three measurements are performed at various positions at the same time. Additionally, the mounting of the albedo badges on a sphere is shown.

The fluence, irradiated dose and measured dose are listed in Table 4.9 for all nine cases. The irradiated dose is only applicable calculated for the spheres K4 because for all others the energy differs too much of 14 MeV and the fluence is unknown.

Three equipped spheres are irradiated simultaneously, so that one sphere is placed at each of the three positions during one irradiation. This procedure is repeated with three different neutron fluences to achieve different neutron doses. So a total of nine measurements are performed with three irradiations. From the fluence the irradiated neutron dose is determined with equation (2.10).

According to Ref. [22] the energy-dependent conversion factor P_E is assumed to be $P_E = 384 \text{ pSv}\cdot\text{cm}^2$ for $E = 14 \text{ MeV}$. The detector card in the sphere is evaluated and the measured ambient dose $H_{n,\text{meas}}^*(10)$ at the point of the sphere is determined by equation (4.1).

Table 4.9: The irradiated and measured neutron ambient dose equivalent $H_n^*(10)$ and setup parameters for field calibrations at the Fraunhofer Institute for different irradiation.

irradiation	sphere	fluence in n/cm ²	$H_{n,irrad}^*(10)$ in mSv	$H_{n,meas}^*(10)$ in mSv
1	4	$1.30 \cdot 10^7 \pm 20\%$	5 ± 1	5.0 ± 0.4
	6			1.36 ± 0.12
	5			1.41 ± 0.12
2	4	$3.92 \cdot 10^7 \pm 20\%$	15 ± 3	16.2 ± 1.4
	6			4.97 ± 0.43
	5			4.55 ± 0.39
3	4	$7.84 \cdot 10^7 \pm 20\%$	30 ± 6	33.0 ± 2.8
	5			10.01 ± 0.87
	6			9.61 ± 0.83

Within the uncertainty the irradiated and the measured ambient doses are in a good agreement. As expected, the dose of the measurements, which are far away from the source and irradiated at an angle of 45° to the center axis of the generator, is lower. Since at a larger distance the neutrons scatter more, less neutrons reach the sphere at these points.

In addition, the four albedo dosimeters, which are located outside the sphere during irradiation, are evaluated. Respectively, for the opposite dosimeters (N+S and W+E) the factors k and Z are determined and shown in Figure 4.24 for different doses.

The largest value found for the k factor is in the same range as the factor for the $^{241}\text{AmBe}$ reference field. Based on the measurements performed so far it is claimed that this is the maximum value for the TL-DOS k factor in general.

If the results for all positions K4–K6 are compared with each other, all expectations are confirmed. At position K4 the highest k factor is found because the dosimeters are closest to the neutron source. Based upon the fact that the distance between the generator and position K6 is larger, more scattered and moderated neutrons are measured by the dosimeters there. This results in a smaller k factor. Due to the same distance, the factors for position K5 are very similar to those for position K6. However, next to this position there is a wall where the neutrons are moderated. Therefore, a slightly smaller k is found for this position.

This is also the reason why the values on the Z -axis scatter most strongly for this position. The sphere at K6 is furthest away from the walls and other objects. Therefore, the scattered radiation is very uniform and the resulting factors and ratios show only a small deviation.

In comparison to the k factors from the N+S dosimeter pairs, the k factors from the W+E dosimeter pairs always have larger numerical values for the Z ratio. More thermalized neutrons are measured at the side of the sphere because the dosimeters are not directly suspended in generator direction. The more thermal neutrons in the field the smaller is the k factor and the larger is the Z -ratio.

A dependence of the dose could not be determined for the two factors, k and Z . All measurements at the neutron generator are classified in category N4.

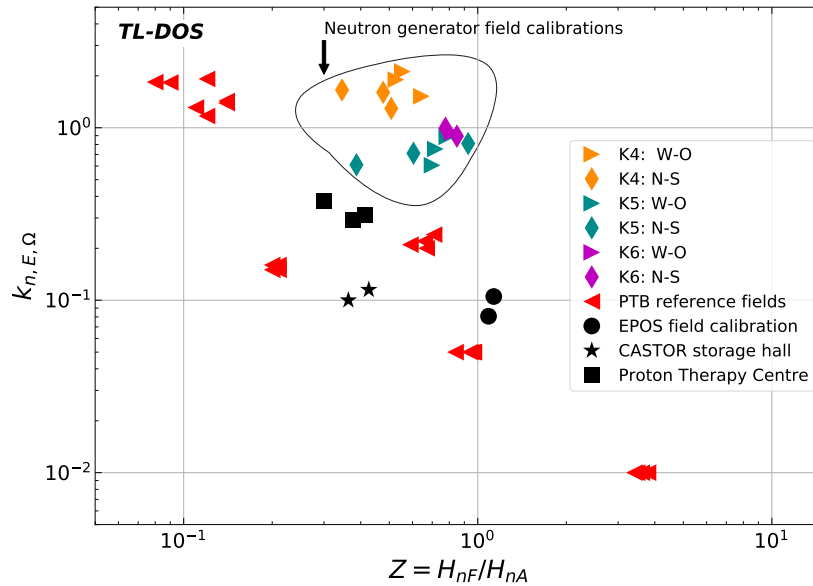


Figure 4.24: The correction factor k and ratio Z measured with the TL-DOS neutron system. The field calibrations in a castor storage hall are the black stars, in red the data of the reference fields, in black the field calibration at EPOS and the field calibrations at the WPE. In the circled area different field calibrations performed at the Fraunhofer Institut with various $H_{p,n}(10)$ doses are shown. The positions of the sphere in the room are marked with orange, cyan and magenta and the symbols differ the albedo badge position.

All four applications and N categories for the TL-DOS dosimeter have been tested by performing field calibrations in different workplace fields. All recorded measurements are arranged near to the reference field data. This confirms that the TL-DOS system works and can be used for various applications to estimate the personal neutron dose $H_{p,n}(10)$ in routine dosimetry.

The next step is to check whether the dosimeter fulfills further requirements for the official design certification, such as the estimation of the photon dose.

Chapter 5

Supplementary requirements for the new neutron dosimeter

As the German 'Eichgesetz' [19] does not provide any regulations for the official verification of neutron dosimeters, no official design certification is possible (see Chapter 2.4). Therefore, no official design certification is necessary for neutron dosimeters before use in routine individual monitoring to measure the neutron dose. The successful participation in the comparison measurements of the PTB is sufficient.

However, the dosimeter is carried in photon + neutron mixed fields and thus, it also measures the photon dose $H_{p,\gamma}(10)$. Consequently, an official design certification to estimate the photon dose is mandatory for a neutron dosimeter and the new TL-DOS neutron dosimeter has to meet the requirements of photon dosimetry [20].

This chapter reviews some of these requirements for the new TL-DOS neutron albedo dosimeter. First, the X-ray irradiation facility used for investigations and characterizations of the new system in photon fields is briefly introduced. Second, photon energy and angular dependence of the TL-DOS neutron dosimeter are examined and the beta criterion is discussed. Finally, the detection limits are determined and results from high-dose photon irradiations are reported.

5.1 The X-rays facility of the MPA NRW

So far in this thesis, all irradiations with photon fields were performed at the ^{137}Cs facility. Since this facility only emits photons with an energy of 662 keV, an additional irradiation facility like the X-ray facility of the MPA NRW is required to check the energy dependence of a dosimeter. With this X-ray facility, it is possible to vary the photon energy and the dose rate as voltage and current of the X-ray tube, irradiation time and distance from the X-ray tube can be varied. The photon energy spectrum is varied via a filter wheel (Figure 5.1 (left)) localized behind the X-ray tube (in beam direction). Photon energies

from 18 keV to 120 keV can be achieved.

The generated photon energy spectra consist of a continuous spectrum of bremsstrahlung and peaks of the characteristic radiation. A distinction is made between narrow spectra (ISO:N series), wide spectra (ISO:W series) and high air kerma spectra (ISO:H series) [20]. For example, for an N-40 energy spectrum, the maximum energy is 40 keV and the averaged photon energy is 33 keV. In this thesis the N-qualities are used, as recommended in [73].

Behind the filter wheel, two apertures (Figure 5.1 (right)) limit the radiation field to the measuring range. For irradiation, a carrier is positioned at different distances in the radiation field via a rail system. An ionization chamber (Figure 5.1 (right)) for measuring the air kerma or a phantom for irradiating a personal dose can be set up on the carrier. Additionally, the carrier can be rotated for angular irradiations.

Photon irradiations of the TL-DOS neutron dosimeter are carried out with different photon energies between 33 keV–662 keV by using the X-ray and ^{137}Cs facilities.

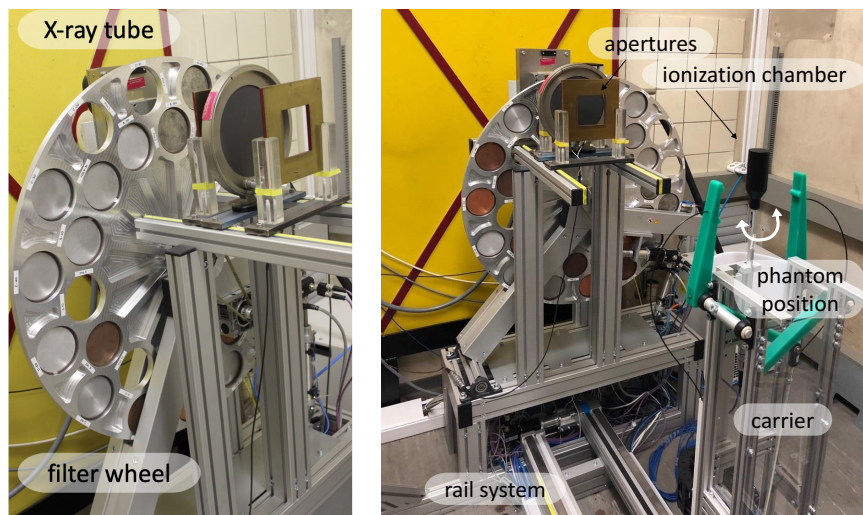


Figure 5.1: Two photos of the X-ray facility. Left: Filter wheel with different filters to modify the photon energy spectrum. Right: Apertures to focus the field and the ionization chamber on the carriage to measure air kerma.

5.2 Energy and angular photon response of the dosimeter

A dosimeter has to be able to detect photon doses from 0.1 mSv to 1 Sv accurately in the energy E_γ and angular α range [18]:

$$80 \text{ keV} < E_\gamma < 1.25 \text{ MeV}, \quad -60^\circ < \alpha < +60^\circ. \quad (5.1)$$

The achievement of even lower energies than 80 keV, down to 30 keV, would be desirable to ensure correct application in even more areas, e.g. at an X-ray facility in a hospital. In this range, the measured dose must not deviate more than -29% and +67% from the irradiated dose [20].

To calculate the energy and angle dependence of a dosimeter, the measured signal is normalized by the signal of a reference irradiation. In this thesis, the signal of a ^{137}Cs irradiation at 0° is used for normalization. This approach is recommended in DIN EN 62387 [15] and the response (see equation (2.8), too) is calculated with

$$R = \frac{M(E_\gamma, \alpha)}{M(Cs = 662 \text{ keV}, 0^\circ)}. \quad (5.2)$$

From the theory [74] and previous works [14, 75] it is known that the response of LiF:Mg,Ti shows a dependence of the irradiation energy, see Figure 5.2.

Compared to other dosimetry materials, LiF:Mg,Ti has a flat response and has a maximum at about N-40 ($\bar{E}_\gamma = 33 \text{ keV}$). Quantified is the maximum at about $R = 1.3$. There is a minimum with a response less than one at about $E_\gamma = 80 \text{ keV}$, before the response levels off towards $R = 1$ for higher energies.

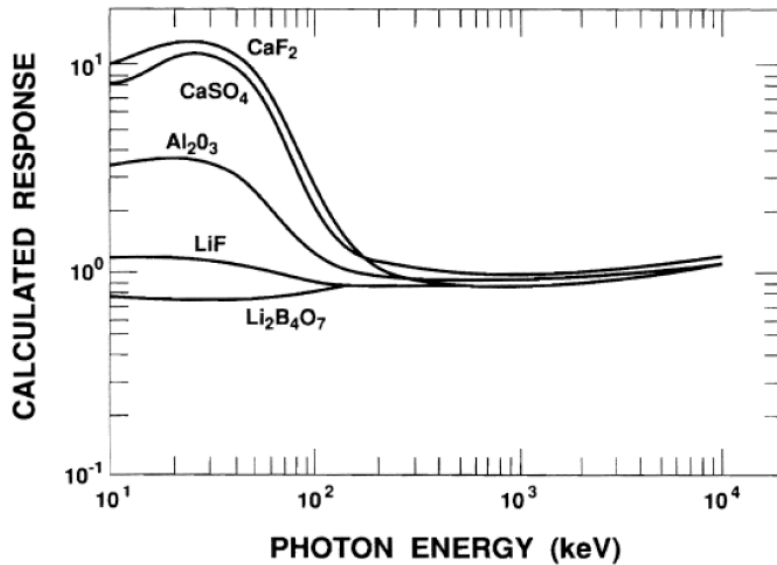


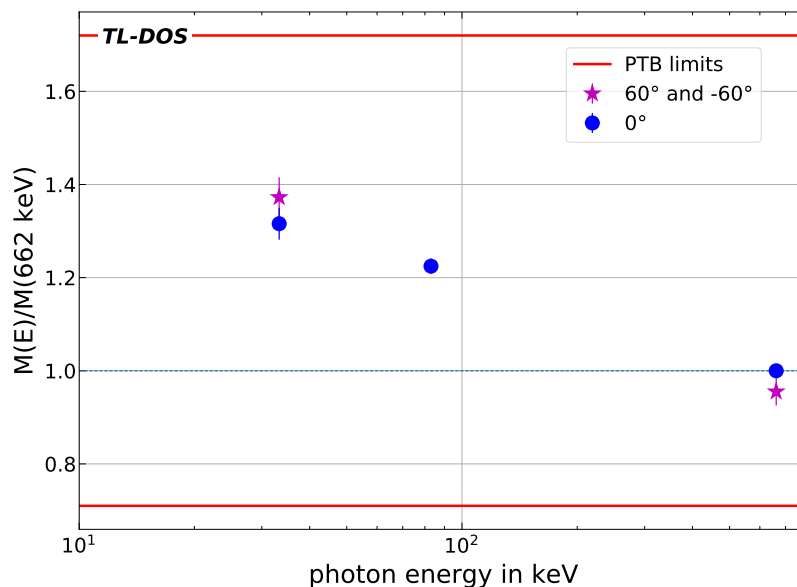
Figure 5.2: Theoretical response of different thermoluminescence materials. [74]

TL-DOS albedo badges are irradiated at a slab phantom with varying angles and photon energies at the X-ray and ^{137}Cs facilities to check the energy and angle dependence. The same dose ($H_{p,\gamma}(10) = 1 \text{ mSv}$) is used for all irradiations. A list of the irradiations carried out is shown in Table 5.1. The irradiation settings are chosen to consider all distinctive points (see Figure 5.2). One albedo badge contains four detectors (see Chapter 3.4), of

Table 5.1: Irradiation program of the TL-DOS neutron dosimeter to proof the energy and angular dependence by means of key points.

irradiation quality	\bar{E}_γ in keV	angel α	# badges
N-40	33	0°	8
N-40	33	60°	4
N-40	33	-60°	4
N-100	83	0°	4
N-100	83	60°	4
^{137}Cs	662	0°	8
^{137}Cs	662	60°	4
^{137}Cs	662	-60°	4

which usually only the detector at position 3 (albedo detector with Li-7), referred as Li7-A detector, is used for estimation of the photon dose (see Section 2.7.2). For these Li7-A detectors, the response (equation (5.2)) is calculated and for every irradiation scenario the mean is determined. Figure 5.3 shows the results found as mean values with their standard errors of mean in dependence of the photon energy. Furthermore, the 0° and 60° irradiations are shown in different colors. The 60° and -60° irradiations are summarized in this figure because same results are expected for these measurements based on measurements with other TL-DOS dosimeter systems. The standard errors of mean are displayed for all data points, but are partially smaller than the dot-size.


Figure 5.3: Photon response of the TL-DOS neutron dosimeter depends on energy and angle. Irradiated with $H_{p,\gamma}(10) = 1$ mSv on a slab phantom. The maximal and minimal limits for the response are illustrated in red.

For the data recorded at 0° , a typical LiF:Mg,Ti curve is found with the highest response ($R = 1.31$) for N-40. The fact that angle irradiations of these energies result in a higher response ($R = 1.37$) than at 0° is also expected and has already been discussed in Ref. [14]. In case of an angular irradiation, the distance traveled by the particle in the sensitive material is larger compared to an 0° irradiation. This effect prevails at low photon energies. However, for higher photon energies the signal decreases at angular irradiations, because the solid angle effect dominates. The amount of the field of view from the detector is smaller in this case. The result of the measurement A-100 60° is equal to its 0° irradiation. The result of the 60° irradiation for ^{137}Cs (662 keV) is 4.5% below the 0° irradiation as already presented in [49] and [75] for another TL-DOS dosimeter using detectors with a diameter of 7 mm.

It is confirmed that the response for all measurements is within the limits of the PTB, which are marked in the figure in red. Thus, it is assumed that all further measurements would fulfill the requirement and the dosimeter is suitable for the whole required range (equation (5.1)).

To analyze the angular dependence in more detail, the data of angular irradiations are not combined in the following considerations. So it can be checked whether the dosimeter behaves in the same way for the rotation in both directions. For this purpose, the data of $\alpha=60^\circ$ and $\alpha=-60^\circ$ are considered separately for two energies in Figure 5.4 (left).

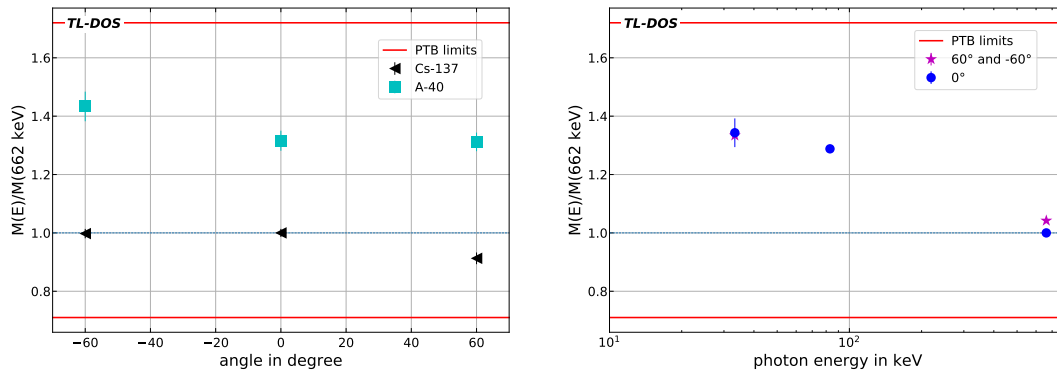


Figure 5.4: Left: Angular dependence of the TL-DOS neutron dosimeter response for two different photon irradiation energies (33 keV and 662 keV). Right: Energy and angular photon response of the TL-DOS neutron dosimeter after evaluation of the detector Li6-A instead of Li7-A. Again the given limits are drawn in red.

Generally, the angular response is very flat. In both cases, the response is 9% lower for $+60^\circ$ than for -60° , which suggests a systematic effect. For an irradiation, the center of the badge is fixed on the rotation axis (in y direction) of the phantom. Since the Li7-A detector is not located in the middle of an albedo badge (see Chapter 3.4), the position of the detector and especially the distance between the detector and the source depends

on the rotation direction. On the detector with the smaller distance to the source (-60°) a higher dose is induced than on the detector irradiated at 60° . Possible causes for this phenomenon are not only the different solid angle (approx. 3%) but also shielding and dose-building effects. Nevertheless, all results are within the limits prescribed by the PTB.

Furthermore, the compliance of the limits is also verified for the other detectors of the albedo badge. These could serve as a measurement backup for estimating the photon dose in case of damage to the Li7-A detector. The evaluation has been repeated for all three remaining detectors and the results for detector Li6-A (position 4) are presented in Figure 5.4 (right). For the Li6-A detector, the standard deviation is at a maximum value of 6% similar to the one for the Li7-A detectors (5%). This highlights the high quality of the whole dosimeter system and this detector can also be used for evaluation.

This fact can be beneficial to get more information about an irradiation from a single detector, which is discussed in more detail in Chapter 6.

5.3 Beta criterion for photon dosimetry

Dosimeters for the measurement of the photon $H_{p,\gamma}(10)$ dose have to meet another requirement in Germany, called the beta criterion [18].

The indicated $H_{p,\gamma}(10)$ signal by beta radiation must not exceed 10% of the true $H_p(0.07)$ value. Mathematically it is written as

$$\frac{M(H_p(10), Sr - 90)}{M(H_p(0.07), Sr - 90)} \leq 0.1. \quad (5.3)$$

M is the measured signal for the corresponding dose after a ^{90}Sr beta irradiation.

In this thesis, the beta criterion is not investigated by experiments because Ref. [56] already dealt with this question and discussed it because of its importance for badge and filter designs. After several filters were tested by simulations, a satisfactory result was found for the boral filter of the albedo badge used (see Chapter 3.4).

Furthermore, the TU Dresden University carried out simulations with different materials to select a filter for the TL-DOS whole-body photon system [76] in 2015. They found that a 2 mm boral filter as used in the albedo badge meets the beta criterion. In summary, the TL-DOS neutron dosimeter will fulfill this requirement very likely.

5.4 Photon decision threshold and detection limit of the neutron dosemeter

The decision threshold (DT) and the detection limit (DL) quantify the lower limit of the dose range that is still measurable.

If a value above DT is measured, it can be assumed that there has been an exposure to radiation. The signal induced by radiation can be separated from the background.

DL is the smallest dose value above this limit which can reliably be detected. All dose values higher than the detection limit can be affirmed as correct and the dose can be determined accurately.

These two quantity limits vary dependent on the measuring method and dosemeter system. Figure 5.5 uses Gaussian distributions to illustrate the quantities [77].

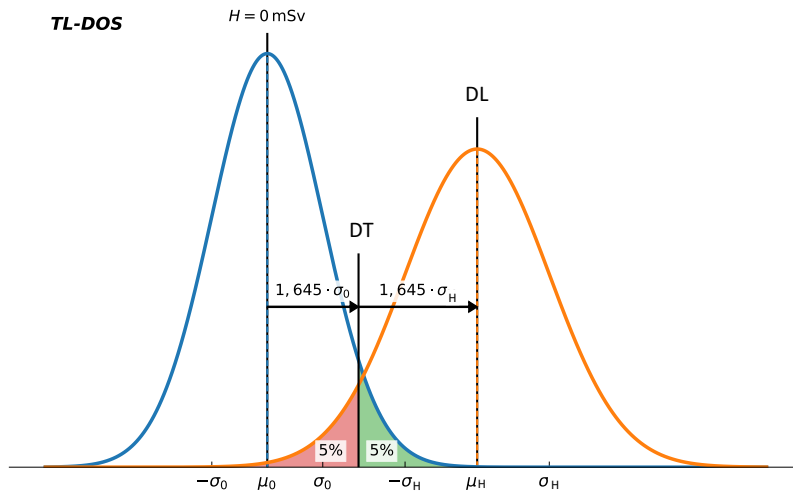


Figure 5.5: Illustration of the decision threshold (DT) and detection limit (DL) of a dosemeter system explained by normal distribution. In dosimetry, the significance level is usually set to 5%.

The decision threshold is determined by a hypothesis test, assuming a normal distribution. In dosimetry, a significance level of 5% is assumed, resulting in the quantiles $K_{1-\alpha} = K_{1-\beta} = 1.64$.

Dosemeters which measure the photon dose equivalent $H_{p,\gamma}(10)$ have to meet the requirement that they can reliably detect at least a dose of 0.1 mSv. To estimate DT and DL for the albedo dosemeter, the following equations are used:

$$DT = \mu_0 + K_{1-\alpha} \cdot \sigma_0, \quad (5.4)$$

$$DL = DT + K_{1-\beta} \cdot \sigma_{0.1} \quad (5.5)$$

μ_0 is the averaged measurement value of the detector after read out without an irradiation beforehand, and σ_0 is its standard deviation. $\sigma_{0.1}$ describes the standard deviation of the measured detector signals after an irradiation with $H_{p,\gamma}(10) = 0.1$ mSv.

However, the dosimeter can only be read out once because the signal is deleted during the measurement. Hence, the same measurement cannot be repeated and the standard deviation of a measurement cannot be calculated in this way. Therefore, alternative considerations of possible influences (see Table 5.2) are collected and used to calculate DL. The principle for the determination of the decision threshold and the detection limit is described and prescribed in DIN ISO 11929 [77]. Therefore, equations (5.4) and (5.5) are used, where μ_0 is set to zero because a measurement of unirradiated detectors should result in a dose $H = 0$ mSv.

There are three models which include different parameters for the calculation of the photon dose equivalent $H_{p\gamma}(10)$ and the uncertainty \bar{u} respectively. While G1 is the base model, G2 supplementary includes energy and angular uncertainties by the correction coefficients $k_{E,\alpha}$ and G3 respects the uncertainty of the natural background radiation H_{nat} additionally. For these models, $H_{p,\gamma}(10)$ is calculated as follows:

$$H_{p\gamma}(10)_{G1} = \frac{S_\gamma + b'}{m'}, \quad (5.6)$$

$$H_{p\gamma}(10)_{G2} = k_{E,\alpha} \frac{S_\gamma + b'}{m'}, \quad (5.7)$$

$$H_{p\gamma}(10)_{G3} = k_{E,\alpha} \left(\frac{S_\gamma + b'}{m'} - \dot{H}_{\text{nat}} \cdot t \right). \quad (5.8)$$

Where S_γ is defined as the measured signal after an irradiation with photons and m' and b' are calibration factors to determine the photon dose $H_{p,\gamma}(10)$, see Chapter 3.5. The standard deviation \bar{u} for the three models results in:

$$\bar{u}(H_p(d)_{G1}) = \bar{u}(H_p(d)_{G3})(t = 0, \bar{u}(k_{E,\alpha} = 0), k_{E,\alpha} = 1), \quad (5.9)$$

$$\bar{u}(H_p(d)_{G2}) = \bar{u}(H_p(d)_{G3})(t = 0), \quad (5.10)$$

$$\begin{aligned} \bar{u}(H_p(d)_{G3}) = & \left[k_{E,\alpha}^2 \left(\bar{u}^2(H_{\text{nat}}) + \left(\frac{\bar{u}(S_\gamma)}{m'} \right)^2 + \left(\frac{\bar{u}(b')}{m'} \right)^2 \right. \right. \\ & \left. \left. + \left(\frac{S_\gamma + b'}{m'^2} \bar{u}(m') \right)^2 \right) \right. \\ & \left. + \left(\frac{S_\gamma + b'}{m'} - \dot{H}_{\text{nat}} \cdot t \right) \bar{u}(k_{E,\alpha}) \right]^{1/2}. \end{aligned} \quad (5.11)$$

With these estimates of the standard deviation and equations (5.4) and (5.4), DT and DL can be calculated for all 3 models. In Ref. [47] the detection limit (according to G3

with measured natural background radiation) for the whole body TL-DOS dosimeter is determined to 30.96 μSv . With this it fulfills the requirement.

To calculate the quantities (DT and DL) for the TL-DOS neutron dosimeter for all models, the values in Table 5.2 are determined from the measurements presented in Chapters 3.5 and 5.2.

Table 5.2: Compound uncertainties for the determination of DT and DL.

uncertainty	parameter	average	sigma \bar{s}
energy and angular	$k_{E,\alpha}$	1.05	0.01
natural background	\dot{H}_{nat} in $\mu\text{Sv/d}$	1.83	1.00
calibration factors (transformed) (Li7-A)	m' in $\frac{1}{\text{mSv}}$	4288	33
	b'	71	52
calibration factors (transformed) (Li6-A)	m' in $\frac{1}{\text{mSv}}$	4175	58
	b'	27	80

Transformed calibration factor (in Table 5.2) means that the frame factor (Section 3.5.3) has already been taken into account. Detectors are measured directly after erasing them to calculate the decision threshold for the neutron dosimeter. As a result, only detector and reader background is measured.

As already described in Section 3.3.2, the background increases with increasing temperature. This results in a higher decision threshold for measurements at 653 K. Therefore, not only ^6Li and ^7Li but also 573 K and 653 K measurements are distinguished. For all variants, twelve detectors are measured. The results according to equations (5.4) and (5.5) are listed in Table 5.3. The model G3 is divided into a sweeping and a measured one. Since the sweeping G3 model estimates the background in a generalized manner, it is rather inaccurate. The natural background is measured with detectors and subtracted for the model measured G3.

Neutron badges are irradiated with $H_{p,\gamma}(10) = 0.1 \text{ mSv}$, as this is the minimum requirement, before the signal average and standard deviation are calculated. For an accurate calculation the standard deviation has to be determined by a few measurements of different doses and a subsequent specific compensation function. The exact value is not important, but it is only determined whether the limit can be fulfilled in principle. Therefore, the used standard deviation of the required limit is sufficient and it is not necessary to determine the standard deviations for various doses to find a subsequent specific compensation function.

The decision threshold is determined with equation (5.4) and results in lower values for the Li7-detector than for the Li6-detector. Furthermore, a higher read out temperature results in a higher DT.

As result of a higher decision threshold, the detection limit is also higher for measure-

ments at 653 K. Table 5.3 shows that a higher decision threshold is reflected in a higher detection limit. With equation (5.5) the detection limits of the detector used for photon dose calculation (Li7-A detectors) result to 52 μSv . For measurements at 653 K, the value of the detection limit is 34% higher.

The detection limit for the Li-6 detectors is slightly higher than the limit of the Li-7 detectors, because a higher uncertainty was found for the calibration of these detectors. They still meet the limit of 100 μSv , see Table 5.3.

A detection limit is found that is acceptable for 10 mg detectors in albedo badges for both temperatures measured. The presented neutron dosimeter passes the test.

The decision threshold and detection limit could be improved by renewing the PMT whose sensitivity has decreased a lot during the time, see investigations in Section 3.3.4. The decision threshold can be reduced with an improved reader's own background separation to get an even better result.

Table 5.3: Decision threshold (DT) and detection limit (DL) for the Li6-A and Li7-A detectors of the TL-DOS neutron dosimeter. Once measured at 573 K and once performed at 653 K. The marked value is the one which is required by the PTB. This dosimeter passes the test.

model	temperature in K	detector	DT in μSv	DL in μSv
G1	573	Li7-A	26	47
		Li6-A	36	73
	653	Li7-A	34	64
		Li6-A	48	92
G2	573	Li7-A	27	51
		Li6-A	34	71
	653	Li7-A	37	67
		Li6-A	47	98
G3 (sweeping)	573	Li7-A	58	115
		Li6-A	58	117
	653	Li7-A	63	124
		Li6-A	66	135
G3 (measured)	573	Li7-A	28	52
		Li6-A	35	73
	653	Li7-A	37	70
		Li6-A	47	99

5.5 High-LET peaks induced by a high photon dose

In order to determine whether only a photon irradiation or an irradiation with additional neutron radiation has taken place, the high-LET peaks, which result from irradiation

with high-LET particles (Chapter 3), are used.

However, the literature states that high dose irradiation also produces high-LET peaks. E.g. in Ref. [35] a glow curve that shows also peaks in the high temperature region is presented after irradiation with photons (^{60}Co).

Figure 5.6 (left) shows a glow curve measured with the TL-DOS system after an irradiation with 3.8 Sv (^{137}Cs). Compared to a photon irradiation with a lower dose (see Figure 5.6 (right, above)), a clearly increased signal in the area of the high-LET peaks is recognized for this glow curve. For the TL-DOS system and doses in personal dosimetry dose range, these peaks are usually vanishingly small [4]. Therefore, they cannot be separated from the background.

The high temperature peaks are not only visible and separable of the background after a high-LET irradiation, but also with a sufficiently high photon dose. Doses approximately $>1\text{ Sv}$ are referred to as high dose in the field of personal dosimetry.

Glow curves irradiated with neutrons can be distinguished from high photon dose induced signals. Compared to peak 5 the high-LET peaks are more pronounced for low dose neutron radiation as after a high dose photon irradiation, compare Figure 5.6 a and c. Therefore, it is notable that there are even more information in a glow curve than those about the dose. How these or other observations can be used for further information is examined in Chapter 6.

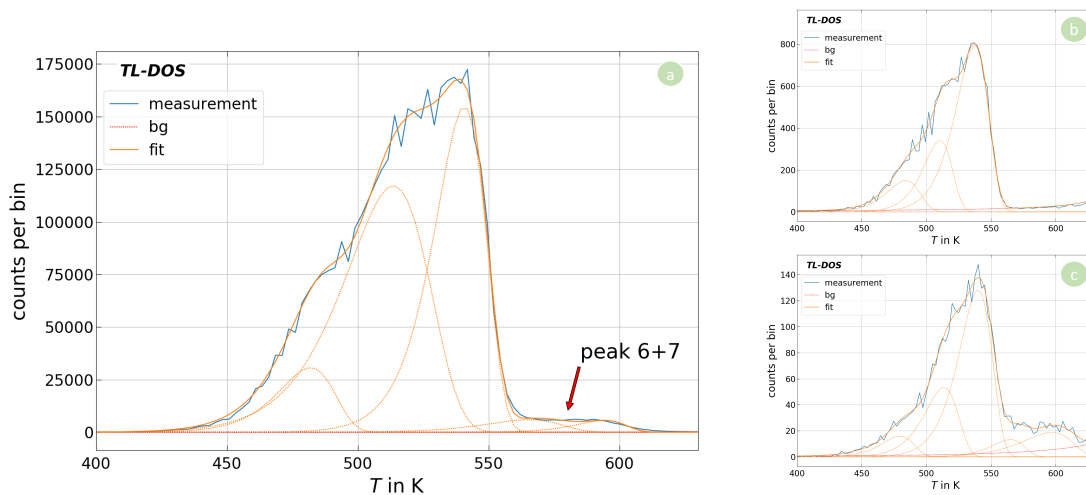


Figure 5.6: Three glow curves with its individual fitted peaks, background and smoothed data measured after different irradiation a) high dose 3.8 Sv photon irradiation with ^{137}Cs b) 5 mSv photon irradiation with ^{137}Cs c) 3 mSv neutron irradiation in a reference field of the PTB.

The measurements presented above show that the TL-DOS neutron dosimeter fulfills all

requirements defined by PTB. After the dosimeter has been characterized in the photon fields and in various neutron work place fields (Chapter 4) this albedo dosimeter version could be used in the routine operation of an individual monitoring service.

In addition, it was shown in Chapter 5.5 that the additional measurement of high-LET peaks offers a gain in information. Not only the fact that a glow curve consists of more counts and consequently, the statistical error is smaller, but also the possibility that the high-LET peaks contain more information about the previous irradiation, make the evaluation and analysis of these peaks very interesting. Therefore, the high temperature peaks will be examined in more detail in the following chapter.

Chapter 6

High-LET peaks and their prospects for additional irradiation information

This chapter deals with the additional measured signal, the high-LET peaks of a glow curve in more detail. The signal is observed not only after irradiation with neutrons, but generally after an irradiation with high-LET particles or high photon doses. In the TL-DOS project, it is easier to perform irradiations with alpha particles than neutron irradiations because an alpha irradiation source is available at the MPA NRW.

First, a setup for high-LET irradiations with alpha particles is presented and calibrated. The calibration and adjustment measurements include a verification of a signal-to-irradiation time relationship of the TL-DOS system for alpha irradiations, studies of the post-irradiation fading effect after high-LET irradiations and a comparison of neutron and alpha induced glow curves.

Second, the energy dependence of individual glow peaks is considered, especially the dependence of the high-LET peaks is investigated. Single peak integrals are used to define a classification method of measured glow curves into one of the three groups of alpha, neutron or gamma irradiation.

Third, a new analysis based on the evaluation of the high-LET peaks is developed to gain more information like the alpha and gamma composition of an irradiation. Since it is very beneficial for mixed irradiations and especially useful for neutron dosimeters the dose calculation method is transferred to neutron+photon mixed irradiations.

6.1 The alpha irradiation setup and alpha induced glow curves

In this thesis, all alpha irradiations are performed with the so-called alpha irradiator of the MPA NRW (Fig. 6.1). In contrast to previously presented measurements, TL-DOS standard detectors are used for investigations of alpha-particle irradiations. Instead of the Li-6 and Li-7 neutron chips, TL-DOS whole-body detectors [46] with a diameter of 17 mm

and Li-N (MT-N, see Chapter 3.2) as thermoluminescence material are irradiated to conduct studies with alpha particles. Due to the larger size, these detectors are produced with a larger amount of TL material and therefore they have a higher sensitivity.

The irradiator device developed and characterized in Ref. [78] is shown in Figure 6.1 (left). For irradiation, a detector (1) is placed in the carousel (2). As the carousel rotates, a detector is positioned under the alpha source, which is inserted into the holder (3) before. A detector is irradiated for a certain amount of time, while the distance between the source and the detector is 2 mm. For all investigations presented in this chapter, the alpha source (Figure 6.1 right) is an ^{241}Am coin, which mainly emits alpha particles with an energy $E = 5.5 \text{ MeV}$ and has an activity of $A = 5.6 \text{ kBq}$.

For different irradiation times, the signal has been calibrated to a photon irradiation performed with the MPA ^{137}Cs facility. It is defined that an alpha irradiation with this setup and an irradiation time $t = 715 \text{ s}$ corresponds to a ^{137}Cs irradiation with $H_x = 5 \text{ mSv}$ (see Chapter 3.5) [78].

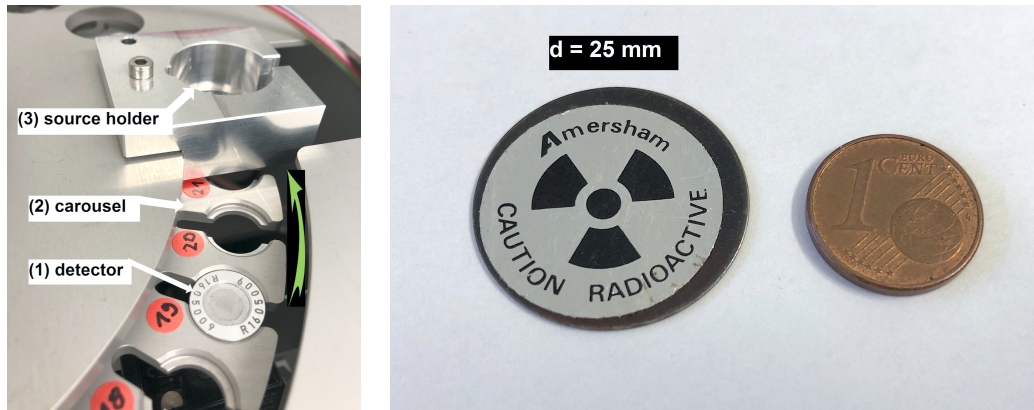


Figure 6.1: Left: Alpha irradiator at the MPA NRW with (1) a TL-DOS whole-body detector (2) a detector carousel and (3) a source holder. The carousel is rotatable so that a detector can be placed under the source for a certain time. Right: ^{241}Am source and a 1-cent-coin to compare the sizes. The source has a half-life $t_H = 432.2 \text{ a}$ [78].

With the combination of the alpha irradiator and TL-DOS whole-body detectors, signals for different irradiation times between 300 s and 2000 s are recorded to calibrate the system before usage. For each setting time 5–10 measurements are carried out and are averaged. The detectors are measured with the TL-DOS readout device as described in Chapter 3.3 in order to analyze the signal of the high-LET peaks of the glow curve.

As described in Chapter 4.2, the recorded glow curves are evaluated once with the TL-view program and once with the tool GCana.py (Section 3.6.2). Thus, it is possible to check whether GCana.py is not only suitable for neutron glow curves but also for alpha signals. The results are shown in Figure 6.2, where the entire net integral, including the

high-LET peaks, is plotted versus the irradiation time. A linear relationship is found for the net integral as function of the irradiation time. Since the blue and red points of the two evaluation methods differ very slightly from each other and the two fitted linear functions are within agreement, it is found that the evaluation of the alpha curve works with both tools and the analysis tool adapted to neutron glow curves can be applied to the alpha particle induced signal as well.

In addition, the irradiations are repeated with a larger distance between the source and the detector to test irradiations with different energies. The irradiation energy is reduced with a larger distance, base upon the fact that alpha particle lose a part of their kinetic energy in the air through collisions.

For this purpose, rings of different thicknesses (see Figure 6.2 (right, above)) are placed under the source during an irradiation. All results analyzed with GCana.py are shown in Figure 6.2 (right). For each distance, a linear relationship between the signal and the irradiation time is determined. However, both data have different gradients. It applies the greater the distance, the less signal is induced on the detector during the corresponding time because the alpha particles, which reach the detector, have a lower energy. Moreover, less alpha particles reach the detector.

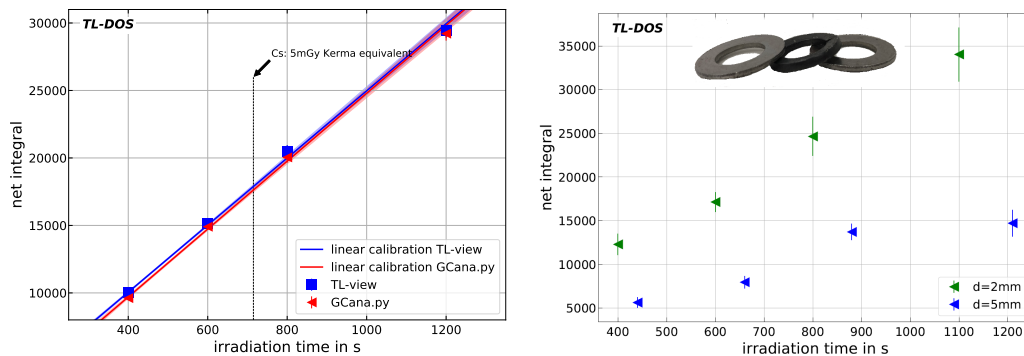


Figure 6.2: Averaged net integral of the total glow curve after different alpha irradiations with its standard error of mean. TL-DOS whole-body detectors readout at 653 K after a pre-temper step. Left: For two different glow curve analyses tools. Right: For two different distances between detector and source.

6.1.1 Signal of the high-LET peaks depending on the dose

The linearity of the glow peaks 1–5 to the dose is well known [47], whereas the high-LET peaks (peaks 6+7) are often referred to as supralinear [79]. In the supralinear range, the glow curve signal is not linear to the dose. Based on this fact, the linearity of the high-LET peaks has to be checked in the dose range used, before further investigations can be made.

As expected, a linear relationship can be confirmed for these peaks as well because the total integral in which the high-LET peaks are included is linear with dose (see Figure 6.2). All peak integrals of the measurements are considered individually up to peak 6 and peak 7 which are summarized because, due to the large overlap of the high-LET peaks and the uncertainty on their peak temperature, the fit may not separate these two clearly, see Section 3.6.3.

Figure 6.3 shows the averaged integral of the high-LET peaks plotted versus the irradiation time and its standard error of mean is also plotted. The data are fitted with a linear function $y=m\cdot x+b$. In the measured dose range, the correlation is assumed as linear because the fit-to-measurement-deviation, presented in the bottom part of the figure, is small with values of $\pm(2-10)\%$.

After the time-to-signal-calibration of the alpha irradiator is completely specified, it can be used to investigate the high-LET peaks.

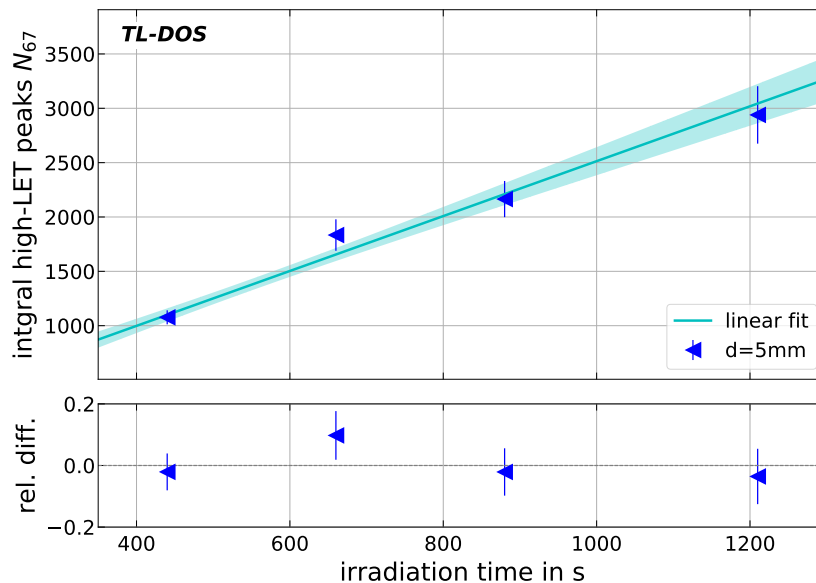


Figure 6.3: Averaged net integral of the high-LET peaks (6+7) of a glow curve after different alpha irradiations with its standard error of mean. TL-DOS whole-body detectors readout at 653 K after a pre-heating step and deconvoluted by GCana.py in its individually peaks.

6.1.2 Alpha induced glow curve vs. neutron induced glow curve

During an irradiation with neutrons, the sensitive material of the Li-6 detector captures a neutron and an alpha particle is formed, see equation (3.2). This particle induces the signal on the detector. This signal is compared to a glow curve which is generated by an

irradiation directly with alpha particles.

For this purpose, two glow curves are displayed in Figure 6.4, one in the time regime (left) and one as function of the temperature (right). The alpha induced glow curve was measured after an irradiation ($t = 433$ s corresponds to approx. $D = 3$ mGy) of an MT-N detector with the alpha irradiator, whereas the neutron irradiation of a Li-6 detector was performed in the $^{241}\text{AmBe}$ reference field of the PTB with $H_{p,n}(10) = 3$ mSv. In Chapter 3 it was shown that the two detector types have a very similar responses to irradiations with photons.

In the left plot, the two curves are shifted relative to each other, because the time-dependent heat transfer of the two detectors is different. The peaks 3–7 are visible for both pre-heated glow curves. In addition, a statement about the total integral after background subtraction can be made. In these two cases the signals correspond to

$$N_{\alpha} = 8810 \pm 440,$$

$$N_{\mathbf{n}} = 9020 \pm 450$$

photon counts. The alpha particle irradiation results in 2% less counts than the neutron irradiation which is compatible with each other within the 1σ uncertainty interval.

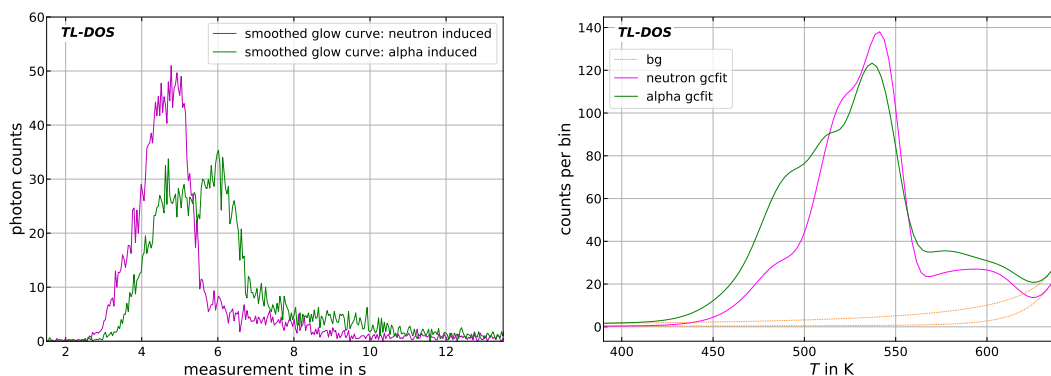


Figure 6.4: Pre-heated glow curves after a) an alpha irradiation with $t = 433$ s and b) a neutron irradiation with $H_{p,n}(10) = 3$ mSv in the $^{241}\text{AmBe}$ reference field. Both measured at 653 K. Left: presented in the time regime as smoothed curves. Right: presented in the temperature regime as fitted curve. Gcfit means the glow curvefit.

If the glow curves are compared to each other in the temperature regime, so that the heat transfer of the detector does not matter, different behavior of the peaks is found. The neutron induced glow curve (magenta curve in Figure 6.4 right) results in a smaller peak 3 integral, but in a higher integral of peak 4 and especially in a higher peak 5 integral in contrast to the alpha induced glow curve, green curve in the figure. Peaks 6 and 7 are similarly pronounced for both glow curves, only the measurement background is higher for the alpha induced signal. The integrals of the high-LET peaks result almost in the

same number of counts for both measurements. A possible reason for the higher peak 4 integral could be the significantly higher local ionization density of neutron irradiation. Overall, the differences between alpha induced signals and neutron induced signals are small.

Based on the previous discussions, alpha irradiations are performed for first investigations of the high-LET peaks because they can be assumed to be similar to neutron induced glow curves in first approximation and handle much easier and faster.

6.1.3 Post-irradiation fading of alpha induced glow curves

The post-irradiation fading (see Section 3.1.3) behaviour of the TL-DOS system has already been investigated in detail for photon irradiation [34, 80]. In this chapter, the fading effect after high-LET irradiations is discussed with a special focus on alpha irradiations and the high-LET peaks.

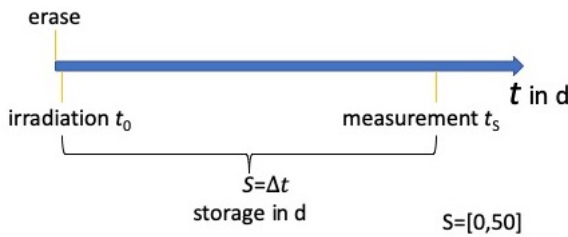


Figure 6.5: Irradiation procedure for fading investigations of alpha induced signal. The storage time S is defined as time between the irradiation and the measurement.

With the alpha irradiator 132 whole-body TL-DOS detectors (MT-N) are irradiated for $t_\alpha = 600$ s. After a storage time $S = \Delta t$ between 0 d and 50 d (see Figure 6.5), twelve detectors are measured at 653 K without pre-heating. A total of eleven different values are chosen for S . The time between the erase and the irradiation of a detector is constant for all measurements.

The results are presented as mean value and their standard error of mean in Figure 6.6. The natural background radiation is not taken into account because the irradiated dose is high enough. In Ref. [34] it was shown that for sufficiently high doses (> 4 mSv), the natural background can be neglected in a first assumption. For further detailed analysis of the post-irradiation fading effect, the natural background has to be included. In addition to the measured alpha fading curve, the TL-DOS photon post-irradiation fading curve measured and explained in Ref. [34] is shown in Figure 6.6. Both curves are fitted with the same function

$$y = A \cdot \exp(-B \cdot x) + (1 - A) \cdot \exp(-C \cdot x) \quad (6.1)$$

dependent to the storage time, but different irradiation types (photons and alpha particles) result in various fit parameters for the function.

The fading effect after an alpha irradiation is much stronger than the fading effect after

a photon irradiation. After 30 days the alpha signal is reduced to 70% compared to t_0 and the photon signal to 75% compared to t_0 .

A similar fading behavior has already been described in [81] for the LiF:Mg,Ti material TLD 100. While in Ref. [81] and also in this thesis a signal reduction of 25% was found for gamma irradiated detectors after 30 days, this behavior was confirmed with (-27%) in Ref. [82] as well. After alpha irradiations a strong reduction (35.5%) is observed in Ref. [81], just as in the measurement presented here.

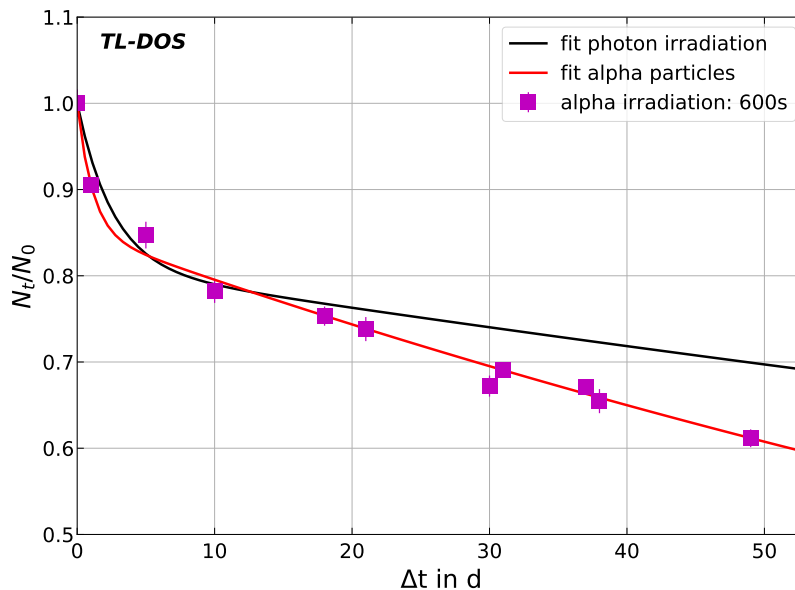


Figure 6.6: Averaged relative number of signal photons as a function of the fading time. The standard errors of mean are mostly smaller than the marker size. The data is adapted with equation (6.1). In black is illustrated a previously measured photon fading curve adapted from Ref. [34].

The more pronounced the fading effect, the more important is the pre-heating step before a measurement in routine dosimetry. In Ref. [78] it has already been shown that the TL-DOS pre-heating process eliminates fading effects for alpha irradiations, too.

In the future the fading behavior should be studied in detail for neutron induced glow curves. The description of the fading effect of signal generated by high-LET radiation helps for a better understanding of other measurements and subsequent results. It may be possible to obtain even more information from the high-LET peaks, e.g. about the irradiation scenario, due to the enhanced fading effect.

In Ref [81] it is claimed that there are further factors influencing the fading effect in addition to the LET dependence, which is assumed in the reference. One indication for additional effects impacting the fading behaviour is the observed difference in the fading time-constants between alpha and neutron irradiated detectors [36]. These effects cannot

be explained yet due to the high complexity of the material LiF:Mg,Ti [81]. Further investigations regarding the post-irradiation fading are out of scope for this thesis. In routine dosimetry and hence in this thesis the detectors of the neutron dosimeter are pre-heated before a measurement to reduce the impact of fading.

6.2 Energy dependence of individual glow peaks

In Chapter 4 the strong energy dependence of the TL-DOS neutron dosimeter system was discussed. If this dependence could be better understood or compensated, the uncertainty of the dose estimation could be reduced.

The peaks of neutron induced glow curves are examined individually in the following. Their energy dependence is investigated, as this could be used for the evaluation of dosimeters to alleviate or solve the challenge of energy dependence (see Chapter 2.5).

Therefore, the glow curves recorded in the neutron reference fields (see Chapter 4) with the albedo Li-6 detectors (Li6-A) are deconvoluted into their individual peaks and evaluated separately. All irradiations were performed with the same dose.

In Figure 6.7 the integrals of the peaks N_i are normalized to the integral resulting from irradiation with $\bar{E}_n = 0.099$ MeV neutrons and plotted versus the mean neutron energy \bar{E}_n . Additionally a function

$$\frac{N_i(\bar{E}_n)}{\bar{N}_i(\bar{E}_n = 0.099 \text{ MeV})} = \frac{a}{\bar{E}_n + b} + c \quad (6.2)$$

is fitted to the results to describe the data. For example one of these plots is shown in the figure below on the left side for the combination of peak 6 and peak 7. As usual, the high-LET peaks are considered together. The peak integrals decrease with an increasing energy for all peaks. The result matches the expectations from the cross sections.

On the right side of the figure, the results of the three fit parameters (a,b,c) are shown together with their uncertainty for the individual peaks. To guide the eye, the mean is also drawn as trend line respectively. Higher uncertainties are found for the parameters of peak 3 and peak 4 than for the other two. This is due to the fact that the detectors are pre-heated before a measurement, which causes different amounts of signal from peak 3 to be erased. The large uncertainty on the parameters for peak 4 results from the glow curve fit, which is most unreliable for peak 4. Therefore, in Ref. [34] peak 4 is always considered together with peak 5.

The values of the individual fit parameters are the same for all peaks within their uncertainty, showing that the energy dependence of each individual peak is the same for all peaks and the behavior of the high-LET peaks is described by function (6.2) as well.

By taking these two peaks into account, more signal of a glow curve is measured that is subject to the same energy dependence.

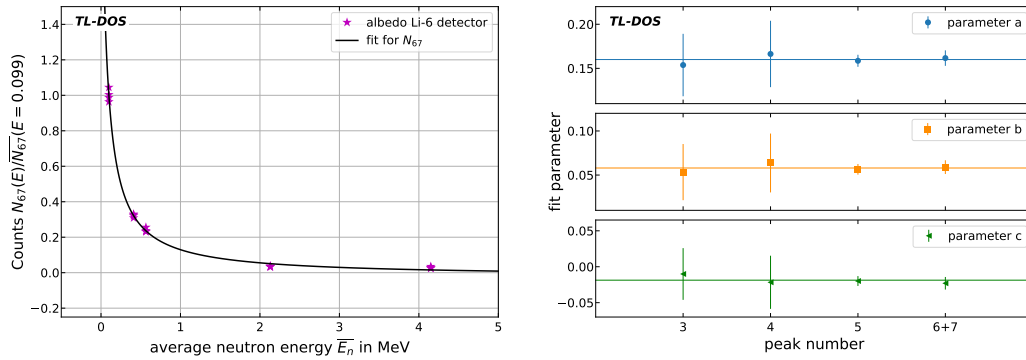


Figure 6.7: Left: Normalized signal of peaks 6+7 (N_{67}) plotted versus the averaged energy of the PTB reference neutron fields. The albedo Li-6 detectors are pre-heated and measured at 653 K, successively. Right: Resulting fit parameters of function (6.2) for different peaks and their mean as trend line.

6.3 Determination of type of irradiation

When estimating a neutron dose with an albedo dosimeter a false positive error (first order) can occur, so that a photon dose is wrongly identified as a neutron induced signal. It occurs especially, if the Li-7 detector is significant less sensitive than the Li-6 detector to photons. With the TL-DOS dosimeter it is avoided by checking the authenticity of a neutron dose. For this purpose, a method is developed to determine with which type of particle the detectors were irradiated after a single irradiation. Whether a high-LET irradiation like a neutron or alpha irradiation was performed or not, is the simplest statement which can be made. If the high-LET peaks of a glow curve are visible through the readout, the detectors have been irradiated with neutrons or heavy charged particles (like alpha particles) or a very high dose (see Chapter 5.5). Depending on the type of irradiation, the individual peaks and the high temperature region are more or less visible, which can be a benefit for different analysis, e.g. see Ref. [34, 83].

Peak integral ratios vary depending on the radiation type that induced the glow curve. To analyze different peak ratios, data of irradiated TL-DOS detectors (Li-6) are considered. Li-6 detectors are chosen because on them a signal is also induced by neutrons, unlike Li-7 detectors. Therefore measurements after irradiation with:

- alpha particle with the MPA NRW ^{241}Am irradiator,
- photons with the ^{137}Cs facility of the MPA NRW,
- neutrons in different reference fields of the PTB

are used. The irradiations are performed with various doses. All glow curves are fitted with GCana.py and various ratios of the peak integrals RN are formed. In particular, the ratio RN_{45} of peaks 4 and 5 and the ratio RN_{567} are calculated:

$$RN_{45} = \frac{N_4}{N_5}, \quad (6.3)$$

$$RN_{567} = \frac{N_5}{N_6 + N_7}. \quad (6.4)$$

Where N_5 is the net integral of the 5th peak, for example. For the ratios only the stable peaks, which are not strongly sensitive to the fading effects, are used. The consideration of exactly these two ratios is based on the observations of different glow curve shapes in Sections 5.5 and 6.1.2. Both ratios are displayed for different irradiation types in Figure 6.8 showing that the values of the ratios are characteristic for the particle type of irradiation.

Peak ratios change significantly. A photon irradiation can be distinguished from a high-LET irradiation like alphas or neutron by the ratio RN_{567} unambiguously, see Figure 6.8 (left). For high-LET irradiations the ratio is 2–3 and the ratio is larger than 10 for photon irradiations with high doses.

The ratio RN_{45} is proficient for distinguishing between neutron and alpha irradiations. It is significantly higher for alpha irradiations than for neutrons, shown in the figure (right).

Peak ratios can be used to distinguish the type of the three considered particles with which the detectors were irradiated. Thus, a calculated neutron dose can be classified as a real neutron induced signal (correct neutron dose) or as a photon induced signal (false neutron dose).

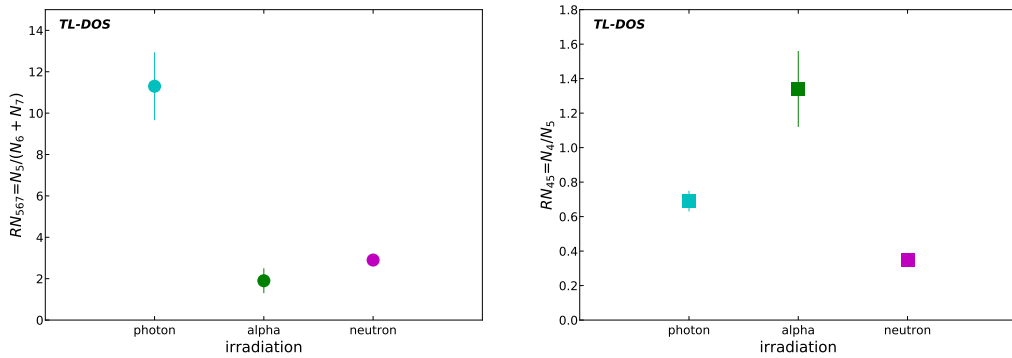


Figure 6.8: Left: Average ratio RN_{567} and its standard error of mean for photon, alpha and neutron irradiations. Right: Average ratio RN_{45} for photon, alpha, neutron irradiation. Measured at 653 K with a Li-6 TL-DOS detector chip after a pre-heating step.

If the ratios are also dependent on the particle energy or the irradiated dose, it would be impractical and undesirable. In order to exclude an energy dependence of the ratio, the measurements of all neutron reference fields and the irradiations with the alpha irradiator with different distances to the source are considered separately. Additionally, the alpha irradiations are performed with various doses from 0.9 mGy up to 5 mGy. Figure 6.9 shows all results for various neutron and alpha irradiation.

The same ratio RN_{45} is found to be about 0.34 for neutron irradiations with very different energy spectra. Also alpha irradiations results in a similar RN_{567} ratio which is characteristic for high-LET irradiations like these. Considering the uncertainties the values for this ratio range from 1.4 up to 2.2.

The two plots in Figure 6.9 are shown as examples. Considering the plots the other way around, similar results are found. Just as same values are found for the ratio RN_{567} for different neutron energies, the ratio RN_{45} also results in equal values for all tested alpha energies and alpha induced doses. Furthermore, the ratios of photon induced glow curves are also measured for different photon doses. Since no dependence of the dose or the energy could be confirmed the ratios depend solely on the particle type of irradiation, they can be used for differentiate between the irradiation types.

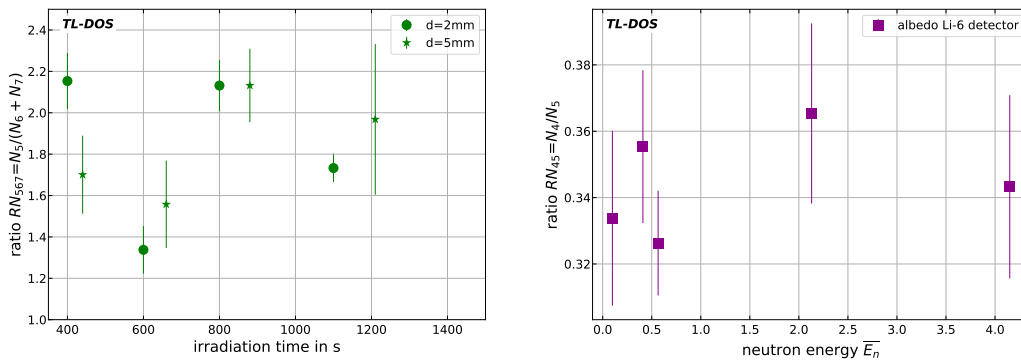


Figure 6.9: Left: Average ratio RN_{567} and its standard error of mean determined for different alpha irradiation times with different distances and energies. Right: Averaged ratio RN_{45} and standard error of mean determined for different neutron energies in the reference fields of the PTB.

It is possible to distinguish from the glow curve, whether a detector has been irradiated with photons, neutrons or alpha particles. In Ref. [83] the separation of beta and gamma irradiations was studied using machine learning. This method could also highlight even more significant differences here.

6.4 Separation of alpha and gamma induced signals after mixed irradiations

In order to meet the dosimeter challenge of mixed fields (Chapter 2.5), the albedo method (two detectors) is currently used for neutron dosimeters. The different induced doses are measured by two detectors, those results subtracted from each other, see Chapter 2.6. The effective cross section (Figure 3.4) shows that this only works to a limited extent for high energies. Additionally, more detectors result in a larger badge and more effort in routine measurements.

The biological effectiveness and consequences of radiation are higher if more energy is applied to a human body. This is described numerically by the parameter LET [38]. Since high-LET irradiation like alpha particles or neutrons is particularly harmful to humans, it is important to separate and to know the different doses after mixed irradiation precisely.

Therefore, the following chapter introduces the development of a signal separation using for alpha gamma mixed irradiations. It is a proof-of-principle study to develop an analysis to separate high and low LET induced signal.

Depending on the ionisation density, differences in the shape of glow curves have been observed for several years [84, 85]. The TL-DOS system, allowing the readout of deeper traps, offers the possibility to gain more information about the irradiation from the glow curve as already discussed in the previous chapter. In order to estimate the dose as accurately as possible, investigations with various mixed irradiation fields are performed.

6.4.1 Dose linearity of mixed irradiations

To simulate mixed fields, TL-DOS detectors are irradiated with alpha particles and photons successively. The whole body detectors using Li-N as sensitive material are used as the alpha irradiator is mechanically optimized for the size (17 mm) of these detectors.

First, an alpha irradiation is performed, where the signal of the alpha irradiations is calibrated to the $H_x = 5$ mSv signal of irradiations with ^{137}Cs to specify the alpha dose D_α . Second, the detectors are irradiated with a dose D_γ between 0 mGy and 20 mGy using the ^{137}Cs facility of the MPA NRW.

In total, 20 detectors are irradiated with different scenarios and 5–10 measurements are performed per combination. The signals induced on a detector are added to a total dose D_t :

$$D_t = D_\alpha + D_\gamma. \quad (6.5)$$

All total doses are in the personal dosimetry range of a few mGy, where the alpha dose is normalized to a photon dose. In the next paragraph it is checked if the detected signal also adds up. For single-irradiations (with alpha particles or photons) the signal increases linearly with the dose, see Figure 6.2.

In Figure 6.10 photon counts of mixed field measurements are plotted as average with their standard error mean to the total dose. Each total dose represents a set of measurements with varying combinations of alpha doses D_α and gamma doses D_γ . The four different total doses D_t are described by a linear function:

$$N_{\text{net}} = m \cdot D_t + b. \quad (6.6)$$

A linear relationship for the signal and the dose is affirmed for the mixed irradiations (alpha+gamma) in the dosimetry dose range, too. Additionally, the relative difference between the fit and the measurement is illustrated in the figure (lower part). No systematic deviation is found because there are both positive and negative deviations. In addition, these are smaller than +3%, so the data is well described by the linear function.

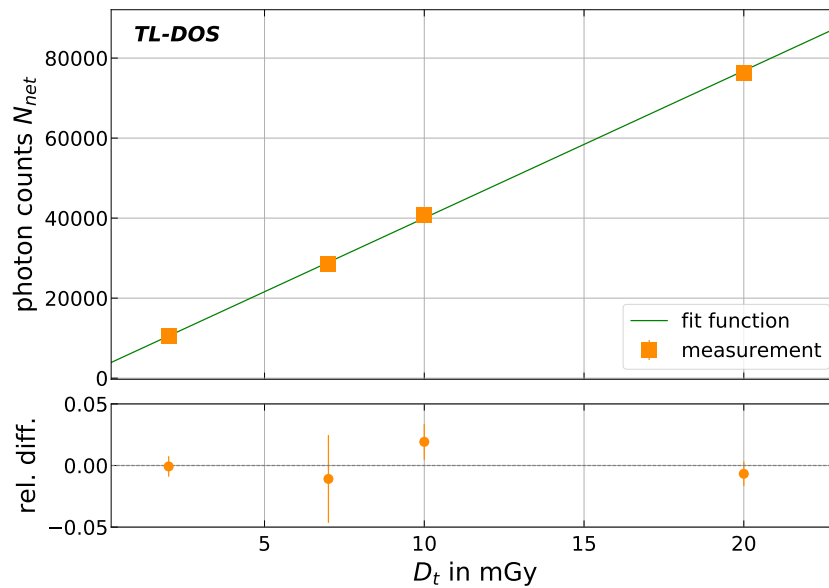


Figure 6.10: Calibration curve of the detectors, irradiated with ^{137}Cs and ^{241}Am : linear relationship between the measured counts and the total dose D_t . Each point represents a set of measurements with constant D_t , but varying alpha D_α and gamma doses D_γ .

6.4.2 Analysis to separate the alpha and gamma induced signal

After read out the TL-DOS detectors at 653 K with a pre-heating step all glow curves are deconvoluted by GCana.py. The glow curve is split into peaks 3–7 because also the

deeper traps are populated during irradiation with alpha particles. Following, the individual peaks of a glow curve are considered separately. Figure 6.11 shows such a glow curve with its peaks 3–7 after irradiation with $D_\alpha = 3.5$ mGy and $D_\gamma = 0.5$ mGy. For measurements in personal dosimetry the yellow area in the figure is the signal induced through both irradiations, whereas the red area is only induced through high-LET radiation like alpha particles. The background is marked as gray area in the figure.

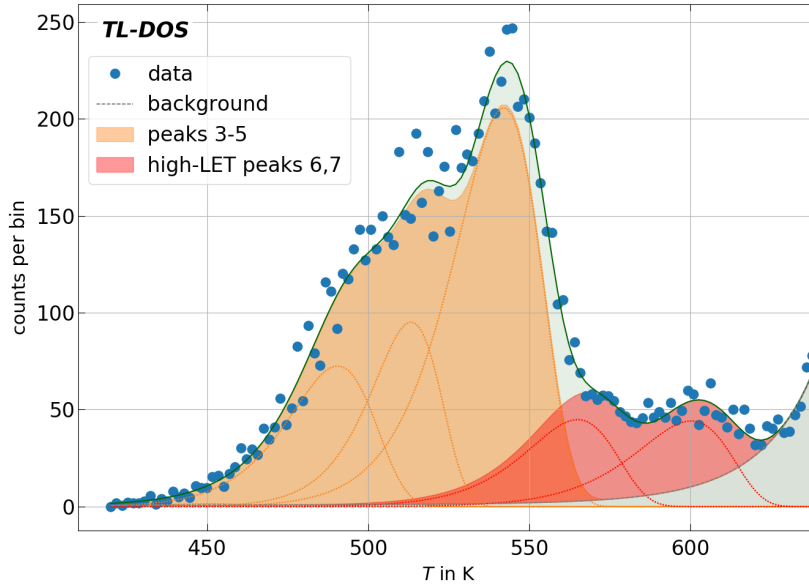


Figure 6.11: A glow curve with its individual peaks 3–7 is visible. It is recorded after irradiate a thermoluminescence dosimeter system (TL-DOS) detector with ^{241}Am and ^{137}Cs . $D_\alpha = 3.5$ mGy, $D_\gamma = 0.5$ mGy, $D_t = 4.0$ mGy.

The separation analysis is based on the evaluation of the high-LET peaks. It is possible to form the ratio RN_{567} of peak 5 and the high-LET peaks (equation (6.4)) to estimate the alpha and gamma induced signal individually. The high-LET peaks are considered together because their sum is the total signal which is only generated by alpha particles and not by gammas in the irradiation scenario used. Furthermore, peak 6 and peak 7 are strongly overlapping and difficult to separate.

For each irradiation the gamma fraction j is calculated by equation (6.7) to assess the radiation exposure as precisely as possible.

$$j = \frac{D_\gamma}{(D_\alpha + D_\gamma)} \quad (6.7)$$

Figure 6.12 shows the averaged ratios RN_{567} with their standard error of mean as a function of the gamma fraction j . A relationship between the two quantities is visible. The higher the gamma fraction, the higher the ratio RN_{567} . If j is zero, the ratio is

approximately two which is in a very good agreement with the results in Chapter 6.3. At this point the integral of the high-LET peaks are half the counts of the peak 5 integral.

Due to the fact that peaks 6 and 7 are mainly caused by the high-LET irradiation in the considered dose range and the traps of peak 5 are filled by both high and low-LET irradiations, the ratio RN_{567} is proportional to the high-LET fraction of the irradiation. As a consequence, the data in Figure 6.12 are described by a modified $\frac{1}{x}$ function.

A parametrization

$$RN_{567} = \frac{a}{j - b} + c \quad (6.8)$$

is found which describes the measurements well. This parametrization curve and the 1σ errorband are also shown in the figure. In addition the differences of the curve to the measurement are illustrated. All values fluctuate close to zero and the reduced χ^2 results in 0.4 for the fit, which confirms that the measurements with their uncertainties are described by the parametrization to a good degree.

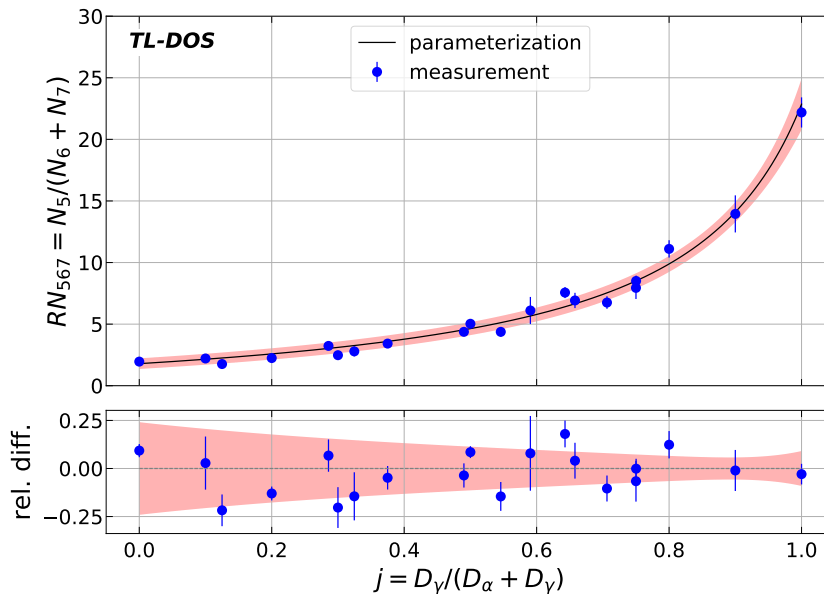


Figure 6.12: Measurements and parametrization for the gamma fraction of mixed irradiations with ^{241}Am and ^{137}Cs and different doses; in the bottom part the relative deviation of the measurement to the fit.

In order to use the presented analysis to separate the alpha and gamma induced signal from one glow curve, a calculation method is defined. The method is shown in the schematic diagram in Figure 6.13. The relationships between the individual parameters are described more precisely in the transparent boxes. Linear and parameterization mean the function (6.6) and (6.8).

After a detector has been measured, the glow curve is deconvoluted to determine the ratio RN_{567} . The gamma fraction j is determined via the parameterization, yellow way. In addition, the total dose is calculated from the total counts by a linear calibration (orange way).

Afterwards, the gamma dose D_γ results by multiplying the two quantities. In turn, this is subtracted from the total dose D_t (equation (6.5)) to obtain the alpha dose D_α .

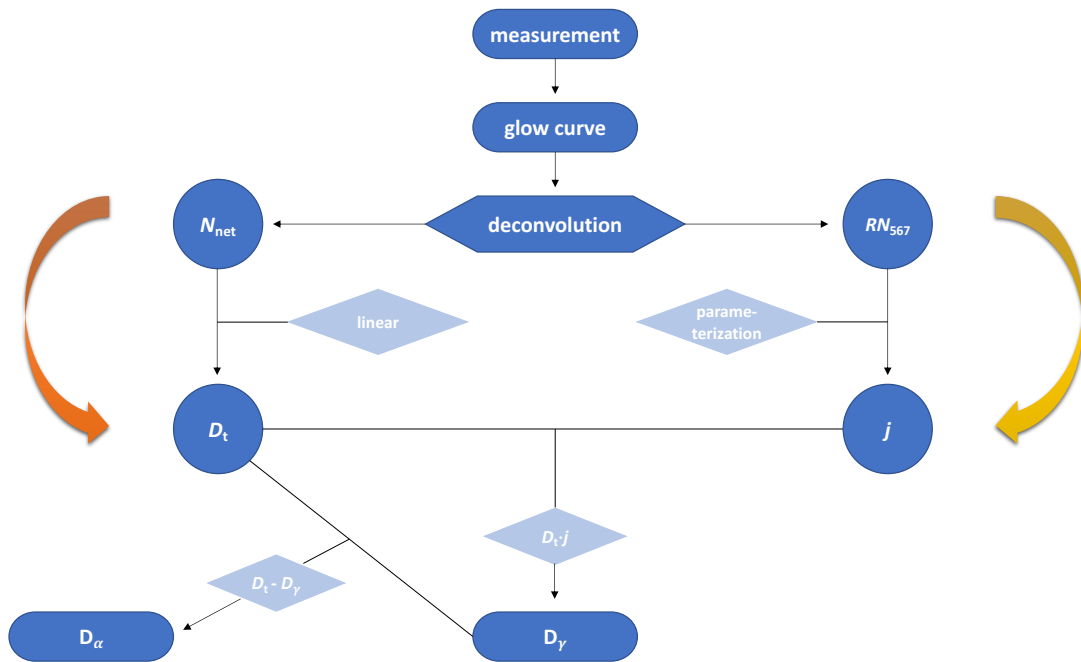


Figure 6.13: Schematic of the dose calculation method to separate the alpha and gamma dose of only one measured glow curve after mixed irradiation. The calculation methods between the individual parameters are shown.

6.4.3 Robustness of ratio RN_{567} and uncertainties on the estimator

To define the parameterization equation (6.8) for RN_{567} the detectors were irradiated with different total doses and different dose combinations. The standard deviation of the ratio RN_{567} is constant for all irradiated doses in the dose range used, so that no dose dependence is found for the uncertainty of the ratio.

Additionally, the robustness of the ratio RN_{567} is tested by a cross validation. Therefore, the data set is split in two sets, set Y and set L. First, the free parameters of the fit function, equation (6.8), are determined with the data set Y. Second, the deviation between the fit function and the L data set is calculated. This procedure is repeated for different Y-L splits and a mean deviation is determined. Here the absolute mean deviation between

the calculated ratio and the measured ratio RN_{567} is 0.8 ± 0.1 . The result affirms that the data are well described by the determined parameterization curve for the irradiation scenarios tested.

In the next paragraphs the uncertainty on the estimation of the gamma fraction is discussed. For this purpose three components (σ_{stat} , σ_{func} , σ_{devi}) of the total uncertainty are considered separately.

One component is the statistical uncertainty σ_{stat} , which is calculated by the standard deviation of the measured ratio RN_{567} . In the presented dose range, the standard deviation is 5% for calibrated detectors. This value was observed in previous measurements, too. For example, the dose estimator scatters at most 4–5% in the range from 0.5 mGy to 20 mGy. Since all detectors are produced at the MPA NRW with a high quality standard, they are well known and have an uniform response.

For the standard deviation = 5%, the uncertainty σ_{stat} is determined for each measured j and afterwards the data is fitted by a quadratic function. The resulting uncertainty σ_{stat} is marked relatively as dotted curve in Figure 6.14.

Another component is the function uncertainty σ_{func} . It is calculated by uncertainty propagation of the three fit parameter of the parameterization curve and marked as dashed line in the figure.

The systematic deviation σ_{devi} is the last component of the trio. Therefore, the absolute deviation of the irradiated gamma fraction j_{irrad} and the estimated gamma fraction j_{fit} (calculated with equation (6.8)) is determined. The results are plotted against the irradiated gamma fraction (j_{irrad}) and the absolute deviation is found as constant. This constant is relatively plotted in the Figure 6.14.

The quadratic sum of all three is used to estimate the total relative uncertainty σ_{tot} , which is shown in Figure 6.14.

The smaller the gamma fraction j is, the higher is the relative uncertainty on the estimation of j . In the case $j \leq 0.45$, the function uncertainty σ_{func} is the dominant one. Subsequently, the statistical uncertainty predominates compared to the other both, that could be further reduced by calibration or newer detectors because the detector production is constantly being improved.

If the gamma fraction of the total irradiation is at least 40%, the relative uncertainty on j is less than 10%. Usually, it is the case in personal dosimetry because in reality, the natural background radiation is a dominant part of the signal induced on the detector. The worldwide average natural radiation dose to humans is about 2.4 mSv per year [86], so that always a gamma signal is induced on a detector.

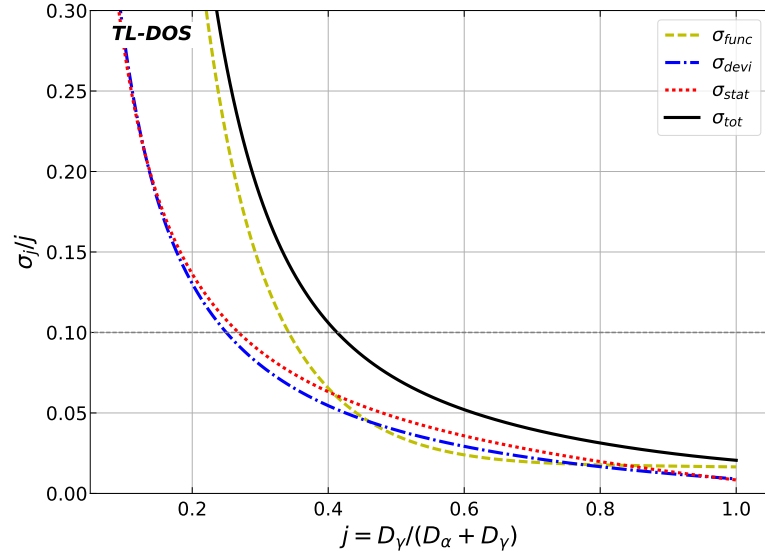


Figure 6.14: Relativ total uncertainty σ_{tot} of the gamma fraction j and the individual components of the uncertainty (function σ_{func} , statistical σ_{stat} , systematic σ_{devi}).

6.4.4 Validation of the estimator

The newly developed analysis is tested and validated by further measurements. Again 20 TL-DOS detectors are irradiated with ^{137}Cs and ^{241}Am . This time the photon irradiation is performed before the alpha irradiation to exclude possible effects and dependencies of the irradiation order. Again, all total doses are in the order of a few millisievert and one irradiation combination is measured five times.

The ratio RN_{567} and the gamma fraction j are calculated by equations (6.4) and (6.7) for these measurements. The resulting data are compared to the parameterization defined in Section 6.4.2.

Figure 6.15 shows the measured ratios as average with their standard error of mean and the parameterization (equation (6.8)) with its uncertainty found in Section 6.4.2. All data are in good agreement with the function and its uncertainty.

Additionally, for all glow curves the gamma fraction j_{est} is calculated by the combination of the measured ratio RN_{567} and the parameterization (equation (6.8)). The deviation between this estimated gamma fraction j_{est} and the irradiated one j is also shown graphically as relative difference in the figure.

Since the gamma fraction is overestimated for some ratios and underestimated for some others, for the difference no dependence on the ratio is found.

The relative difference for these gamma fractions (Figure 6.15) and the total uncertainty on j (Figure 6.14) are in a good agreement for the four gamma fractions, e.g. for $j = 0.29$ the deviation is 20% and the uncertainty is expected as $\pm 20\%$ according to Figure 6.14.

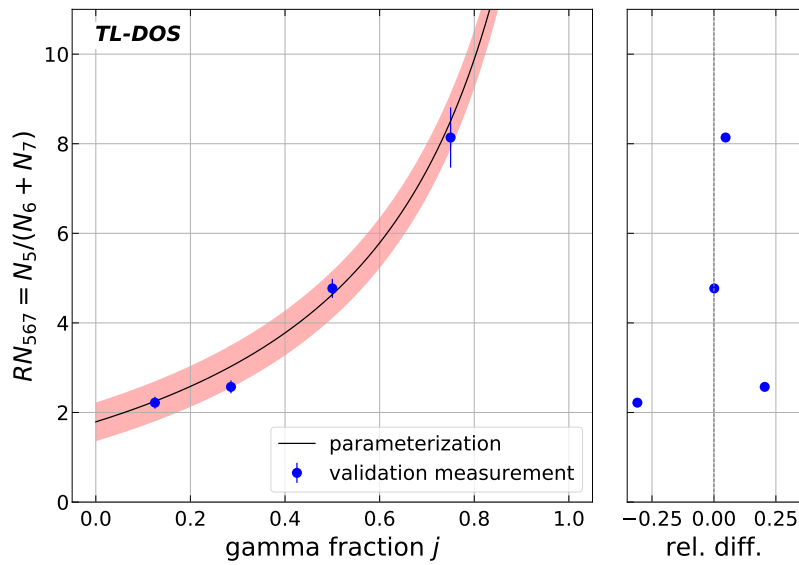


Figure 6.15: Classification of the new measurements in the calibration curve, which is fitted in Figure 6.12, and the deviations of the measure points to the calibration curve.

If the same function (equation (6.8)), as used to find the parameterization in Section 6.4.2, is fitted through these four measured values, the fit parameters (a,b,c) result in equal values, respectively.

Based on the facts that the parameters are compatible with each other and the differences (Figure 6.15) are in an agreement with the uncertainties, it is confirmed that the order of the two irradiations does not matter. In addition, the analysis has been verified by these measurements.

6.5 Separation of the neutron and the photon dose after mixed irradiations

The newly developed analysis (Chapter 6.4) for the separation of alpha and gamma induced signal is based on the evaluation of the high temperature peaks. It is likely that it is possible to transfer the analysis to other irradiation combinations which includes one irradiation with high-LET particles and also one irradiation with low-LET particles.

As described in Chapter 2.5, neutron dosimeters always face the challenge of mixed irradiation fields. Neutron+photon dose separation by only one glow curve would be a great alternative to the common two-detector-method presented in Chapter 2.6. To test the new separation analysis in neutron dosimetry, measurements in neutron+photon mixed fields are performed with the TL-DOS neutron dosimeter.

6.5.1 Measurement setup and performance

First, 16 TL-DOS albedo badges, described in Chapter 3.4, are irradiated with scattered neutron radiation at the WPE to perform mixed irradiations. There, the neutron field is characterized by field calibrations and the neutron correction factor k is well known at point e (Fig. 4.20). The k -factor is determined for this point in Section 4.4.5. Four badges are mounted simultaneously in front of a water slab phantom as shown in Figure 2.4. All dosimeters are irradiated with the same set-up parameters (proton beam energy $E = 172$ MeV, modulated beam: R20M10, etc.) described in Section 4.4.5 to induce the same dose to each. Four of the 16 badges are used to calculate the induced neutron equivalent dose $H_{p,n}(10)$ by using the k factor determined as described in Section 4.4.5 for the WPE. The dose results in

$$H_{p,n} = (0.91 \pm 0.08) \text{ mSv.}$$

Second, twelve dosimeters remained are irradiated with photon doses $H_{p,\gamma}(10)$ in the range between 0 mSv and 4 mSv with the ^{137}Cs facility. Again, four TL-DOS albedo dosimeters are fixed at the water phantom, respectively. So measurements with four different neutron+photon irradiation combinations are performed with four dosimeters each. The total $H_p(10)$ dose sum up to

$$H_t = H_p(10) = H_{p,n}(10) + H_{p\gamma}(10). \quad (6.9)$$

6.5.2 Analysis of neutron+photon mixed irradiations

According to the DIN 6802 the neutron dose is usually calculated using the Li6-A detector. Therefore, this detector - of the total four chips in a badge - is considered for the analysis that follows. The analysis is performed as described in Section 6.4.2.

The measured integral of the total glow curve is plotted versus the total dose irradiated. The mean values and the corresponding standard errors of mean are shown in the top part of Figure 6.17 (left). A linear calibration function is fitted to the measured values. Furthermore, the deviation of the fit to measurement is illustrated in the bottom part of the figure. As for alpha+gamma irradiations, a linear correlation between the dose and the signal can also be confirmed for neutron+photon mixed irradiations.

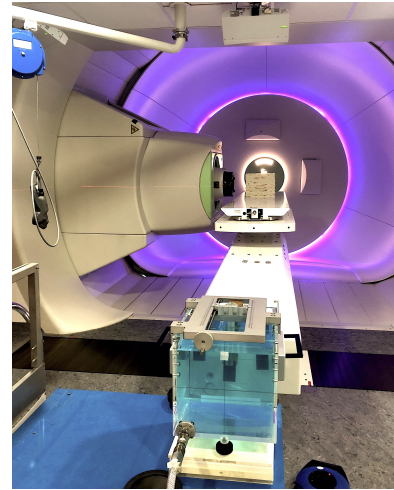


Figure 6.16: Measurement setup at the WPE to induce a neutron signal on dosimeters.

In the next step, the gamma fraction j and the ratio RN_{567} are determined for all Li-6 albedo detectors by equation (6.7) and (6.8).

In Figure 6.17 (right) the results of the measured ratios are presented as mean value and corresponding standard error of mean. A function as described in equation (6.8) is fitted to the data. The resulting parameterization is shown as red line in the figure and its uncertainty is plotted as well. The ratio increases with a larger gamma fraction of the total irradiation as expected because a neutron irradiation results in a lower ratio RN_{567} than a photon irradiation, see Chapter 6.3. The uncertainty of the parameterization is especially large for low gamma fractions ($\leq 20\%$) and high gamma fractions ($\geq 85\%$). In the future, even more data of these mixed fields should be recorded in order to improve the fit and reduce uncertainties.

As a check, the deviation of the gamma fraction, estimated with the curve, to the irradiated fraction of all individual measured values is calculated. The mean value of all deviations is determined and it results in a mean deviation of the gamma fraction of 3.4%.

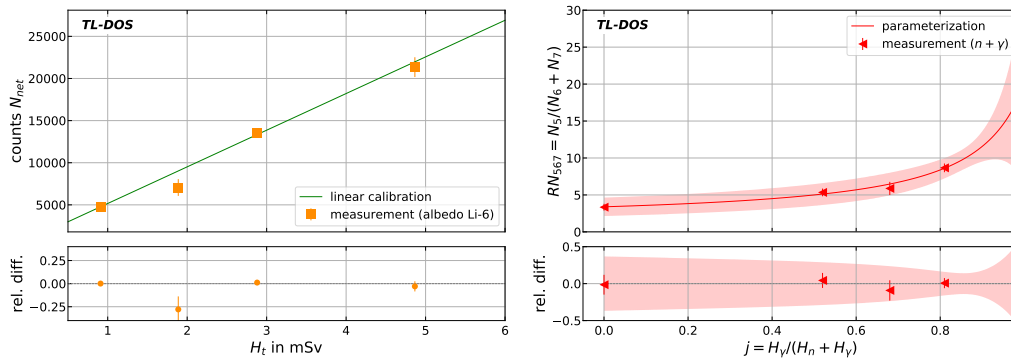


Figure 6.17: Left: Signal-to-dose-linearity of the Li-6 albedo detectors of the TL-DOS albedo dosimeter, irradiated with ^{137}Cs and neutrons: linear relationship between the measured counts and the total dose H_t . Each point represents a set of four measurements. All points are irradiated with a constant neutron dose and varying photon doses. Right: Measurements of different total doses and parameterization for the gamma fraction of mixed irradiations with neutrons and photons (^{137}Cs). All detectors are irradiated with the same neutron doses. Bottom: The relative deviation of the measurement to the fit.

6.5.3 Comparison of neutron+photon to alpha+gamma mixed fields separation

To compare the neutron+photon results with the results found for alpha+gamma mixed data, both are plotted together with their respective parameterizations in Figure 6.18. In principle, both have the same course.

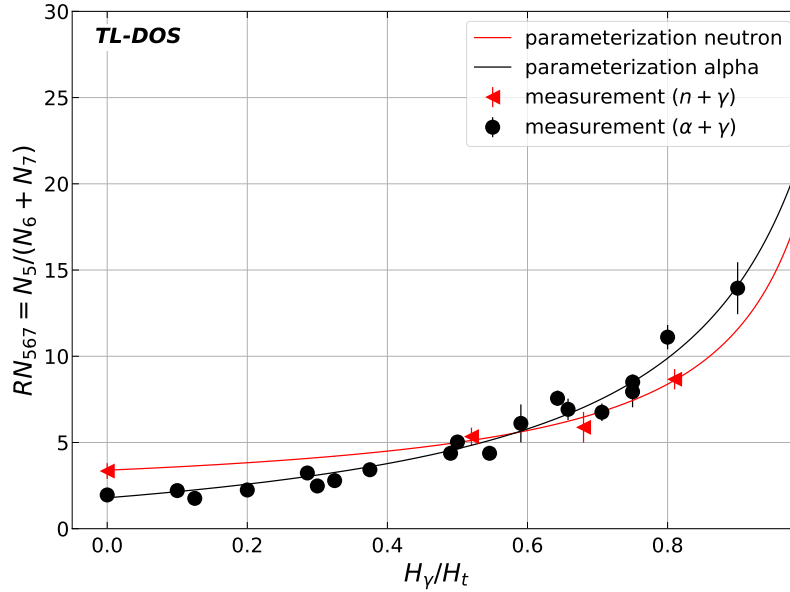


Figure 6.18: Measurements and parameterization for the gamma fraction of alpha+gamma mixed irradiations with ^{241}Am and ^{137}Cs and for neutron + gamma mixed irradiations with scattered neutrons and ^{137}Cs .

As expected after investigations in Chapter 6.4, it is observed that the curves result at $j = 0$ in Figure 6.18 into different ratios. According to Figure 6.8 the ratio is higher for neutron induced glow curves. But all parameterization should result in the same value for $j = 1$ (in Figure 6.18) because at this point only a gamma dose is measured and in each case it is performed with the same ^{137}Cs facility. The difference observed here is due to the fact that the two measurements were performed with slightly different dosimeter types. The one for alpha+gamma separation is performed with the TL-DOS whole body detectors (material: MT-N) without any badge or phantom and the other used TL-DOS Li-6 (MT-6) detectors in the albedo badge on a water phantom. Additionally, too few data points are available for the mixed irradiation with neutrons, especially in the range between $j = 0.8$ and $j = 1$. This may result in a shift of the parameterization curve especially for $j = 1$. Table 6.1 shows that the fit parameters for neutron+photon mixed irradiations have significantly higher uncertainties than those of alpha+gamma mixed irradiations due to the low statistics. It can be recognized that the same method developed for alpha+gamma mixed fields works and can be transferred to the neutron+photon mixed fields.

Table 6.1: Fit parameters of two parameterizations.

irradiation	a	b	c
$\alpha + \gamma$	4.61 ± 0.58	1.18 ± 0.03	2.10 ± 0.45
$n + \gamma$	2.23 ± 1.55	1.12 ± 0.17	3.70 ± 1.34

In summary, the measurements (neutron+photon irradiation) demonstrate that a description of the ratio depending on the gamma fraction by equation (6.8) is possible and the separation of the doses works by using glow curve deconvolution.

The proof of principle study is successfully completed. These results can be used to adapt and update the evaluation procedure of the TL-DOS neutron dosimeter. The analysis represents a possibility to meet the challenge of mixed fields (Chapter 2.5) as it is a good alternative to separating the dose via two detectors. As shown in Figure 3.4 the current separation via Li-6 and Li-7 shows especially for high energies its limits.

In addition, this separation offers new possibilities in the design of the neutron dosimeter badge and the evaluation analysis. The number of detectors in the badge can be reduced because the Li-7 detectors are no longer necessary. This would mean that a TL-DOS neutron badge would be smaller, which means a higher wearing comfort. Or the detectors could become larger allowing more sensitive material to be used and resulting in a higher measurement signal. These are new prospects in neutron dosimetry.

Chapter 7

Neutron energy dependence of the TL-DOS dosimeter

The TL-DOS system offers the possibility to extract some additional information from the glow curve, e.g. the irradiation time as already presented in Ref. [34]. Especially the signal gain of neutron induced glow curves suggests that even more information about the irradiation can be found.

The first challenge for neutron dosimeters, as formulated in Chapter 2.5, the separation of mixed fields, has been discussed in Chapter 6. Compared to the current method with two detectors (two glow curves) the new analysis provides a good alternative for signal separation via one glow curve.

The more information are obtained from a glow curve, the more precise is the dose estimation. For this reason, the second challenge, the energy dependence, is examined in more detail in the following sections. Therefore, the correction factor k , which is necessary for the estimation of the personal neutron dose $H_{p,n}(10)$ with an albedo dosimeter, is considered and the current estimation via Z , as described in DIN 6802, is critically reviewed. Subsequently, other approaches for determining k are presented, before the proposed analyses are compared.

7.1 Energy dependence of the neutron correction factor k and the Z ratio

The field specific neutron correction factor k is required according to equation (2.13). It allows to compensate for the strong energy dependence of the dosimeter as described in Chapter 2.5. In Chapter 4 it was affirmed that the previous energy dependence of neutron dosimeters could be compensated with the TL-DOS system. Still, the data recorded in the reference fields cannot be fully explained. It seems, that no uniform relation can be

found, that describe all k - Z data (Fig. 4.4) of the individual reference fields by only one function.

The k factor is supposed to compensate the energy dependence, so it is itself also energy dependent. In fields where the new neutron dosimeter has a high response (low average energy) the k factor is small and for fields where the dosimeter has a small response (high average energy) the k factor is large.

For a better understanding of the k - Z -scatter plot (Fig. 4.4), the energy dependence of k is examined. For this purpose, the data measured in the reference fields are used.

In Figure 7.1, the k factors calculated in Chapter 4 are plotted against the average energy of the neutron fields. The mean neutron energy of the reference fields are given in the PTB report [63]. To guide the eye, a square root function is plotted to the data in the figure.

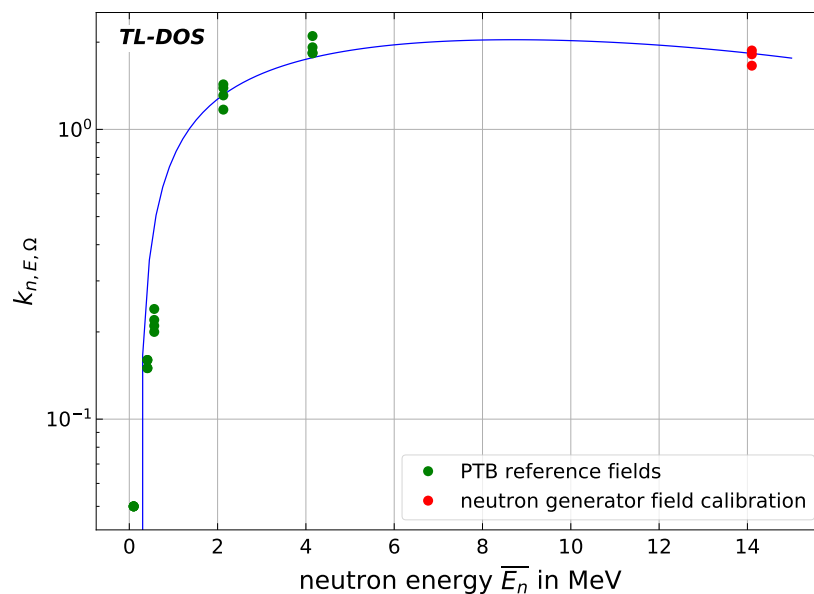


Figure 7.1: Field specific neutron correction factor k of measurements in the neutron reference fields plotted against the respective averaged neutron energy [63] of the field. Additionally, the measurements at the neutron generator are added in red and a square root function is shown to guide the eye.

In addition, the data of the field calibrations at the Fraunhofer Institut are entered. However, these have to be treated with caution because of the resulting scattered radiation, the average neutron energy of this field will be lower than $E=14.1$ MeV. Neutrons with an energy of 14.1 MeV are produced by the generator. Hence, this is the maximum energy of the spectrum, which is otherwise unknown. For the study only the 0° measurements are used to minimize the neutron scatter effect.

For all other field calibrations, presented in Chapter 4, the neutron energy spectra are

not known and therefore, they cannot be taken into account.

It should also be noted that very different energy spectra can produce the same mean energy. The field energy spectra plotted in Figure 4.1 confirm that there are many possibilities for the form. The energy spectrum of a neutron field is only limited by the typical characteristic ranges (see Figure 2.1).

As expected, Figure 7.1 verifies that k depends on the neutron energy and all factors are described by one function. In routine dosimetry $k(E)$ is estimated via the Z ratio. The k - Z plot shows that the energy dependence is represented worse by the Z ratio. The trend of the data can not be described by one function without resulting in large deviations.

7.1.1 Z as unfavorable factor

The Z ratio is directly determined from the measurements of an albedo dosimeter (equation (2.16)). So far it is supposed to be a measure for the energy dependence of a neutron field. Current practice in neutron dosimetry to estimate the energy range of the irradiation is using a calibration function $k(Z)$. Thus, for ensuring this, both k and Z should depend on energy.

In Figure 7.2 the ratio Z is plotted against the neutron energy of the reference fields. There is no dependency between the two quantities that is described well by only one function. Especially, for energies $\bar{E}_n \approx 0.5$ MeV various Z ratios (0.2–0.7) are found. The figure also shows four Z ratios for $\bar{E}_n = 0.4$ MeV, but these fluctuate only very slightly and are difficult to see. Therefore, the workaround via four N categories and four functions according to DIN 6802 is currently necessary.

Neutron fields, that have a similar average energy and therefore a similar k factor should be assigned, can have very different values for Z . The Z ratio depends not only on the neutron energy, but also on the composition of the energy spectrum. The larger the relative thermal component of the field, the higher is the Z ratio.

The ratio Z is not optimally suited, so it is checked whether there are better possible parameters to estimate the k factor from the measured values.

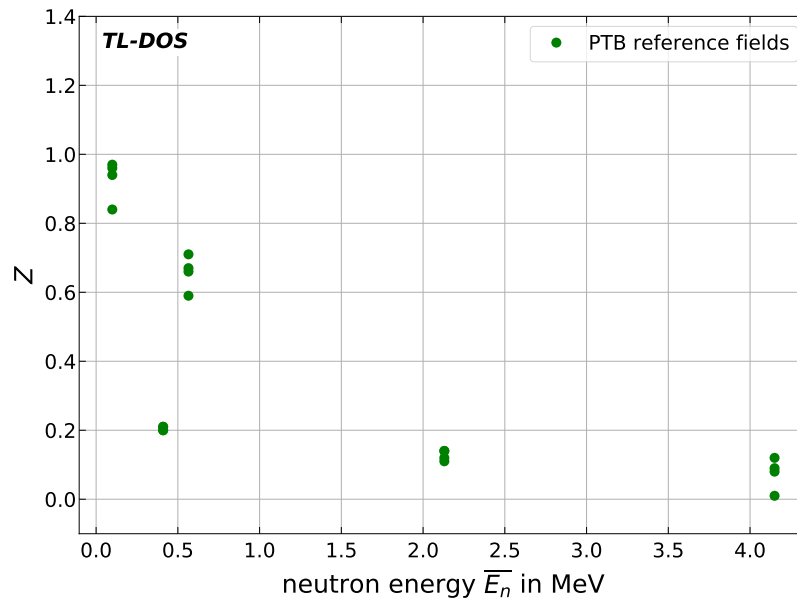


Figure 7.2: Calculated Z ratio of measurements in the neutron reference fields plotted against the respective averaged neutron energy [63] of the field.

7.2 Possible alternative for the energy estimation

In this chapter, three alternatives for determining the k factor for the new TL-DOS neutron dosimeter are studied. In all cases the energy estimation is modified or changed. For this purpose, the additional high temperature peaks are used, new N-categories are defined and different doses measured by an albedo dosimeter ($H_{n,A}$, $H_{n,F}$) are combined.

7.2.1 Energy dependent high temperature peaks

The simplest method to estimate the neutron energy is by using the high temperature peaks of a glow curve. As described in Chapter 6.2, all individual peaks including the high temperature peaks are energy dependent, but this is only valid for the albedo detectors in a neutron badge and not for the field detectors. The albedo detectors mainly measure the back-scattered, moderated neutrons (thermal neutrons). Therefore, the different sensitivity of the detectors for various neutron energies has a smaller influence on the signal of albedo detectors than on the signal of the field detectors. It is confirmed in Figure 7.3 (left), where the counts of the high temperature peaks are plotted against the average neutron energy. While the data, marked in purple, shows an exponential correlation, this cannot be observed for the field measurement data marked in green.

However, the count values of N_{67} additionally depend on the dose. In Figure 7.3 all detectors were irradiated with the same dose.

The count values N_{67} have to be normalized before using for energy estimation in routine dosimetry. Since all peaks show the same energy dependence (see Chapter 6.2), the energy is averaged out by normalizing to the total integral of the glow curve, see Figure 7.3 (right). The resulting ratios are equal for all neutron reference fields, so that it can unfortunately not be used for solving the challenge of energy dependence.

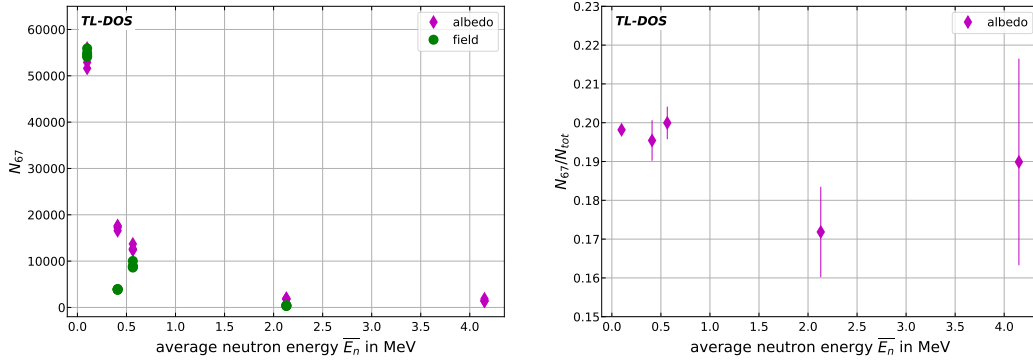


Figure 7.3: Left: Energy dependence of the high temperature peaks. Once for the albedo detectors in purple and once for the field detectors in green. Right: The integral of the high temperature peaks normalized to the total glow curve integral for five reference fields.

7.2.2 Modifications of the Z ratio

Another possibility for the energy estimation is the adjustment or even a replacement of the Z ratio. Therefore, it is searched for new alternative ratios, which are calculated with the same quantities ($H_{n,A}, H_{n,F}$) as the Z ratio use.

Approximately, an albedo dosimeter measures the total energy spectrum in two bins. The lower neutron energies are mainly detected by the field detector and the higher energies induce signal on the albedo detector after moderation and back-scattering. For this reason, it is obvious to sum up these two signals to represent the whole energy spectrum.

$$S = H_{n,A} + H_{n,F} \quad (7.1)$$

However, this introduced parameter S depends on the irradiated dose. In order to neglect the dose dependence, the parameter is normalized to the irradiated dose before the k factor is applied in Figure 7.4 (left).

In comparison to the k - Z scatter plot (Figure 7.4 (right)) these data is better described

by only one unique curve. A relationship is found which could be described by an exponential function.

For routine evaluation of a neutron dosimeter, it is advantageous, if the energy did not need to be estimated via the N-categories, but that all measurements are treated equally, as shown in Figure 7.4 (left). This would ensure that no wrong characterization in one of the four categories can happen. However, the disadvantage of this method is the dose dependence. All measurements have to be normalized to the dose or the curve shifts further to lower or higher x-values depending on the dose increase or reduction.

The challenge arises: One parameter is always unknown, either the energy or the dose of the irradiation, so that the system of equations is under-determined.

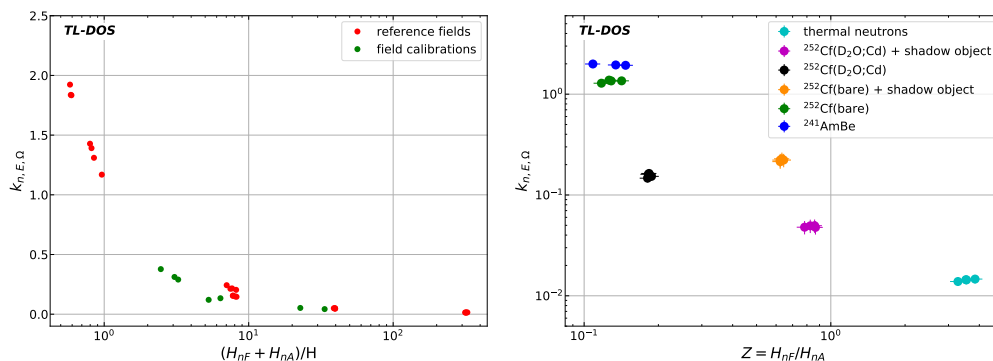


Figure 7.4: Left: The Z ratio is replaced by S normalized to the dose. The k factors of the reference fields and some field calibrations is plotted against this factor. Right: Results of the reference fields determined by the common analysis method using the Z ratio to compare it with the right plot.

For the evaluation of a dosimeter it is necessary that the dose value is not necessary and can be unknown. One possibility to determine a non-dose dependent parameter is to combine the sum S with the albedo dose $H_{n,A}$ or field dose $H_{n,F}$. In Figure 7.5 (left) the albedo dose is normalized to the sum S . This parameter is called V ratio:

$$V = \frac{H_{n,A}}{H_{n,A} + H_{n,F}}. \quad (7.2)$$

The albedo dose and not the field dose $H_{n,F}$ has been chosen because it is used to estimate the personal dose equivalent $H_{p,n}(10)$.

In Figure 7.5 on the left side, the k factor is shown as a function of the normalized albedo dose. The data is described by an exponential function which is called M1 in the following. The lower part shows the relative deviation of the estimated k factors of the reference fields to the fitted curve. Mostly, it is up to 50%.

Whether this method would provide a suitable improvement is checked and compared to the currently used method in the following chapter.

For a different representation of this method, the k factor is normalized to the V ratio and plotted against the k factor. This is shown in addition to a linear fit

$$k = m \cdot \frac{k}{V} + b \quad (7.3)$$

in Figure 7.5 (right). This function is referred to as M2 in the following. While the relative deviation for large k factors is very small, it can be as high as $\pm 50\%$ for smaller k factors ($k < 0.1$). This method M2 will also be compared to the current situation in Germany in Chapter 7.3. The energy dependent correction factor is calculated using

$$k = \frac{b}{1 - \frac{m}{V}}. \quad (7.4)$$

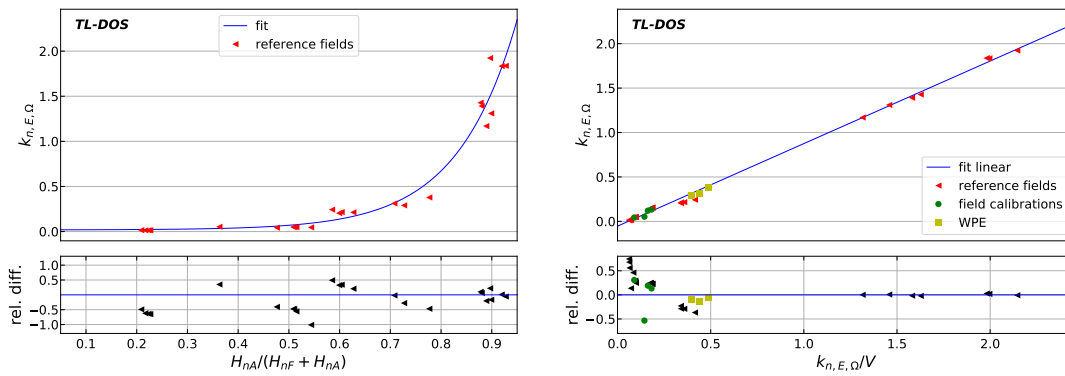


Figure 7.5: Left: The k factors of the reference fields are plotted against the determined albedo neutron dose normalized to the sum. The plot additionally shows an exponential fit and the relative difference from the data to the fit (M1). Right: The k factors of the reference fields and field calibrations (Epos, castor storage hall, WPE) depending on the defined ratio k to V are described by a linear function. The relative deviation of the data to the fit are illustrated as well (M2).

7.2.3 Reduction of N categories

At the current status, a user of an albedo dosimeter has to classify himself in one of the four N categories of application so that the energy dependence can be described as good as possible (see Chapter 2.7). The major source of error is the assignment to a wrong category.

The classification would be easier, if there are less categories for choosing. For this reason, tests are carried out with a reduced number of N categories.

Through performance of field calibrations presented in Chapter 4, the N2 category is being questioned. For this reason, the N2 category will be neglected in the following.

In addition, the range of the k factor in the TL-DOS system has become much narrower

compared to commercial systems. As shown in Chapter 2.7, during the development of albedo dosimetry, the k factor was required not to exceed a value of two within each individual category. While for the old system this criterion results in the four categories (N1 to N4), the number can be reduced with the same claim for the TL-DOS neutron system in good conscience.

The N categories are reduced from four to two functions (Line-H and Line-L) in the following. While the Line-H is supposed to replicate the fields with mainly high neutron energies and a high k factor, the Line-L is used for the fields with lower energies.

The reference fields are assigned to these two Lines based on their energy spectra (Fig. 4.1). The data of the three reference fields with the largest part of high energy neutrons ($^{241}\text{AmBe}(\alpha,n)$, ^{252}Cf , $^{252}\text{Cf} + \text{shadow object}$) represent the H-Line. Whereas the L-Line is fitted to the data of the reference fields with mainly neutron energy $E < 0.1$ MeV.

Figure 7.6 shows the current four N functions on the left and the two new functions on the right. Both Lines (H and L) are fitted with an empirical function:

$$k = a \cdot \exp(-b \cdot Z) - c. \quad (7.5)$$

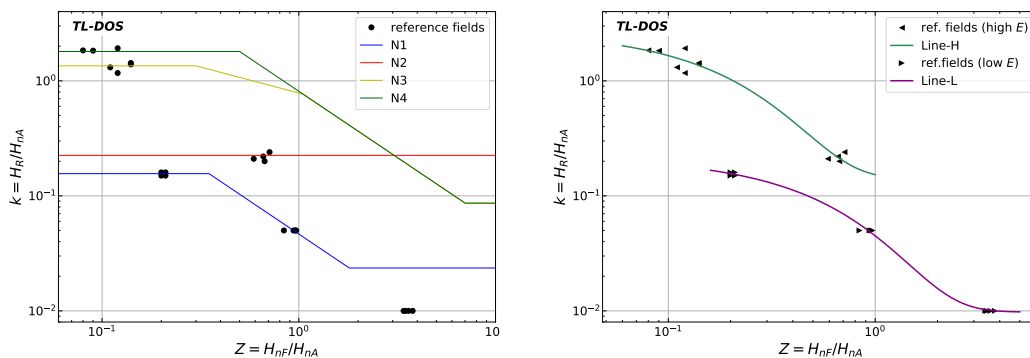


Figure 7.6: Left: The four currently used functions of the N categories (see also Chapter 2.7). The data are measured in the neutron reference fields with the new TL-DOS dosimeter. Right: Two new functions fitted through the reference field data. One describes high and one low energy fields.

In order to apply the two categories in routine dosimetry, the dosimeters have to be assigned to one of the them before analysis starts. For example this decision is made based on the maximum occurring neutron energy.

Hence, for applications in neutron workplace fields where very fast neutrons can occur, the H-line is used. Whereas the L-line is used for fields with primary low-energy neutrons. For the two categories, the Z ratio only gives information about the thermal neutron part of the field.

7.3 Intercomparison of different energy-estimation methods

In the last sections different methods for evaluation and especially for the determination of the k factor have been presented. These are compared with each other in the following. For this purpose the data of the field calibrations presented in Chapter 4 is used.

The data is evaluated by three new possibilities and the current rule (Chapter 2.7). In all four cases, the k factor is determined and then multiplied by the albedo dose value $H_{n,A}$ of the measurement to estimate the neutron dose $H_n(10)$.

First, the calculated k -factors are compared with those determined from the field calibration. In Figure 7.7 (left), the relative difference between the calculated k factors and the reference k factors, determined for different workplace fields (see Chapter 4.4), are shown. Most results of the difference between the calculated k factor and the reference k factor are in the range $\pm 50\%$. However, especially for the measurements at the WPE, the current regulation (blue markers) show a very large deviation. The smallest deviation for the measurements at the WPE is found for the analysis with the two application areas (H and L) and M1 (k determination about the ratio albedo to sum). For these, the deviation of the Epos field calibrations is also low. The data of the castor field calibrations show the smallest deviation up to $\pm 10\%$ for the H- and L-Line, as well.

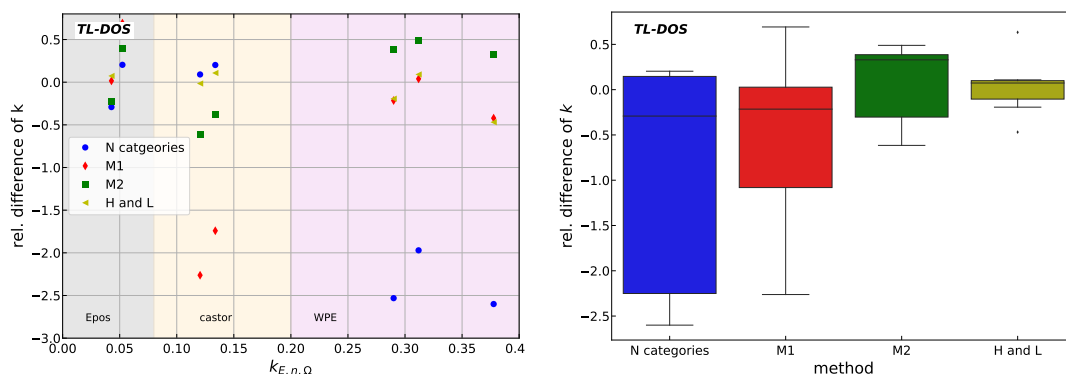


Figure 7.7: Left: Relative deviation between the k factor calculated by an analysis method to the k factor determined by field calibrations for three different measurements is presented depending on the k factor. The background color of the figure marks the different locations of the measurements. Right: The relative difference of k for the four different analysis methods.

Figure 7.7 (right) shows the relative deviation of k as box plot. In addition to the median, the quartiles 1 and 3 (25% and 75%) are also shown in the figure. The smaller the distance between the two quartiles (box height) the more uniform are the k factors for different neutron fields distributed. For example the method of the N categories results in large differences depending on the neutron field. This method is suitable for some neutron

fields and for other neutron fields it is not. The smallest fluctuation in the deviations is shown by the analysis using the H- and L-Line. Of the four analyses considered, this method is the best and can be applied to all of the fields.

In a second step, with the calculated k factors the neutron dose is determined by means of equation (2.13). Then the response is determined according to equation (2.8) to verify if the analysis dose delivers values within the given limits. The results are entered together with the allowed limits (specified by the PTB) in Figure 7.8.

The best results are found for the methods with two application areas (H-/L-Line). The results for this analysis (yellow triangles) are closest together and therefore show the flattest response. All but one data point are in the required range. In addition, dosimetry offers the possibility to correct the entire response upwards or downwards. This is achieved by a correction factor that is applied to all measurements. If this procedure is applied to the selected method, all points would be located between the limits. Additionally, most results would overestimate the dose and not underestimate it. This is a popular feature in personal dosimetry due to its conservative nature. For these reasons, the analysis using two functions (line-H and -L) is recommended as the best possible solution of the four methods tested.

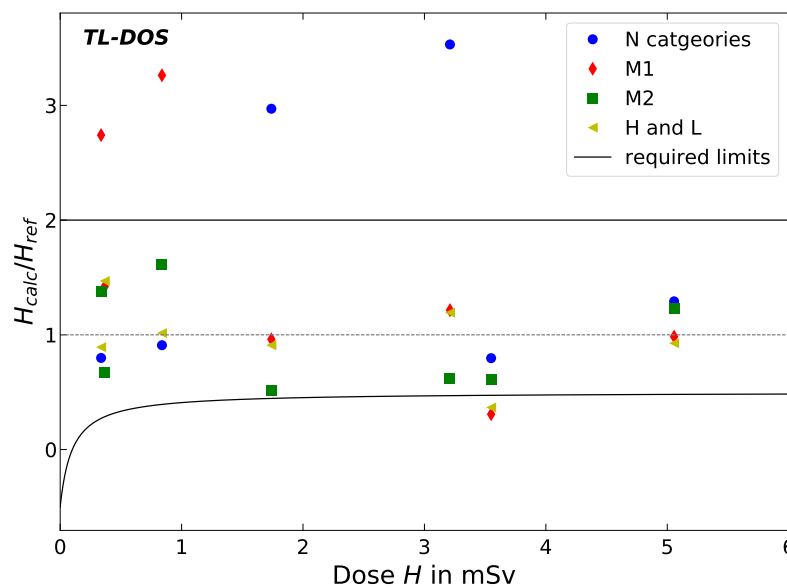


Figure 7.8: The response H_{calc}/H_{ref} of the calculated dose to the reference dose plotted against the dose. The results for all four analysis methods are presented together with the allowed area (between the two black lines).

It was asserted that the system of parameters, which are measured with the neutron dosimeter to estimate the dose, is currently an under-determined system of equations.

There is always a quantity (energy or dose) missing although angles of irradiation have not yet been taken into account.

Another possibility to estimate the neutron energy is to change the design of the neutron 'albedo' badge. A more component system (more detectors or filters) is needed for better understanding and to solve the energy dependence. If different filters are installed in front of the detectors in the badge, the energy spectrum of the field can be described better. Depending on the energy of the neutron radiation it is moderated and shielded in different filters, which can lead to a rough reconstruction of the energy.

This method is only possible because of the mixed field separation by only one detector as presented in Chapter 6.

In the future, simulations of badge irradiation could be carried out for a better understanding of the irradiation process. In addition, this could also show whether a different badge size of dosimeter could be used. Improving the analysis even further by taking a closer look at energy dependence is a good way to improve the TL-DOS neutron dosimeter. The dose estimation would become more reliable and accurate.

Chapter 8

Conclusion and Outlook

In this thesis, a neutron dosimeter based on the TL-DOS system was developed to measure the dose equivalent $H_{p,(n+\gamma)}(10)$ by using the principle of an albedo dosimeter. Thermoluminescence neutron detectors were optimized based on investigations on powder types and forms. Additional signal of a glow curve, the high temperature peaks, is measurable by a suitable adjustment of the readout temperature and a reduction of the resulting higher background. A further development of the glow-curve deconvolution tool GCana.py enables a precise analysis of the signal obtained. The design of the dosimeter system for measuring the whole body photon and neutron dose was completed with the use of the albedo badge developed at the TU Dresden.

The newly designed neutron dosimeter was characterized in the well known neutron reference fields of the PTB, in order to define a calibration and evaluation procedure. Compared to commercial systems, a sensitivity gain of a factor of 2 is observed. This is due to the additional measured signal, thinner detectors and the optimized badge. It was found that the scattering of the albedo specific factors k and Z for the TL-DOS system is in the same order of magnitude as for commercial systems. The impact of the energy dependence is smaller for the TL-DOS system and does not cover such a large range as commercial systems do. It is concluded that the system works and is operational for personal dosimetry.

By performing field calibrations in unknown fields, the different application areas of workplace fields were tested. Measurements were performed in thermal neutron fields up to high energy neutron fields. All results provide a possible usage of the new dosimeter in these applications.

Subsequently, it was shown by irradiation at an X-ray facility that the photon energy and angle-dependence for the determination of the $H_{p,\gamma}(10)$ dose are flat and meet the requirements of the PTB. The beta criterion is fulfilled with a suitable boron filter in the neutron badge, as was discussed quantitatively. For the designed system the detection limit for photon irradiation was determined to 52 μSv despite the time-dependent loss of sensitivity of the photomultiplier of the readout device. This is clearly below the required

threshold of 100 μSv . In addition to the currently used detector Li7-A, the detector Li6-A can be used as backup to estimate the photon dose, since it also fulfills all requirements. Based on the performed measurements it is concluded that the developed neutron dosimeter can be used in the routine operation of an individual monitoring service. In future, the dose signal linearity and angular irradiations can be measured in a neutron field for an even detailed characterization of the system.

Furthermore, more information about a preceding irradiation were extracted by analyzing the additional measurement signal. Investigations of the high temperature peaks show the same neutron energy dependence as found for the other peaks (2–5). After alpha irradiation, a slightly stronger fading (30% after 30 d) in contrast to a photon irradiation (25% after 30 d) is confirmed.

If the peaks of a glow curve are considered individually by using a deconvolution, different peak integral ratios can be calculated. They are used to determine the type of irradiation being either photons, alpha particles or neutrons.

An analysis was developed to separate the gamma induced signal and the alpha induced signal with only one detector after an alpha+gamma mixed irradiation. It is based on calculating the ratio of the integral of peak 5 to that of peaks 6 and 7. With this method, the gamma fraction is determined e.g for a gamma fraction of 0.5 with an uncertainty of $\pm 5\%$.

First measurements in neutron+photon mixed fields show that the same analysis technique is also applicable to this irradiation. The fact that neutron fields are usually mixed fields requires to separate the photon and neutron doses. So, this analysis allows a new separation of the doses measured by a neutron dosimeter. So far, two detectors (Li6, Li7) are needed in one badge to determine both the photon and neutron dose. The separation with only one detector could serve as redundancy or even reduce the number of detectors and thus the size of the badge. The separation of the doses could be improved by using multivariate analyses, similarly as shown for the irradiation time in Ref. [34].

Finally, the current evaluation method in Germany to solve the challenge of a strong energy dependence was examined critically. A reduction of the number of functions of the application areas (N) from four to two other functions is proposed as alternative evaluation. In order for a better understanding of the energy dependence, simulations of an irradiation of the dosimeter or irradiation at an accelerator with monochromatic neutrons are promising. Moreover, since the system of equations is under-determined for determining dose and energy from the same dosimeter, a dosimeter design with more components might be helpful. Therefore, future prospects should include different filters in front of the detectors to gain more information about the irradiation energy. For this purpose there is enough space in a badge due to the detector reduction resulting from the new separation analysis.

Acronyms

AWST Munich Mirion Technologies (AWST) GmbH in Munich

DIN Deutsches Institut für Normung und Standards

DL detection limit

DT decision threshold

Epos ELBE Positron Source at Research Center Dresden / Rossendorf

EURADOS The European Radiation Dosimetry Group

ICRU International Commission on Radiation Units and Measurements

LiF:Mg,Ti Lithium Fluoride doped with Magnesium and Titanium

ISO The International Organization for Standardization

k factor energy-specific correction factor

KFK monitoring service Karlsruhe

LET linear energy transfer

MPA NRW Materialprüfungsamt North Rhine-Westphalia

OSL optically stimulated luminescence

PMT photo multiplier tube

PTB Physikalisch-Technische Bundesanstalt

PE polyethylene

PMMA Polymethyl-methacrylate (acrylic glass)

RoI region of interest

StrISchV "Strahlenschutzverordnung", Radiation Protection Ordinance

TL thermoluminescence

TLD thermoluminescence detector

TL-DOS thermoluminescence dosimeter system

WPE The West German Proton Therapy Centre Essen

Bibliography

- [1] The first fifty years of Radiation Protection, 1980.
- [2] Verordnung zum Schutz vor der schädlichen Wirkung ionisierender Strahlung (Strahlenschutzverordnung - StrlSchV), 2018. Enter into force on 31. December 2018.
- [3] M. Heiny et al. A new TL-DOS neutron dosimeter for measurements of the personal dose equivalent $H_p(10)$. *Radiation Protection Dosimetry*, 2019. doi:10.1093/rpd/ncz251.
- [4] M. Heiny et al. Separation of alpha and gamma induced signal with LiF:Mg,Ti thermoluminescence detectors in mixed irradiation fields. review process, 2020.
- [5] T. Haninger et al. Properties of the beosl dosimetry system in the framework of a large-scale personal monitoring service. *Radiation Protection Dosimetry*, 170:269–273, 2016. doi:10.1093/rpd/ncv425.
- [6] MPA. Albedodosimeter. interne Gebrauchsanweisung, 2018.
- [7] Povh, Rith, Scholz et al. *Teilchen und Kerne: Eine Einführung in die physikalischen Konzepte*. Springer Lehrbuch, 2 edition, 1994.
- [8] B. Dörschel and L. Herforth. *Neutronen-Personendosimetrie*. Springer Basel AG, 1 edition, 1979.
- [9] W. M. Stacey. *Nuclear Reactor Physics*. Wiley-VCH Verlag GmbH & Co. KGaA, 3 edition, 2018.
- [10] M. Dommert et al. A bayesian approach for measurements of stray neutrons at proton therapy facilities: quantifying neutron dose uncertainty. *Radiation Protection Dosimetry*, 180(1–4):319–323, 2018. doi:10.1093/rpd/ncx264.
- [11] J. E. Martin. *Physics for Radiation Protection*. Wiley-VCH Verlag GmbH & Co. KGaA, 3 edition, 2013.
- [12] W. Schlegel and J. Bille. *Medizinische Physik 2*. Springer, 1 edition, 2002.
- [13] Report 51. Quantities and Units in Radiation Protection Dosimetry, 1993.
- [14] M. Piepenbrock. *Entwicklung einer Dosimetersonde zur Bestimmung der Tiefenpersonendosis $H_p(10)$ und der Oberflächendosis $H_p(0.07)$ mit dem Thermolumineszenz-Dünnschichtdosimeter-System TL-DOS*. Master's thesis, TU Dortmund, 2016.

- [15] IEC 62387: Radiation protection instrumentation - Passive integrating dosimetry systems for personal and environmental monitoring of photon and beta radiation, 2007.
- [16] W. G. Alberts et al. Neue Dosis-Meßgrößen im Strahlenschutz. *Physikalisch Technische Bundesanstalt PTB-Bericht*, 1994.
- [17] P.-T. W. PTW Freiburg. Radiation Medicine QA, SOLUTIONS, Blätterkatalog. Website, 2017. Online: http://www.ptw.de/fileadmin/data/download/catalogviewer/Radiation_Medicine_Cat_en_58721100_09/blaetterkatalog/index.html#page_1; accessed 10-2017.
- [18] Physikalisch-Technische Bundesanstalt. PTB-Anforderungen PTB-A 23.2 "Strahlungsmessgeräte; Personendosimeter zur Messung der Tiefen- und Oberflächen-Personendosis", November 2013.
- [19] Gesetz über das Inverkehrbringen und die Bereitstellung von Messgeräten auf dem Markt, ihre Verwendung und Eichung sowie über Fertigpackungen (Mess- und Eichgesetz - MessEG) , 2013. Last modification 20.11.2019.
- [20] ISO 4037-3: X and gamma reference radiation for calibrating dosimeters and dose-rate meters and for determining their response as a function of photon energy - Part 3: Calibration of area and personal dosimeters and the measurement of their response as a function of energy and angle of incidence, 1999.
- [21] E. Fantuzzi et al. EURADOS 2012 intercomparison for whole-body neutron dosimetry. *Radiation Protection Dosimetry*, 161:73–77, 2014.
- [22] ISO 8529-3:1998 Reference neutron radiation -Part 2: Calibration of area and personal dosimeters and determination of their response as a function of neutron energy and angle of incidence., 1998.
- [23] B. M. Freitas et al. MCNP Simulation of the $H_p(10)$ Energy Response of a Brazilian TLD Albedo Neutron Individual Dosimeter, from Thermal to 20 MeV. *Radiation Protection Dosimetry*, 170(1–4):350–353, 2016. doi:10.1093/rpd/ncv379.
- [24] F. Vanhavere et al. Testing three types of active personal neutron dosimeters for application in a nuclear research centre. *Radiation Measurements*, 45:1593–1596, 2011. doi:10.1016/j.radmeas.2010.06.067.
- [25] P. Bilski et al. Lithium fluoride crystals as fluorescent nuclear track detectors. *Radiation Protection Dosimetry*, 178(3):337–340, 2018. doi:10.1093/rpd/ncx116.
- [26] H. J. Brede. Improvement of response of CR-39 nuclear track detectors in fast neutron dosimetry. *Radiation Protection Dosimetry*, 85:113–116, 1999. doi:10.1093/oxfordjournals.rpd.a032813.
- [27] M. Luszik-Bhadra et al. Albedo neutron dosimetry in Germany: regulations and performance. *Radiation Protection Dosimetry*, 162(4):649–656, 2014. doi:10.1093/rpd/ncu042.

-
- [28] E. Piesch and B. Burghardt. Erprobung eines Albedoneutronendosimetriesystems: TLD-Kalibrier- und Messverfahren, Neutronenkalibrierung, dosimetrische Eigenschaften, Routineanwendung. Technical Report KfK 4303. Technical report, Kernforschungszentrum Karlsruhe, 1988.
- [29] E. Piesch and B. Burghardt. Albedo Dosimetry System for Routine Personnel Monitoring. *Radiation Protection Dosimetry*, 23:117–120, 1988. doi:10.1093/rpd.a080142.
- [30] DIN. Neutron dosimetry - Part 4: measurement technique for individual dosimetry using albedo dosimeters. *DIN 6802-4*, April 1998.
- [31] Passive neutron dosimetry systems — Part 1: Performance and test requirements for personal dosimetry. 2015.
- [32] R. Boyle. *Register of the Royal Society*, 1663:213, 1663.
- [33] S. W. S. McKeever. *Thermoluminescence of Solids*. Cambridge Solid State Science Series. Cambridge University Press, 1985.
- [34] R. Theinert. *Estimation of fading time and irradiation dose in thermoluminescence dosimetry using uni- and multivariate analysis techniques*. Dissertation, TU Dortmund, 2018.
- [35] B. B. Shachar and Y. S. Horowitz. Dosimetric characterisation of the high temperature peaks of LiF:Mg,Ti and CaF₂:Tm using computerised glow curve deconvolution. *Radiation Protection Dosimetry*, 22(2):87–96, 1988.
- [36] Y. S. Horowitz and D. Yossian. Computerised glow curve deconvolution: Application to thermoluminescence dosimetry. *Radiation Protection Dosimetry*, 60(1), 1995.
- [37] F. Mentzel. *Empirical Simulation of Glow curves for Multivariate Analysis in the TL-DOS Project*. Master’s thesis, TU Dortmund, 2018.
- [38] Report 16. Linear Energy Transfer, 1970.
- [39] R. Theinert et al. Fading time and irradiation dose estimation from thermoluminescent dosimeters using glow curve deconvolution. *Radiation Measurements*, 108:20–25, 2018.
- [40] K. Kröniger et al. A machine learning approach to glow curve analysis. *Radiation Measurements*, 125:34–39, 2019. doi:10.1016/j.radmeas.2019.02.015.
- [41] WebElements, <https://www.webelements.com/lithium/isotopes.html>; accessed 2020-03-24.
- [42] IAEA. Evaluated Nuclear Data File. 2019. Data retrieved from ENDF, <https://www.nds.iaea.org/exfor/endf.htm>.
- [43] K. Höner. *Untersuchung geometrischer Einflussfaktoren auf das Ansprechvermögen eines Beta-Fingerringdosimeters bei Bestrahlungen mit einem Beta-Sekundärnormal*. Master’s thesis, TU Dortmund, 2017.
- [44] Thermofisher. Harshaw TLD Materials and Dosemeters - Catalogs, 2019.

- [45] S. Mender. *Bestimmung der Nachweisgrenze des Thermolumineszenzdosimetersystems TL-DOS für die Tiefenpersonendosis $H_p(10)$* . Bachelor's thesis, TU Dortmund, 2016.
- [46] J. Walbersloh and F. Busch. A thin-layer LiF thermoluminescence dosimeter system with fast readout for the use in personal dosimetry services. *Radiation Protection Dosimetry*, 170(1-4):191–194, 2016. doi:10.1093/rpd/ncv478.
- [47] W. Hantke. *Labortests zur Überprüfung des routinemäßigen Einsatzes von TL-DOS Ganzkörperdosimetern*. Master's thesis, TU Dortmund, 2018.
- [48] M. Piepenbrock et al. Development of a badge for the thin-layer thermoluminescence dosimeter system TL-DOS to measure the personal dose equivalent $H_p(10)$ and $H_p(0.07)$. *Radiation Measurements*, 106:543–545, 2017. Proceedings of the 18th International Conference on Solid State Dosimetry (SSD18), Munich, Germany, 3 – 8 July 2016.
- [49] M. Heiny. *Design und Prototypen-Entwicklung eines Fingerringdosimeters zur Bestimmung der Teilkörperpersonendosis $H_p(0.07)$* . Master's thesis, TU Dortmund, 2016.
- [50] Thorlabs. Dichronic Filters. https://www.thorlabs.com/newgrouppage9.cfm?objectgroup_id=986&pn=FD1B; accessed 2017.
- [51] C.-M. Linker. *Feldkalibrierung eines Albedo-Neutronendosimeters in einem Protonentherapiezentrum*. Master's thesis, TU Dortmund, 2017.
- [52] Schott. Datenblatt BG40, 2016.
- [53] E. Derugin. Master's thesis, TU Dortmund, 2020. Thesis in preparation.
- [54] A. Savitzky and M. J. E. Golay. Smoothing and Differentiation of Data by Simplified Least Squares Procedures. *Analytical Chemistry*, 36(8):1627–1639, 1964.
- [55] T. Haninger and J. Henniger. Dosimetric properties of the new TLD albedo neutron dosimeter AWST-TL-GD 04. *Radiation Protection Dosimetry*, 170:150–153, 2015. doi:10.1093/rpd/ncv406.
- [56] F. Dahmen. *Monte-Carlo Simulationen zu Thermolumineszenz Albedodosimetern*. Master's thesis, Universität Duisburg-Essen, 2018.
- [57] Radpro. MPA intern: data sheet.
- [58] PTB. Calibration report, 2019.
- [59] A. Lütting. *Charakterisierung des Aufheitzverhaltens und glühkurvenbasierte Rekonstruktion der Detektortemperatur eines Dünnschicht-Thermolumineszenzdosimeters*. Master's thesis, TU Dortmund, 2016.
- [60] G. Kitis et al. Thermoluminescence under an exponential heating function: I. Theory. *Journal of Physics D: Applied Physics*, 39(8):1500–1507, 2006.

- [61] Y. S. Horowitz et al. The thermoluminescence dose–response and other characteristics of the high-temperature TL in LiF:Mg,Ti (TLD-100). *Radiation Protection Dosimetry*, 124(2):191–205, 2007. doi:10.1093/rpd/ncm241.
- [62] ISO 12789-2:2008 Reference radiation fields – Simulated workplace neutron fields Part 1 + Part 2, 2008.
- [63] H. Kluge. Irradiation facility with radioactive reference neutron sources: basic principles. *PTB-report PTB-N-34*, 1998.
- [64] D. Radek. Prüfbericht: Dosimeter Bestrahlung in den Neutronenreferenzfeldern, 2018.
- [65] M. Jordan. Algorithmus Dosisbestimmung - Albedo-Dosimeter. interne Verfahrensanweisung V430700, 2015.
- [66] B. Burghardt and E. Piesch. Field calibration technique for albedo neutron dosimeters. *Radiation Protection Dosimetry*, pages 121–126, 1988. doi:10.1093/oxfordjournals.rpd.a080143.
- [67] M. Luszik-Bhadra. Field correction factors for personal neutron dosimeters. *Radiation Protection Dosimetry*, 170(1–4):284–287, 2015. doi:10.1093/rpd/ncv444.
- [68] R. Krause-Rehlberg et al. EPOS-An intense positron beam project at the ELBE radiation source in Rossendorf. *Applied Surface Science*, 252:3106–3110, 2006. doi:10.1016/j.apsusc.2005.08.109.
- [69] GNS Gesellschaft für Nuklear Service mbH. Data sheet: CASTOR geo Modular System, 09-2016.
- [70] B. Burgkhardt et al. Ergebnisse der Feldkalibrierung von Albedodosimetern an Brennelemente- Transportbehältern im KKP, 1999.
- [71] C. Bäumer et al. Dosimetry intercomparison of four proton therapy institutions in Germany employing spot scanning. *Zeitschrift für Medizinische Physik*, 27:80–85, 2017. doi:10.1016/j.zemedi.2016.06.007.
- [72] Fraunhofer Institue. https://www.int.fraunhofer.de/de/geschaeftsfelder/nukleare_effekteinelektronikundoptik/bestrahlungsanlagen/neutron-generator-.html; accessed 2018-10.
- [73] U. Ankerhold. Catalogue of X-ray spectra and their characteristic data - ISO and DIN radiation qualities, therapy and diagnostic radiation qualities, unfiltered X-ray spectra, 2000.
- [74] Report 47. Measurement of Dose Equivalents from External Photon and Electron Radiations, 1992.
- [75] M. Schidlowski. *Entwicklung, Charakterisierung und klinische Erprobung eines $H_p(3)$ -TL-Augenlinsendosimeters*. Master’s thesis, TU Dortmund, 2017.
- [76] J. Henniger and D. Sommer. Charakterisierung und Anpassung des TLD-Personendosimeters. 2016.

- [77] DIN ISO 11929 - Bestimmung der charakteristischen Grenzen (Erkennungsgrenze, Nachweisgrenze und Grenzen des Vertrauensbereichs) bei Messungen ionisierender Strahlung - Grundlagen und Anwendungen (ISO 11929:2010), 1999.
- [78] C. Bergmann. *Das Potential des Thermolumineszenz-Dosimetersystems TL-DOS für den Einsatz als Radonexposimeter*. Master's thesis, TU Dortmund, 2018.
- [79] T. Berger and M. Hajek. On the linearity of the high-temperature emission from ${}^7\text{LiF:Mg,Ti}$ (TLD-700). *Radiation Measurements*, 43:1467–1473, 2008. doi:10.1016/j.radmeas.2008.06.004.
- [80] D. Hannes. Abschlussbericht der Fading- und Temperaturuntersuchungen 2014/15. 2015.
- [81] S. Shachar and Y. S. Horowitz. Anomalous thermally induced fading of annealed and unannealed LiF:Mg,Ti (TLD-100, Harsahw) using computerized glow curve deconvolution. *Journals of Physics D: Applied Physics*, 24:1649–1657, 1991.
- [82] L. F. Booth et al. Lithium Fluoride Glow Peak Growth due to Annealing. *Health Physics*, 23:137, 1972. doi:10.1097/00004032-197208000-00002.
- [83] M. Steil. *Glühkurvenanalyse zur Unterscheidung von Strahlungsarten mittels Multivariaten Analysemethoden*. Bachelor's thesis, TU Dortmund, 2018.
- [84] M. Osvay and S. Deme. Comparative investigation of LiF TL dosimeters using low and high LET radiation fields. *Radiation Protection Dosimetry*, 85:469–472, 1999. doi:10.1093/oxfordjournals.rpd.a032899.
- [85] D. Youssian and Y. S. Horowitz. Estimation of gamma dose in neutron dosimetry using peak 4 to peak 5 ratios in LiF:Mg,Ti (TLD-100/600). *Radiation Protection Dosimetry*, 77:151–158, 1998. doi:10.1093/oxfordjournals.rpd.a032305.
- [86] R. C. G. M. Smetsers and R. O. Blaauboer. A Dynamic Compensation Method for Natural Ambient Dose Rate Based on 6 Years Data from the Dutch Radioactivity Monitoring Network. *Radiation Protection Dosimetry*, 69(1):19–31, 1997. doi:10.1093/oxfordjournals.rpd.a031883.

Danksagung

An dieser Stelle möchte ich allen Personen danken, die mich bei der Anfertigung meiner Dissertation unterstützt haben.

Zunächst möchte ich Prof. Dr. Herrn Kröniger für die Möglichkeit, meine Arbeit zu schreiben und die hervorragende Betreuung danken. Außerdem spreche ich Prof. Dr. Herrn Westphal meinen Dank für das Lesen und Bewerten meiner Arbeit aus.

Für den Zugang zu Messdaten und das Durchführen von Messungen möchte ich dem Fraunhofer Institut für Naturwissenschaftlich-Technische Trendanalysen INT, Helmholtz-Zentrum Dresden-Rossendorf (Epos Anlage), der BGZ Gesellschaft für Zwischenlagerung, dem Westdeutschen Protonentherapie Zentrum Essen und den deutschen Personendosismessstellen, besonders dem Materialprüfungsamt meinen Dank ausdrücken. Dabei möchte ich Ajvar für die Ermöglichung und Unterstützung bei der Durchführung von Messungen am WPE hervorheben.

Besonders danken möchte ich Jörg, dem gesamten TL-DOS Team und dem Lehrstuhl E4, die mich auf meinem Weg mit produktiven Gesprächen, Kaffeepausen, lieben Worten und tollen Veranstaltungen wie "Kuchen essen", "Freitags Kolloquien" oder "16:16" mit Rat und Tat begleitet haben.

Ich möchte die Gelegenheit nutzen, um mich bei meinem Bürokollegen HWK für die musikalisch begleiteten Pausen, seinem spontanen Humor, das Erste Hilfe Leisten bei Schokoladennotfällen und freundschaftlichen Gesprächen zu bedanken.

Des Weiteren geht ein dickes Dankeschön an Jens, Robert, Gregor und an alle anderen Korrekturleser für die wertvolle Unterstützung und das Korrekturlesen meiner Arbeit.

Meine Familie war während meines Studiums und während der Anfertigung dieser Doktorarbeit, immer mit Herzlichkeit und Geduld für mich da. Ich weiß, das ist nicht selbstverständlich. Ihr seid mir eine große Stütze!